Quantum point contacts in HgTe quantum wells

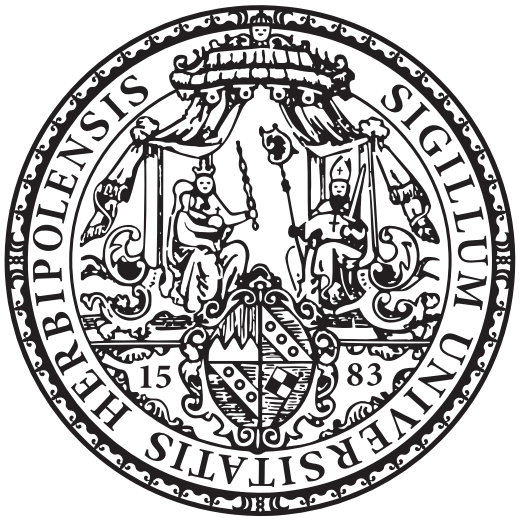

Dissertation

zur Erlangung des naturwissenschaftlichen Doktorgrades

der Julius-Maximilians-Universität Würzburg

vorgelegt von

Jonas Strunz

aus Hof (Saale)

Würzburg, 2021

Eingereicht am: 12.11.2021
bei der Fakultät für Physik und Astronomie

1. Gutachter: Prof. Dr. H. Buhmann
2. Gutachter: Prof. Dr. B. Trauzettel
3. Gutachter: .....
der Dissertation

Vorsitzender: Prof. Dr. R. Claessen
1. Prüfer: Prof. Dr. H. Buhmann
2. Prüfer: Prof. Dr. B. Trauzettel
3. Prüfer: Prof. Dr. F. Reinert
im Promotionskolloquium

Tag des Promotionskolloquiums: 13.05.2022

Doktorurkunde ausgehändigt am: .....

Meiner Familie

Contents

List of abbreviations

1D	One-dimensional
2D	Two-dimensional
2DEG	Two-dimensional electron gas
3D	Three-dimensional
AB	Aharonov-Bohm
AC	Aharonov-Casher
ALD	Atomic layer deposition
BHZ	Bernevig-Hughes-Zhang
CMOS	Complementary metal-oxide-semiconductor
DC	Direct current
EBL	Electron beam lithography
EBPVD	Electron beam physical vapour deposition
EUV	Extreme ultraviolet lithography
FFT	Fast Fourier transformation
IRDS	International Roadmap for Devices and Systems
ITRS	International Technology Roadmap for Semiconductors
HLL	Helical Luttinger liquid
MBE	Molecular beam epitaxy
PMMA	Polymethyl methacrylate
QHE	Quantum Hall effect
QPC	Quantum point contact
QSH	Quantum spin Hall

TI	Topological insulator
TLL	Tomonaga-Luttinger liquid
UCF	Universal conductance fluctuations
WAL	Weak antilocalization
WL	Weak localization
WKB	Wentzel-Kramers-Brillouin

1

Introduction

It ain't what you don't know that gets you into trouble.
It's what you know for sure that just ain't so.

Sometimes attributed to Mark Twain.

When we watch (and enjoy) lightnings during a mild summer night, when a child's haircut becomes messy after sliding down a slide, or when a frog's leg is twitched by a galvanic cell, the same fundamental mechanism is taking place: the movement of particles carrying an electric charge. This very effect however not only provides descriptive and hands-on examples for fruitful physics lessons, but is also of essential importance for the functionality of devices embedded in a myriad of everyday applications – transistors, the backbone of our digitized lives. These devices enable a controllable current flow, which is utilized for realizing logic gates within integrated circuits. Since the 1970s, the semiconductor industry was able to double the number of transistors in an integrated circuit every two years, which has caused an unequalled gain of technology and wealth. This exponential growth in chip complexity was a priori anticipated by *Gordon E. Moore* [1, 2] and is referred to as *Moore's law*.[1]

In order to keep up with the law (referred to as *More Moore*), in 1998 the global semiconductor industry started to release the so-called *International Technology Roadmap for Semiconductors* (ITRS) on an annual basis [3]. The purpose of the latter was the coordination and harmonization of efforts throughout all sectors and segments of the industry, which should ensure that new chips follow *Moore's law*. Thus, the collaboration among suppliers and manufacturers transformed the law into a self-fulfilling prophecy [4]. However, in 2015, the industry had to face the fact that a further pursuit of *Moore's law* had to be abandoned due to a combination of increasing

[1] In 1965, Gordon E. Moore forecast a doubling every year [1]. In 1975, he revised his prediction to a doubling every two years [2].

physical and economic limitations. Therefore, the ITRS orchestrated downscaling of transistor sizes was replaced by the new *International Roadmap for Devices and Systems* (IRDS) in 2016. The latter is characterized by a strategy which is referred to as *More than Moore*. It starts with the analysis of applications needs (for example smartphones or cloud data centres), followed by the development and supply of customized chips. This concept is contrary to the past, where applications where always forced to adapt to improved chip generations [4].

Despite the new conception of the IRDS, there are still a lot of ongoing efforts following and optimizing the *More Moore* way. In this context, one key aspect is a new lithography process based on the usage of extreme ultraviolet (EUV) radiation, which is referred to as EUV lithography. Substantiating the importance of the EUV lithography technology, a German industry-academic cooperation was awarded the German Future Prize 2020 for its ground-breaking contributions to realize the latter [5].

In addition to further improving the fabrication of chips, another approach is based on researching possible future logic devices realizations which are expected to perform superiorly compared to conventional complementary metal-oxide-semiconductor (CMOS) devices due to peculiar and unique physical properties. This alternative is referred to as *Beyond CMOS* (or also as *Beyond Moore*) and an example are spintronic devices [3]. A further option is represented by the implementation of an entirely new paradigm like quantum computing, which has recently experienced enormous experimental progress [6, 7]. However, the research towards quantum computation and spintronic devices is still in its early stages and the quest for material systems and physical concepts which provide optimal frame conditions to realize these seminal concepts – despite the most recent breakthroughs – is still ongoing.

In this regard, one of the most promising candidates is represented by the new material class of two-dimensional (2D) topological insulators (TIs). Devices based on these materials are characterized by conducting states at the edge of the sample, while the bulk is insulating. These so-called edge states are topologically protected against backscattering and are thus not causing any heat – one of the major drawbacks of today's CMOS technology. The corresponding signature state of 2D-TIs is the quantum spin Hall (QSH) effect, which was experimentally demonstrated for the first time in inverted mercury telluride (chemical formula HgTe) quantum wells by the group of *Laurens W. Molenkamp* in 2007 [8]. Since this seminal achievement, the utilization of these unique physical properties in the form of dedicated devices is one of the main goals of the current research in the field.

In this context, the device concept of a quantum point contact (QPC) [9, 10] is envisaged to offer a lot of novel and promising possibilities when implemented in a QSH system. It is formed by a one-dimensional (1D) constriction in an otherwise extended 2D electron or hole system. If a QPC is realized in a 2D-TI by using an etching process, the QSH edge states are brought in spatial proximity when they traverse the defined constriction. Such a scenario is expected to enable the examination of possible interaction effects between the edge states and thus to allow for a lot of unprecedented experiments. However, no working QPC technology has been

implemented in 2D-TI systems, so far. In order to overcome this backlog, the accomplishment of the latter utilizing HgTe quantum wells is the research subject of this thesis, which consists of three main chapters.

In Chapter 2, the emergence of the QSH state in inverted HgTe quantum wells is explained and the concept of QPCs is introduced. Afterwards, a newly developed lithography process for realizing QPCs in HgTe quantum wells is presented. These remarks are followed by a basic quantum transport characterization of several devices.

In Chapter 3, the formation of a QSH interferometer state in appropriate QPC devices is discussed, which is explained using a model based on band structure calculations. Due to the physical properties of inverted HgTe quantum wells, the impact of three different quantum phases is anticipated. Measurements of the QSH conductance depending on an applied gate voltage as well as on an applied magnetic field reveal the accumulation of the expected quantum phases. The results are substantiated by analytic model considerations.

In Chapter 4, the appearance of an anomalous conductance signature emerging from the QSH state of QPCs based on thick inverted HgTe quantum wells is examined. The effect is only observed for a small interval of device width values. Moreover, further experimental examination provides evidence that the signature is related to a gapped topological state and that it is accompanied by a backscattered QSH edge channel. Two explanatory theoretic models based on electron-electron interactions are presented.

Each of the three chapters is based in parts on a (to be) published manuscript. Throughout the whole thesis, required theoretical aspects are integrated within the course of each individual chapter. A recapitulating summary of the presented results is given in Chapter 5, the corresponding German version is added in Chapter 6.

1

BIBLIOGRAPHY

[1] G. E. Moore, *Cramming more components onto integrated circuits,* Electronics **38**, 114 (1965).

[2] G. E. Moore, *Progress in Digital Integrated Electronics,* in *International Electron Devices Meeting* (IEEE, Washington, D.C., 1975).

[3] Institute of Electrical and Electronics Engineers, *What is the IRDS™?,* URL: https://irds.ieee.org/ (11.11.2021).

[4] M. M. Waldrop, *The chips are down for Moore's law,* Nature News **530**, 144 (2016).

[5] Stifterverband für die Deutsche Wissenschaft e.V., *EUV-Lithographie – neues Licht für das digitale Zeitalter,* URL: https://www.deutscher-zukunftspreis.de/de/team-1-2020 (11.11.2021).

[6] F. Arute, K. Arya, R. Babbush, D. Bacon, J. C. Bardin, R. Barends, R. Biswas, S. Boixo, F. G. S. L. Brandao, D. A. Buell, B. Burkett, Y. Chen, Z. Chen, B. Chiaro, R. Collins, W. Courtney, A. Dunsworth, E. Farhi, B. Foxen, A. Fowler, C. Gidney, M. Giustina, R. Graff, K. Guerin, S. Habegger, M. P. Harrigan, M. J. Hartmann, A. Ho, M. Hoffmann, T. Huang, T. S. Humble, S. V. Isakov, E. Jeffrey, Z. Jiang, D. Kafri, K. Kechedzhi, J. Kelly, P. V. Klimov, S. Knysh, A. Korotkov, F. Kostritsa, D. Landhuis, M. Lindmark, E. Lucero, D. Lyakh, S. Mandrà, J. R. McClean, M. McEwen, A. Megrant, X. Mi, K. Michielsen, M. Mohseni, J. Mutus, O. Naaman, M. Neeley, C. Neill, M. Y. Niu, E. Ostby, A. Petukhov, J. C. Platt, C. Quintana, E. G. Rieffel, P. Roushan, N. C. Rubin, D. Sank, K. J. Satzinger, V. Smelyanskiy, K. J. Sung, M. D. Trevithick, A. Vainsencher, B. Villalonga, T. White, Z. J. Yao, P. Yeh, A. Zalcman, H. Neven, and J. M. Martinis, *Quantum supremacy using a programmable superconducting processor,* Nature **574**, 505 (2019).

[7] H.-S. Zhong, H. Wang, Y.-H. Deng, M.-C. Chen, L.-C. Peng, Y.-H. Luo, J. Qin, D. Wu, X. Ding, Y. Hu, P. Hu, X.-Y. Yang, W.-J. Zhang, H. Li, Y. Li, X. Jiang, L. Gan, G. Yang, L. You, Z. Wang, L. Li, N.-L. Liu, C.-Y. Lu, and J.-W. Pan, *Quantum computational advantage using photons,* Science **370**, 1460 (2020).

[8] M. König, S. Wiedmann, C. Brüne, A. Roth, H. Buhmann, L. W. Molenkamp, X. L. Qi, and S.-C. Zhang, *Quantum Spin Hall Insulator State in HgTe Quantum Wells,* Science **318**, 766 (2007).

[9] B. J. van Wees, H. van Houten, C. W. J. Beenakker, J. G. Williamson, L. P. Kouwenhoven, D. van der Marel, and C. T. Foxon, *Quantized conductance of point contacts in a two-dimensional electron gas,* Physical Review Letters **60**, 848 (1988).

[10] D. A. Wharam, T. J. Thornton, R. Newbury, M. Pepper, H. Ahmed, J. E. F. Frost, D. G. Hasko, D. C. Peacock, D. A. Ritchie, and G. A. C. Jones, *One-dimensional transport and*

the quantisation of the ballistic resistance, Journal of Physics C: Solid State Physics **21**, L209 (1988).

2

Realization and characterization of quantum point contacts in the quantum spin Hall insulator HgTe

In this chapter, an initial comprehensive introduction to the emergence of the quantum spin Hall effect in inverted HgTe quantum wells is provided. Subsequently, the concept of quantum point contacts is introduced and the associated transport behaviour is analytically explained based on the saddle point model. After having outlined the constraints of realizing these devices in a quantum spin Hall system, the lithographic fabrication of top gated quantum point contacts in HgTe quantum wells utilizing a multi-step wet etching technique is presented. Thereafter, the transport behaviour of a topological quantum point contact is analysed and the acquired data is compared with the conductance of a trivial sample. The gate voltage dependence of the conductance shows the expected quantization in integer steps of $\Delta G \approx 2e^2/h$ within the conduction band for both samples as well as a residual conductance of $G_{\mathrm{QSH}} \approx 2e^2/h$ within the bulk band gap for the topological device due to helical edge channel transport. Furthermore, evidence is provided that narrow quantum point contacts can be utilized as all-electrically tunable tunnel barriers in quantum spin Hall systems. Lastly, it is explicated that the trivial ballistic one-dimensional transport observed in a topological device mirrors the characteristics of quantum point contacts realized in trivial material systems under temperature and bias voltage influence.

2.1 Quantum spin Hall insulator state in HgTe quantum wells

Following the discovery of the quantum Hall effect (QHE) in a two-dimensional electron gas (2DEG) at high magnetic fields by *von Klitzing et al.* [1], the concept of band topology was introduced in order to explain the observable quantized Hall conductance [2, 3]. The latter emerges in units of e^2/h and can be described by $\sigma_{xy} = n \cdot (e^2/h)$, where $n \in \mathbb{N}$ is an integer, e is the elementary charge and h is the Planck constant. The integer n is referred to as Chern number, which indicates the number of occupied Landau Levels and defines the topology of the band dispersion.

In 2005, *Kane and Mele* [4] elaborated that topologically non-trivial states of matter can also emerge without breaking time reversal symmetry, i.e. without the application of a magnetic field. The authors analysed the band structure of graphene under the impact of spin-orbit coupling and predicted that the influence of the latter results in a gap opening within the otherwise gapless Dirac spectrum. This gapped state is characterized by an inverted band ordering, which results in the emergence of spin-polarized edge states with opposite directions of motion for opposite spin-orientations (spin-up and spin-down) at a given edge. These edge states form the so-called QSH state. In analogy with the correlation between particle momentum and particle spin known as helicity, the edge states are also referred to as helical edge states (or channels) [5]. They form a so-called Kramers doublet, which is topologically protected by time reversal symmetry. This circumstance results in the peculiar situation that helical edge channels (synonymously called QSH edge channels) are protected against backscattering as long as time reversal symmetry is preserved. A system hosting the QSH state is also referred to as a 2D-TI.

Hereinafter, it turned out that an experimental observation of the pure QSH regime in graphene would be rather challenging due to the small extent of the bulk band gap [6, 7]. Consequently, no distinct signatures of pure QSH transport have been identified in graphene based devices to this day. However – shortly after the work of Ref. [4] – a publication by *Bernevig, Hughes and Zhang* [8] predicted the QSH state to emerge for HgTe quantum wells of appropriate thickness. For a more comprehensive and extensive introduction to topological band theory, the interested reader is referred for example to Ref. [9].

2.1.1 Band structure of HgTe quantum wells

The compound HgTe is a zincblende-type II-VI material. The bonds within the material form between 6s electrons from Hg atoms and 5p electrons from Te atoms. As a result, the key energy bands located close to the Fermi energy E_F emerge from these energy levels, as it is common for most conventional zincblende-type semiconductors. However, HgTe represents a special case concerning the resulting energetic band ordering [10].

Since both Hg and Te are rather heavy atoms, relativistic corrections to the positions of the energy levels are of importance. The impact of these corrections for CdTe and HgTe is depicted

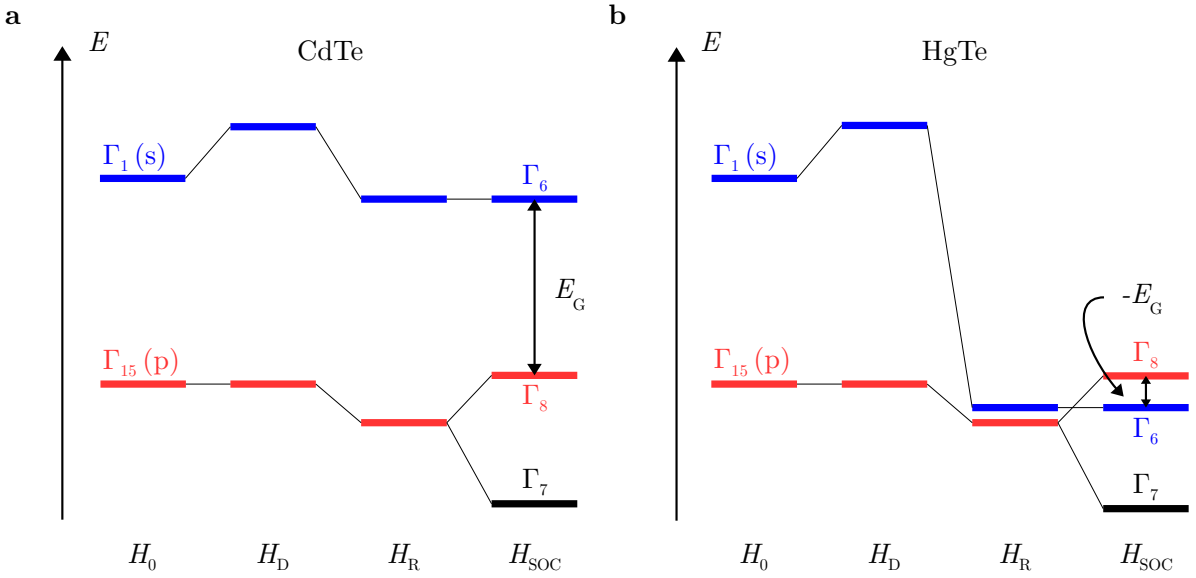

Figure 2.1: **a**, **b**, Sketch of the evolution of the key energy bands for CdTe and HgTe at the Γ-point due to several relativistic corrections. Additional to the unperturbed Hamiltonian H_0, the influence of the Darwin term H_D, of the relativistic mass velocity correction H_R as well as of the spin-orbit coupling H_{SOC} is depicted. In the case of HgTe, the pronounced H_R contribution leads to a band inversion and thus a negative band gap. Adapted from Ref. [11].

in Fig. 2.1a,b. In detail, the unperturbed Hamiltonian H_0 is corrected by the Darwin term H_D, the relativistic mass velocity correction H_R and the spin-orbit coupling correction H_{SOC} [10, 11].

Comparing the influence of the individual corrections in the afore mentioned order for CdTe and HgTe shows that the impact of the Darwin term H_D is similar for both compounds. For the relativistic mass velocity correction H_R, the situation is however quite different. The latter is caused by the difference of atomic masses and core charges for Hg and Cd. For HgTe, the mass velocity correction is so pronounced that the energetic position of the Γ_6 state (originating from Hg s-states) is lowered to close proximity to the energy level of the Te p-states, while the correction for CdTe is way smaller. Lastly, the influence of the spin-orbit coupling correction H_{SOC} splits the Te p-states into the Γ_8 and Γ_7 states – similarly for both compounds. For the case of HgTe, the Γ_8 band is lifted above the Γ_6 band, resulting in the peculiar situation of an inverted band structure, whereas CdTe exhibits a conventional ordering with Γ_6 representing the first conduction band and Γ_8 being the first valence band. Thus, to put it in a nutshell, the band inversion for HgTe emerges from an interplay between the relativistic mass velocity correction H_R and the spin-orbit coupling correction H_{SOC} [10].

In addition to be causative for the topological properties of HgTe, the band inversion has a further consequence. While the Γ_6 ($J = 1/2$) state only forms a single band, the Γ_8 (J=3/2) state leads to the emergence of degenerated light ($m_j = \pm 1/2$) and heavy hole ($m_j = \pm 3/2$) bands for the momentum $k = 0$ (see Fig. 2.2b). In this context, the definition of the band gap $E_G = \Gamma_6(k = 0) - \Gamma_8(k = 0)$ yields a value of $E_G \approx -0.3\,\text{eV}$. However, the actual band ordering at the degeneracy point of the Γ_8 band results in an effective band gap of $E_G = 0\,\text{eV}$ for $k = 0$,

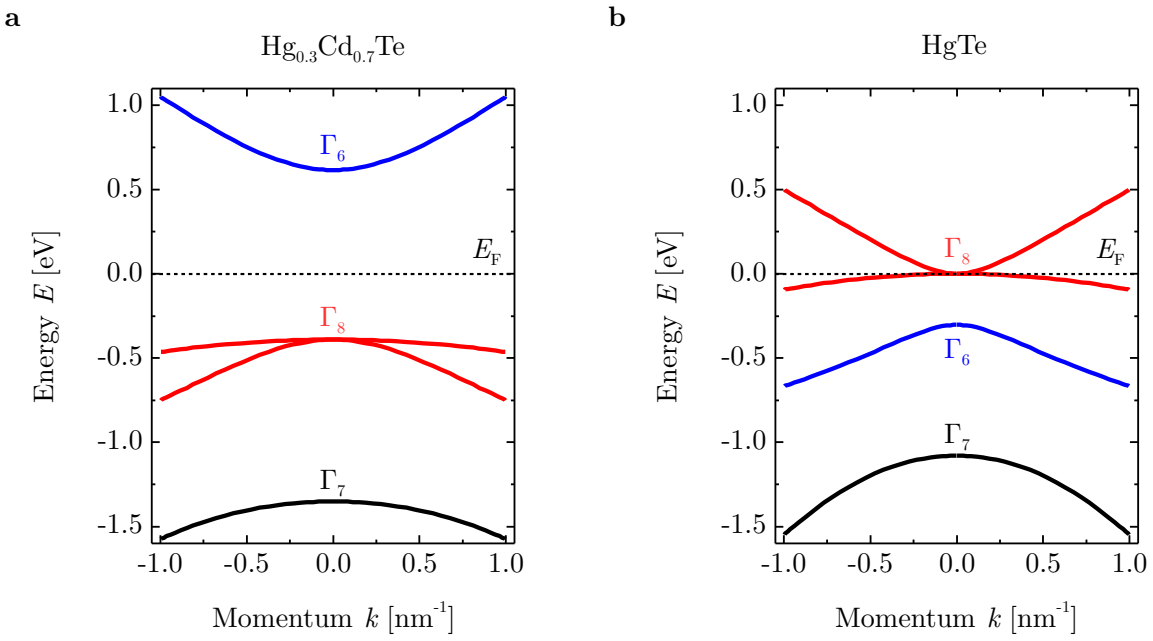

Figure 2.2: **a**, **b**, Calculation of the bulk band structure around the Γ-point for $Hg_{0.3}Cd_{0.7}Te$ and HgTe using a $\mathbf{k} \cdot \mathbf{p}$ method. In both cases, the Γ_8 state splits to a light- and a heavy-hole band. Adapted from Ref. [12].

thus making the bulk material HgTe a Dirac semimetal. In this context, the heavy hole band represents a valence band, while the light hole band acts as the conduction band [10].

In order to make the topological properties experimentally detectable without bulk modes dominating the transport behaviour, it is essential to lift the Γ_8 degeneracy and thus to open up a band gap. In this regard, one option is to confine the material into lower dimensions, thus meeting the need of the thesis at hand for 2D layers. The latter scenario is realized by growing quantum well structures using molecular beam epitaxy (MBE), where a HgTe layer gets sandwiched between two $Hg_{0.3}Cd_{0.7}Te$ layers. The band structure of $Hg_{0.3}Cd_{0.7}Te$ shown in Fig. 2.2a exhibits a conventional band ordering and a band gap of $E_G \approx 1\,\text{eV}$. The second option is based on growing three-dimensional (3D) structures, for which the degeneracy can be lifted by utilizing growth induced strain [10]. This alternative leads to the emergence of 3D-TIs [13], which will not be covered further within the scope of this thesis. For a comprehensive introduction to HgTe MBE, the interested reader is referred to Ref. [14].

The characteristic band edge profile of $Hg_{0.3}Cd_{0.7}Te/HgTe/Hg_{0.3}Cd_{0.7}Te$ quantum wells is sketched in Fig. 2.3a,b. This kind of quantum well formation is also referred to as type III quantum well. Within the HgTe layer, the spatial confinement in growth direction leads to a splitting of the Γ_6 and the heavy hole Γ_8 band into subbands relevant for transport behaviour, while the light hole state is shifted to lower energies [15]. In Fig. 2.3a–c, subbands emerging from the Γ_6 and the heavy hole Γ_8 band are labelled with E_i and H_i, respectively.

The energetic position of the subbands and thus the energetic spacing between the latter is correlated with the thickness of the HgTe layer (confinement strength), which is also referred to

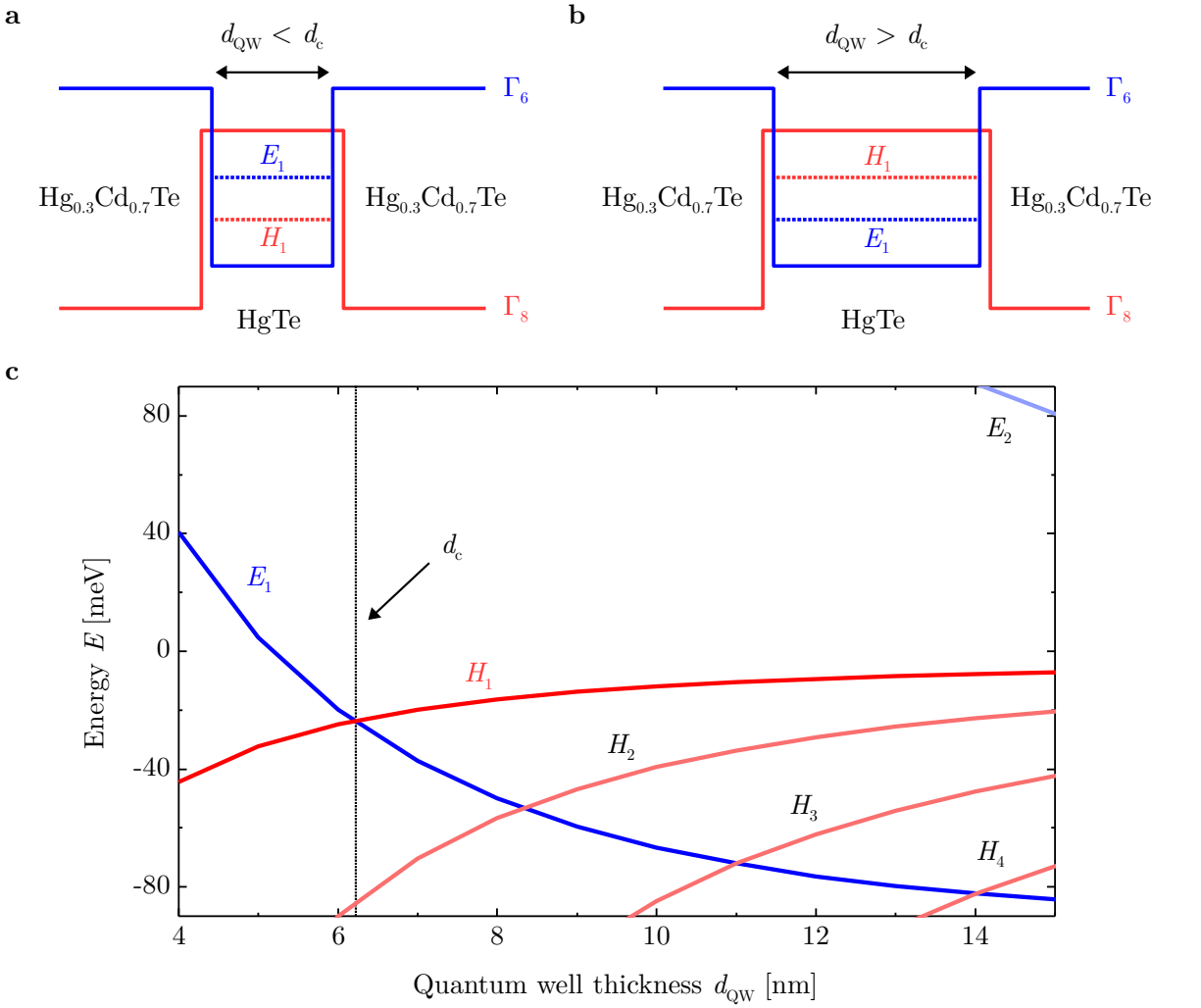

Figure 2.3: **a**, **b**, Schematic of the band edge profile for a quantum well consisting of a HgTe layer sandwiched between two $Hg_{0.3}Cd_{0.7}Te$ layers. The confined energy levels (subbands) emerging from Γ_6 states are labelled E_i, the ones originating from Γ_8 states H_i, respectively. With adjusting the quantum well thickness d_{QW}, the band structure can be tuned from the trivial regime with d_{QW} below a critical quantum well thickness d_c ($d_{QW} < d_c$) to the nontrivial, topological regime ($d_{QW} > d_c$). Adapted from Ref. [16]. **c**, Progression of the subband energies depending on the quantum well thickness. The vertical dashed line indicates the position of the critical thickness. Adapted from Refs. [16, 17].

as quantum well thickness d_{QW} (see Fig. 2.3c). For a critical thickness $d_{QW} \approx 6.3\,\text{nm} =: d_c$, the E_1 and the H_1 subband intersect. Such a situation is referred to as a zero-gap state [16]. For thinner quantum wells with $d_{QW} < d_c$, the E_1 subband (originating from the Γ_6 band) is the first conduction band and the H_1 subband (originating from the Γ_8 band) is the first valence band (see Fig. 2.3a). This regime corresponds to a topologically trivial state. For thicker wells described by $d_{QW} > d_c$ and sketched in Fig. 2.3b, the opposite is the case. There, the H_1 subband becomes the first conduction band, while the E_1 subband forms one of the valance bands (see the progression in Fig. 2.3c). In this scenario, the band inversion of bulk HgTe is regained and a 2D-TI state emerges [10].

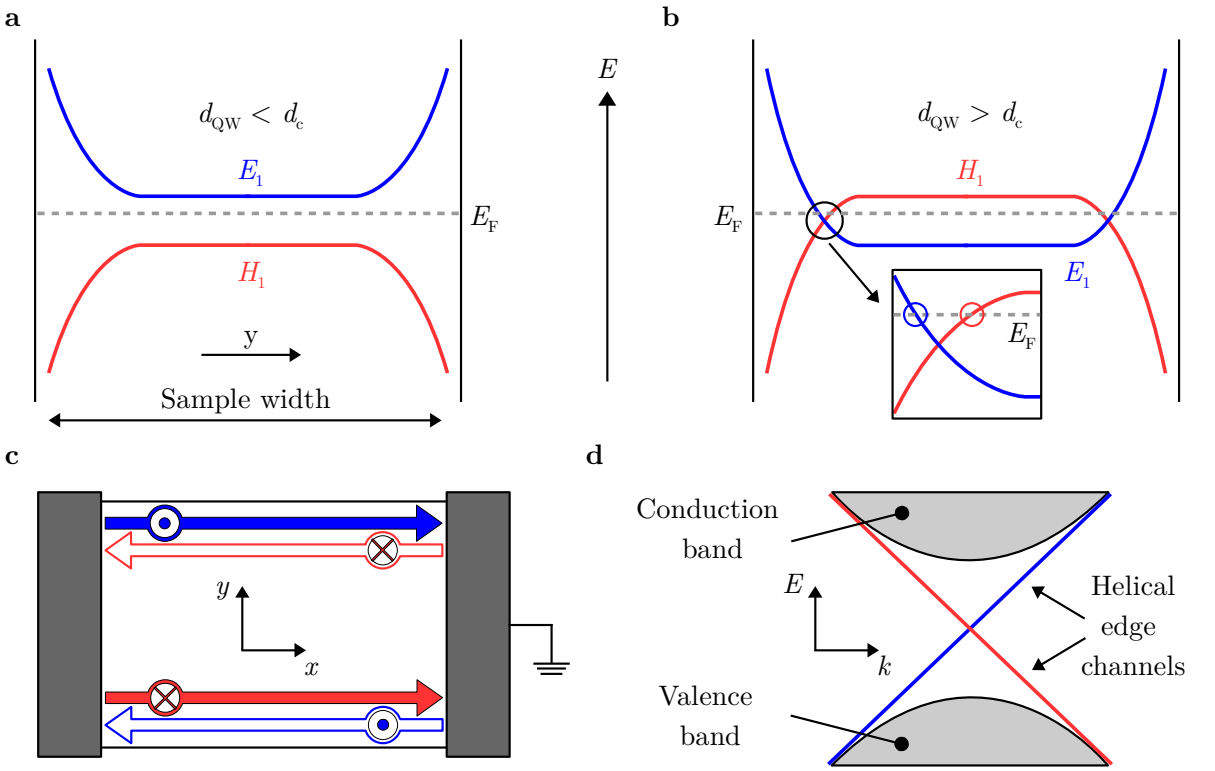

Figure 2.4: **a**, **b**, Sketch of the local energetic position of the E_1 and the H_1 subband for a trivial (panel **a**) and a topological (panel **b**) HgTe quantum well with regard to the spatial dimensions of the underlying sample. For an inverted band ordering, the subbands cross the Fermi energy at the sample edges, which leads to the emergence of QSH edge channels (see inset of panel **b**). Adapted from Ref. [18]. **c**, Schematic of a sample in the QSH regime. At the same edge, electrons carrying opposite spin species move in opposite directions. **d**, Sketch of the helical spectrum, which is linked to the emergence of helical edge channels captured in panels **b** and **c**.

2.1.2 Quantum spin Hall effect in HgTe quantum wells

The signature state of a 2D-TI material is the QSH effect, which describes the existence of 1D helical edge states at the boundaries of the system. The emergence of these states has been predicted for HgTe/CdTe quantum wells within the scope of the *Bernevig-Hughes-Zhang* (BHZ) model [8]. The latter captures the electronic states by utilizing a relativistic Dirac equation. In this description, the energy difference between the E_1 and the H_1 subband at the Γ point is equivalent to the Dirac mass M – the essential parameter of the model. A trivial band ordering in the case of $d_{QW} < d_c$ yields $M > 0$, while an inverted band structure and thus $d_{QW} > d_c$ is described by a negative Dirac mass $M < 0$.

The former has fundamental consequences for the interface between an inverted HgTe layer and an adjacent vacuum – or, in other words, for the edge of the sample. In this context, it is important to note that the vacuum is a trivial insulator with a large gap ($E_G \approx 1 \cdot 10^6$ eV) and can be regarded as a system with an infinite positive mass [19]. Thus, for the case of a normal band ordering, the extent of the band gap increases at the edge of the sample. The consequence is a trivial insulating state when the Fermi energy is located within the energy gap ($M > 0$, see Fig. 2.4a). This situation is contrasted for an inverted band structure, which is sketched

in Fig. 2.4b. In this scenario, the Fermi energy in the bulk lies within the energy gap as well. However, the Dirac mass is negative due to the inversion of the bands. At the edge, the Dirac mass and thus the band ordering needs to adjust to the trivial state of the surrounding vacuum, which leads to an energetic interchange of the H_1 and the E_1 subband. As a result, the subbands cross the Fermi energy at the edges, which leads to the emergence of QSH edge channels.

The QSH state was experimentally realized for the first time in HgTe quantum wells by *König et al.* [20] in 2007. Subsequent experiments based on inverted HgTe quantum wells revealed non-local transport in the QSH regime [21] and the spin polarization of the helical edge states [22]. Figure 2.4c sketches the emergence of QSH edge channels with attributed spin orientations for a two-terminal device. Each of the two 1D helical edge channels in transport direction contributes $G_{1D} = e^2/h$ to the conductance, resulting in an overall conductance of

$$G_{QSH} = 2 \cdot G_{1D} = 2e^2/h \tag{2.1}$$

for the indicated device concept. The gapless energy dispersion of the helical edge states is linear at $k = 0$ (see Fig. 2.4d) and is described by $E(k) = \hbar v_F k$, where $\hbar = h/2\pi$ represents the reduced Planck constant and v_F is the Fermi velocity of the QSH edge channels. The crossing of the two branches at $k = 0$ is referred to as Dirac point. While several basic properties of the QSH effect are already experimentally described (as outlined above), it is still an open question how helical edge channels interact when brought in spatial proximity. Such an examination would be enabled by the realization of a QPC technology in a QSH system.

2.2 Quantum point contacts

A QPC is a 1D constriction in an otherwise extended 2D electron or hole system. It exhibits a width in the order of the Fermi wavelength λ_F and is introducing an additional level of confinement in the transversal direction of the 2D system. Since such a constriction connects two wide areas of the underlying 2D layer (equilibrium reservoirs of the QPC) with each other, the basic experimental realization of a QPC is always represented by a two-terminal device concept. Combining this consideration with the 1D character of the constriction is of particular interest, since it entails that some of the fundamental phenomena of ballistic transport are observable in their purest form by examining QPCs [23, 24].

The conventional way to realize QPCs is based on the electrostatic definition of a 1D constriction within a 2DEG. For this purpose, two gate electrodes forming a split gate are patterned on top of a suitable heterostructure (see Fig. 2.5c). By applying a negative voltage to the electrodes, the 2DEG underneath (and consecutively in the vicinity of) the electrodes gets successively depleted, thus narrowing down the remaining part of the 2DEG between the electrodes. As soon as the width of this area becomes sufficiently small, a 1D transport regime emerges.

This transport regime is characterized as ballistic if the elastic mean free path l_e of the electron (average distance between two elastic scattering events) is larger than the relevant

system size L, i.e. $l_\mathrm{e} \gg L$. The elastic mean free path of a 2DEG can be calculated using

$$l_\mathrm{e} = \frac{\hbar \mu_\mathrm{e}}{e} \cdot \sqrt{\frac{4\pi n_\mathrm{e}}{g_\mathrm{s} g_\mathrm{v}}}\,, \tag{2.2}$$

where n_e is the electron density, μ_e the electron mobility and g_s and g_v are the spin and valley degeneracy, respectively. The opposite case of $l_\mathrm{e} \ll L$ is referred to as diffusive transport regime.

Assuming ballistic transport, scattering of electrons at the boundaries of the sample dominates over scattering processes at spatial potential fluctuations [25] and the 1D modes can traverse the QPC unperturbed. In such a scenario, the split gate voltage V_SG controllable width of the QPC is correlated with the number of transmitted 1D transport modes. Thus, tuning the width of the QPC results in an adjustment of the amount of propagating modes and hence in a change of conductance. Each mode – when transmitted fully – contributes a conductance quantum $G_0 = 2e^2/h$ to the overall conductance, resulting in the QPC characteristic conductance quantization exhibiting plateaus spaced by

$$\Delta G = \frac{2e^2}{h}\,. \tag{2.3}$$

In 1988, QPCs haven been successfully realized for the first time on GaAs/AlGaAs heterostructures based on the split gate approach by two groups, independently [26, 27]. Shortly afterwards, an analytical model describing the transport physics of an electrostatically defined QPC was proposed.

2.2.1 Saddle point model

In the framework of the saddle point model developed by *Büttiker* [28], the shape of the potential forming in the centre of the QPC can be approximated by a hyperbolic paraboloid defined by the expression

$$V(x,y) = V_0 + \frac{1}{2} m^* \omega_\mathrm{y}^2 y^2 - \frac{1}{2} m^* \omega_\mathrm{x}^2 x^2\,, \tag{2.4}$$

where the curvatures in transport direction (longitudinal, x direction) and transversal direction (y direction) are described by the parameters ω_x and ω_y, respectively – both with little dependence on the applied split gate voltage. Furthermore, m^* is the effective electron mass and V_0 is the electrostatic potential at the saddle point, which depends linearly on the split gate voltage [29]. The spatial shape of such a saddle point potential is exemplarily presented in Fig. 2.5a.

The potential approximation given by Eq. 2.4 can be solved analytically [28]. The corresponding Hamiltonian is

$$H = \frac{p^2}{2m^*} + V(x,y)\,, \tag{2.5}$$

where $p^2/2m^*$ represents the kinetic energy. The Hamiltonian can be separated with regard to the x and y direction. In the transversal case, an established standard problem of quantum

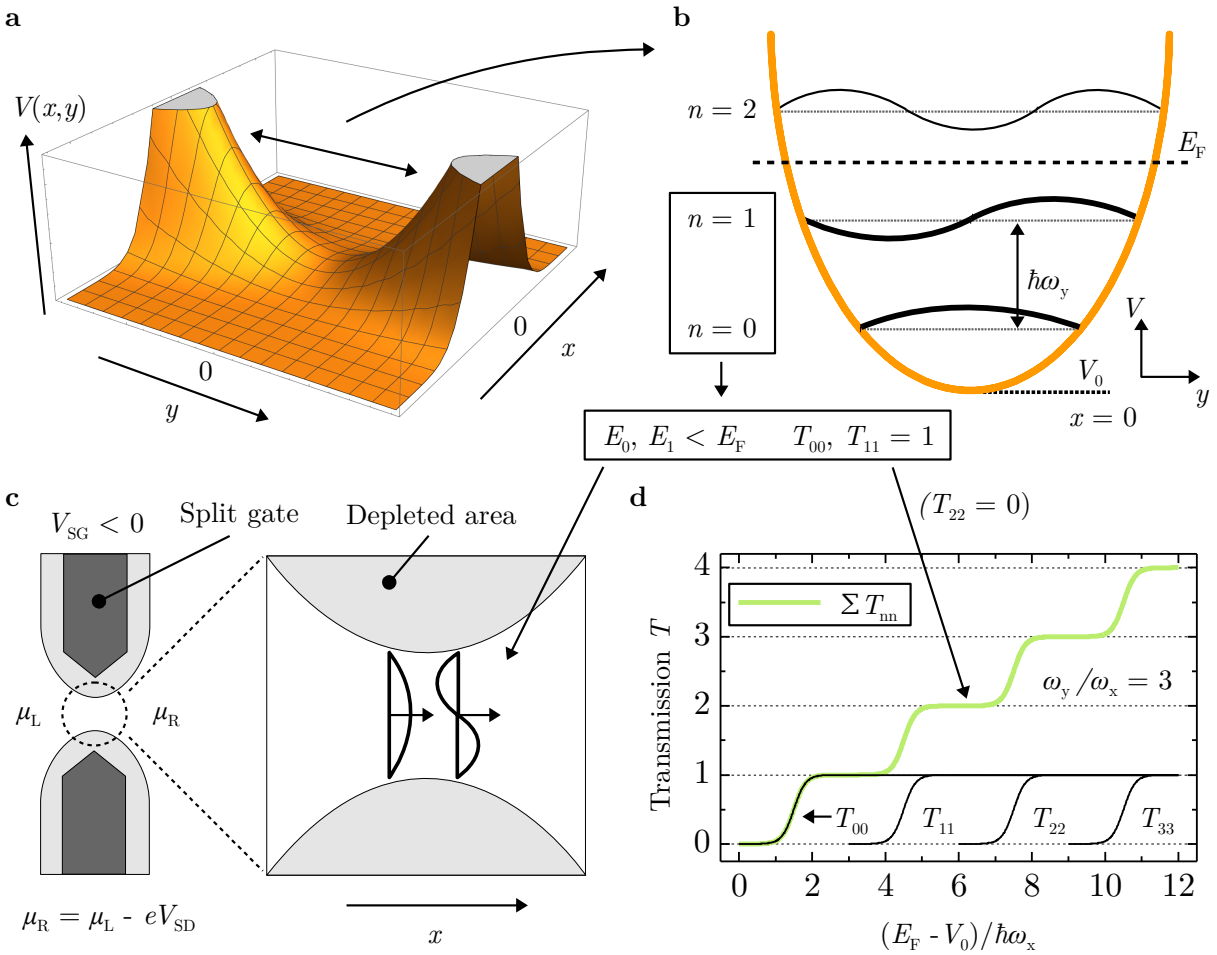

Figure 2.5: **a**, Plot of an exemplary saddle point potential, which forms in the centre of a QPC. **b**, Sketch of the transversal harmonic potential for $x = 0$ and the associated eigenvalues of the energy. In the given example, two modes are fully transmitted, resulting in a conductance of $G = 2 \cdot 2e^2/h = 4e^2/h$. **c**, Cartoon of the transport through a QPC corresponding to the situation sketched in panel **b** and realized by utilizing the split gate technology. The transport modes are schematically illustrated, the arrows depict the propagation direction. The Fermi level μ of the reservoirs is indicated. Adapted from Ref. [25]. **d**, Calculation of the transmission probability through the saddle point potential for the first four subbands ($n = 0, 1, 2, 3$) and of $\sum_{n=0}^{3} T_{nn}$ using Eq. 2.13 with $\omega_y/\omega_x = 3$.

mechanics arises – the harmonic oscillator in a parabolic well. The allowed wave functions in the transversal direction are the eigenmodes of the harmonic oscillator, which are associated with the discrete energy eigenvalues

$$E_n = \hbar\omega_y \left(n + \frac{1}{2}\right) \tag{2.6}$$

with $n \in \mathbb{N}_0$ (see Fig. 2.5b). As a consequence, the wave function in x direction is subject to an effective potential of the form

$$V_{\text{eff}}(x) = V_0 + \hbar\omega_y \left(n + \frac{1}{2}\right) - \frac{1}{2} m^* \omega_x^2 x^2 \,. \tag{2.7}$$

Considering a QPC device with a Fermi energy E_F and neglecting tunnelling effects, there are

$N = n_{\max} + 1$ subbands (also referred to as modes or channels) with

$$E_{\mathrm{n}} = V_0 + \hbar\omega_{\mathrm{y}} \left(n + \frac{1}{2} \right) < E_{\mathrm{F}} \,, \tag{2.8}$$

which are available for electron transport in x direction (see Fig. 2.5b). In order to evaluate the current flow through the 1D constriction (assumption $T = 0\,\mathrm{K}$), the integral of the current density

$$I = e \cdot \sum_{n=0}^{N-1} \int_{E_{\mathrm{F}} - eV_{\mathrm{SD}}}^{E_{\mathrm{F}}} D_{\mathrm{n}}(E) v_{\mathrm{n}}(E) dE \tag{2.9}$$

for all accessible energy values with the assumption of applying a small source-drain voltage V_{SD} is calculated. $D_{\mathrm{n}}(E) = g_{\mathrm{s}} g_{\mathrm{v}} \cdot \frac{1}{2\pi} \frac{dk_{\mathrm{x}}}{dE_{\mathrm{n}}}$ is the density of states (with $g_{\mathrm{s}} = 2$ and $g_{\mathrm{v}} = 1$ for GaAs/HgTe) and $v_{\mathrm{n}}(E) = \frac{1}{\hbar} \frac{dE_{\mathrm{n}}}{dk_{\mathrm{x}}}$ is the group velocity of the present 1D case [24, 30]. Using

$$D_{\mathrm{n}}(E) v_{\mathrm{n}}(E) = \frac{2}{h} \,, \tag{2.10}$$

Eq. 2.9 simplifies to

$$I = \sum_{n=0}^{N-1} \frac{2e}{h} \cdot e \cdot V_{\mathrm{SD}} \,, \tag{2.11}$$

thus yielding an equipartition of the current among N occupied modes (see Fig. 2.5c) [30]. The corresponding conductance term

$$G = \frac{2e^2}{h} \cdot N \tag{2.12}$$

is in qualitative agreement with the experimentally observed quantized split gate voltage dependence of the conductance of QPC devices.

On closer examination, Eq. 2.12 suggests an abrupt steplike increase of the QPC conductance with changing the split gate voltage, whereas experimental data of QPC samples always exhibits a rather smooth transition between two consecutive conductance plateaus. In this context, it becomes necessary to include the circumstance of quantum mechanical transmission and reflection through the saddle point potential to the analytical description of QPC transport. This is accomplished by using the so-called *Wentzel-Kramers-Brillouin* (WKB) approximation. For a deeper insight, the interested reader is referred for example to Ref. [29].

Applying the WKB approximation to the discussed scenario results in a transmission probability $T_{\mathrm{mn}}(E)$ for every individual subband

$$T_{\mathrm{mn}}(E) = \delta_{\mathrm{mn}} \frac{1}{1 + \exp(-\pi\varepsilon_{\mathrm{n}})} \;,\; \varepsilon_{\mathrm{n}} = \frac{2\left[E - \hbar\omega_{\mathrm{y}} \left(n + \frac{1}{2} \right) + V_0 \right]}{\hbar\omega_{\mathrm{x}}} \,. \tag{2.13}$$

It should be noted that only if the incident channel and the outgoing channel are the same, non-zero transmission probabilities can arise [28]. Figure 2.5d shows the calculated transmission probability through the saddle point potential for the first four subbands ($n = 0, 1, 2, 3$) and

of $\sum_{n=0}^{3} T_{\mathrm{nn}}$ using Eq. 2.13 with $\frac{\omega_{\mathrm{y}}}{\omega_{\mathrm{x}}} = 3$. The smooth transition between two consecutive conductance plateaus is in accordance with experimental data. The transition width is set by the energy scale $\hbar\omega_{\mathrm{x}}$, whereas the energy shift between two consecutive plateaus is defined by $\hbar\omega_{\mathrm{y}}$ [25].

For the sake of completeness, the factor $T_{\mathrm{nn}}(E)$ also has to be included within Eq. 2.9, which results in the adjusted form

$$I = e \cdot \sum_{n=0}^{N-1} \int_{E_{\mathrm{F}}-eV_{\mathrm{SD}}}^{E_{\mathrm{F}}} D_{\mathrm{n}}(E) v_{\mathrm{n}}(E) T_{\mathrm{nn}}(E) dE \,. \tag{2.14}$$

However, the mathematical treatment stays the same if merely small source-drain voltages are applied (linear regime). In this case, $T_{\mathrm{nn}}(E)$ is roughly constant within the corresponding energy window and can thus be replaced by $T_{\mathrm{nn}}(E_{\mathrm{F}})$ [25, 31]. Finally, adjusting Eq. 2.12 results in the term

$$G = \frac{2e^2}{h} \sum_{n=0}^{N-1} T_{\mathrm{nn}} \,, \tag{2.15}$$

where T_{nn} represents the transmission probability for each individual subband. Equation 2.15 is usually referred to as the *Landauer formula*, which represents the fundamental law of mesoscopic transport physics – the relation between conductance and transmission probabilities at the Fermi energy [23, 31, 32].

2.2.2 Technological variations

The tuning of the conductance in the framework of the split gate approach is based on adjusting the height of the saddle point relative to a given level of the Fermi energy (see Fig. 2.5b). This modification is induced by a split gate voltage controllable change of the constriction width. In this context, an alternative method to realize QPC devices is represented by the etching of mesa structures with dimensions in the order of the Fermi wavelength. In such a scenario, the minimal device width W_{QPC} and (in approximation) the potential landscape are constant. Hence, the definition of a top gate electrode is necessary in order to be able to tune the Fermi energy relative to a given potential and thus to modify the conductance of the QPC.

Concerning the overall geometry of QPCs, two types of device realizations can be distinguished. A gradual confinement of the 2DEG to a 1D constriction is described as an adiabatic QPC [33, 34], while a sudden confinement is defined as an abrupt QPC [35]. The advantage of the adiabatic approach is related to the smooth variation of the constriction width, which ensures a reflectionless matching of electron states within the transition area between the 2D reservoirs and the 1D constriction [33]. QPC devices based on electrostatic definition using the split gate approach as well as etched constrictions utilizing a wet chemical etching process can both be characterized as adiabatic.

Since the seminal works of *van Wees et al.* [26] and *Wharam et al.* [27], QPCs have been realized in various semiconductor systems. However, GaAs based devices still represent the

benchmark regarding material and device quality. Recently, QPCs have also been implemented in graphene [36, 37] and oxide heterostructures [38, 39].

2.2.3 Realization in a quantum spin Hall system

As pointed out in Chapter 1, the realization of a QPC technology in a QSH system is a long time awaited achievement. Such a device would represent a ground-breaking development, since it would act as a basic building block for multiple novel experiments. However, the unique existence of helical edge channels poses certain challenges concerning the implementation of a QPC in a 2D-TI system.

Limitations of the split gate approach

Pure helical edge channel transport is only observable within the bulk band gap. Thus, a device realization which enables the tuning of the Fermi energy of the QPC area from the conduction band across the band gap to the valence band is required. The split gate approach sketched in Fig. 2.6a cannot meet this condition, since the latter is conceptually unsuitable to realize a 1D transport situation in different transport regimes of the same sample.

Furthermore, it is still unclear if the split gate approach is a feasible option for HgTe quantum wells at all. Due to the small bulk band gap of HgTe, the split gate approach might lead to a situation in which the depleted areas of the HgTe 2DEG underneath the electrodes start to enter the valence band regime, while the constriction between the two split gate electrodes still exhibits a finite width and thus is still hosting 1D electron transport. Such a scenario would then result in parasitic parallel conductance and hence prevent any observability of conductance quantization.

However, the main reason why the split gate approach is not utilizable for the envisaged experiments within the scope of this thesis is related to the nature of helical edge channels. As explicated earlier, helical edge channels emerge at the boundary of two topologically different materials where the Dirac mass changes its sign. This topological transition always takes place at the physical edge of a device and cannot be moved towards the bulk of a device, for example by the influence of an electric field – a misconception sometimes present in theoretical publications. As a consequence, a hypothetical device realization of a QPC in a QSH system using the split gate approach would not exhibit the requested spatial proximity of the helical edge channels (see Fig. 2.6a).

Top gate approach

In order to overcome this obstacle, the QPC has to be defined by bringing the physical device edges – and thus also the QSH edge states – in spatial proximity, which is sketched in Fig. 2.6b. In other words, the QPC has to be defined by etching a mesa instead of utilizing electrostatic depletion of an unstructured 2DEG. However, it is important to note that for the case of HgTe quantum wells, the chosen etching method is an important factor regarding device quality. In the past, HgTe based QPCs realized using dry etching techniques did not exhibit pronounced

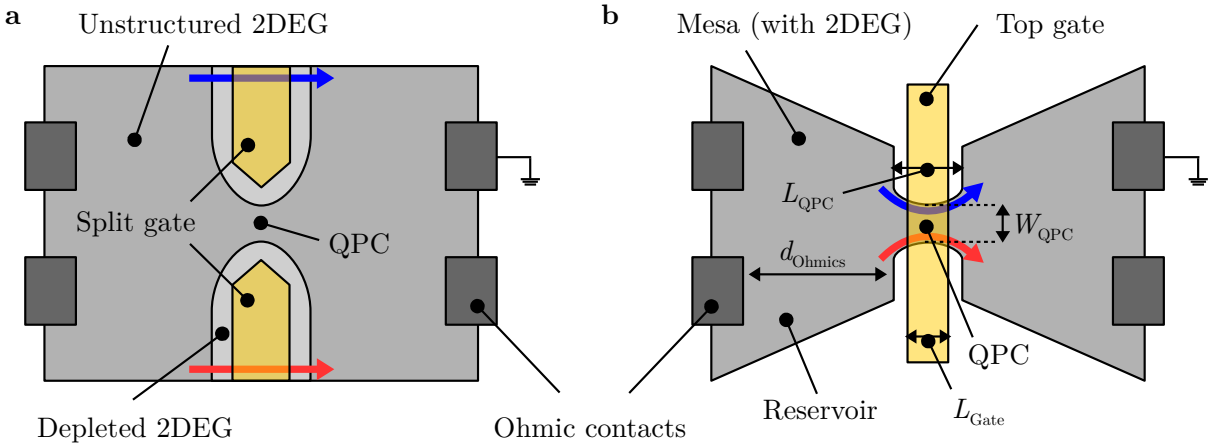

Figure 2.6: **a**, Sketch of a QPC realized in a QSH system based on the split gate approach. The dimensions of the QPC are not constant, since they depend on the extent of the depleted 2DEG area. **b**, Sketch of a QPC realized in a QSH system based on the definition of an etched mesa. The QPC, which exhibits a minimal width W_{QPC} and a length L_{QPC}, is covered by a top gate electrode with a length L_{Gate}. In both sketched scenarios, the helical edge states are located at the physical device edges.

QPC quantization or indications for the presence of the QSH regime [40]. Later, it was found out that the utilized dry etching process caused local doping of the device edges, which reduced the carrier mobility especially in small structures drastically. This gain of insight initiated the implementation of a device quality preserving wet etching process for HgTe devices [41, 42], which was also utilized for sample fabrication within the scope of this thesis.

A QPC based on an etched mesa realized in a QSH system is sketched in Fig. 2.6b. The constriction is characterized by its length L_{QPC} and its width W_{QPC}, which is determined by the smallest distance of the mesa edges. A top gate electrode with a length L_{Gate} is centrally patterned on top of the QPC mesa. Since $L_{Gate} < L_{QPC}$, the length of the gate electrode defines the relevant length scale of the QPC in terms of transport experiments. By applying a voltage to the gate electrode, the Fermi energy of the gated region can be tuned from the conduction band across the band gap to the valence band, while the adjacent ungated areas (reservoirs) unaffectedly remain n-type – the n represents an electron dominated transport regime, the hole equivalent is referred to as p-type. Accordingly, the QPC device has to be described as a ballistic junction with three different transport regimes: the n-n'-n, the n-i-n and the n-p-n regime.

2.3 Lithographic fabrication of HgTe based quantum point contacts

The introduced device concept of an etched QPC mesa covered with a top gate electrode results in two requirements for the to be utilized fabrication process. First, the etching of the QPC has to be controllable and reproducible, which implies a to be established fixed link between between a priori defined design dimensions and post-fabrication QPC dimensions. Second, the top gate electrode should only cover the central part of the etched constriction. Otherwise, also

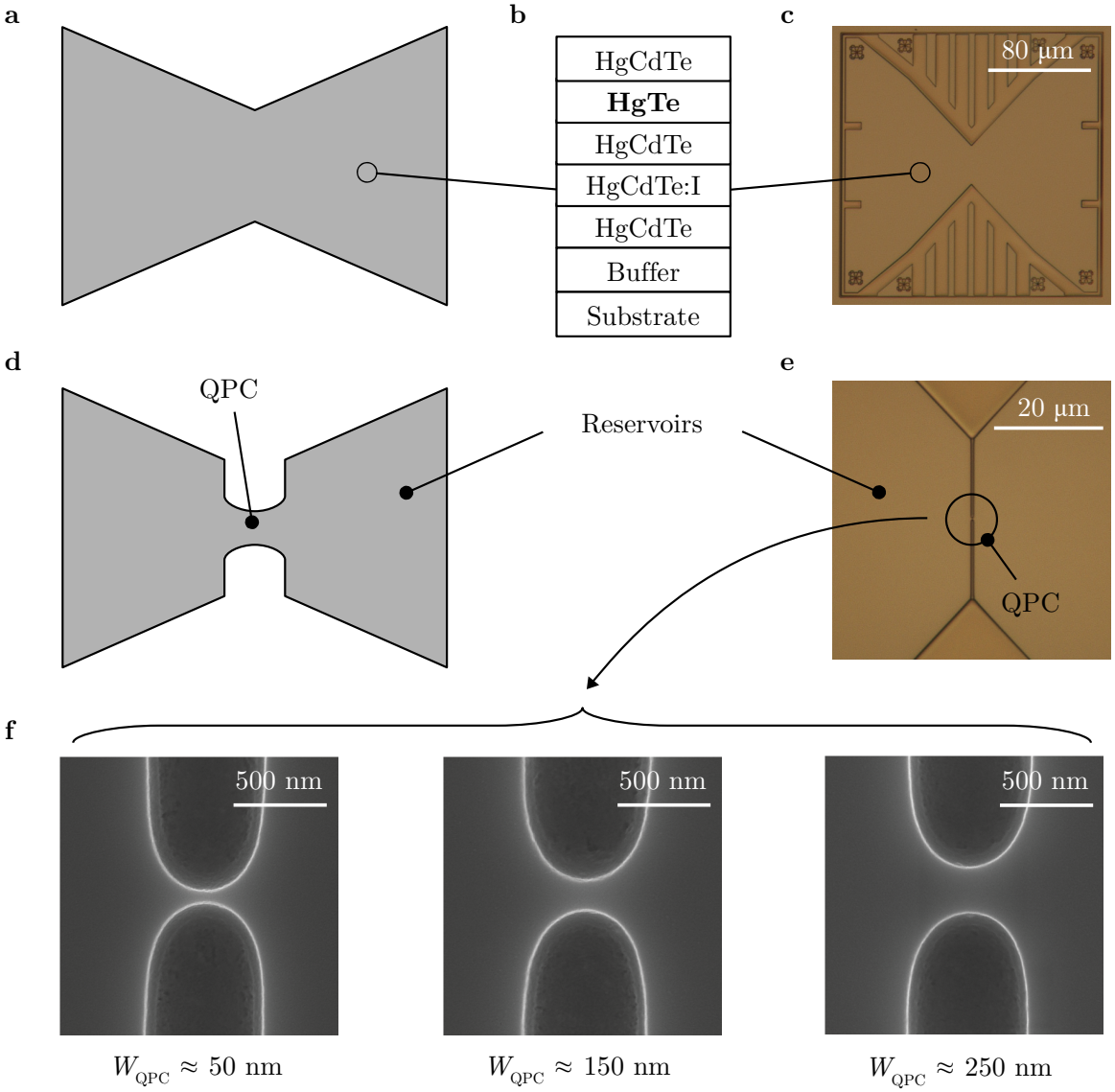

Figure 2.7: **a**, **c**, Sketch and optical micrograph of the first mesa etching step, which forms the equilibrium reservoirs of the QPC. **b**, Qualitative schematic of the full layer stack of the HgTe quantum wells used in this thesis. **d**, **e**, Sketch and optical micrograph of the second mesa etching step, which defines the QPC. **f**, Scanning electron micrographs of exemplary QPC devices with different values of the width W_{QPC}.

the adjacent 2DEG areas on both sides of the QPC would be gated, thus causing a non-linear background in the measurement of the gate voltage dependence of the QPC conductance.

The realization of these two prerequisites was the main subject of the lithography development done within the scope of this thesis. Both tasks have been solved successfully, which will be presented in the following. In order to fabricate QPC devices, standard optical lithography as well as electron beam lithography (EBL) methods were utilized. The detailed process parameters are added to Appendix A.

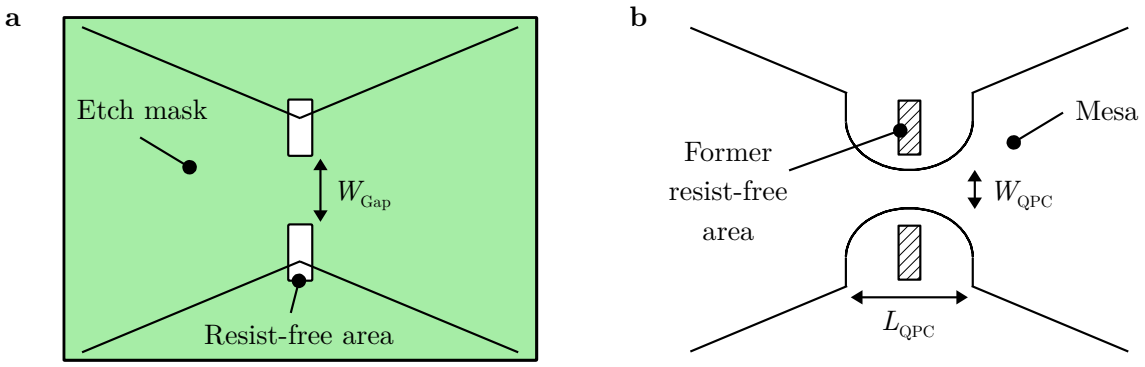

Figure 2.8: Sketch of the relation between the dimensions of the QPC etch mask (panel **a**) and the etched QPC (panel **b**).

Etching of the mesa

The mesa of the QPC devices is defined utilizing a wet etching process based on an aqueous solution of KI : I_2 : HBr. To guarantee a constant flow of etchant on the sample surface, a setup is utilized which allows to control the flow rate of the solution by using an adjustable pump. For further details, the interested reader is referred to Refs. [41, 42]. In order to ensure controllability of the QPC dimensions, the fabrication of the main mesa (referred to as inner mesa) is separated into two parts.

In the first step, only the equilibrium reservoirs surrounding the to be defined QPC are structured, which is shown in Fig. 2.7a,c. Subsequently, the QPC is formed in a second lithography step (see Fig. 2.7d,e). The etch masks for defining both mesa parts are patterned by using EBL. A qualitative schematic of the full layer stack of the HgTe quantum wells used for QPC fabrication is presented in Fig. 2.7b.

The reason for separating both etching steps is related to the presence of the diffusive etching regime [42]. In this case, the etching rate is indirectly related to the dimensions of the etch mask. Thus, the etching within the to be defined QPC area takes place at a higher rate than for example in the device segments of the to be defined equilibrium reservoirs. Hence, it is not possible to define both mesa parts in one combined etching step, since there is no overall etching time which would ensure satisfying etching results for all parts of the sample.

Another factor to be considered is the isotropic etching behaviour of the utilized wet etching process [42]. The latter causes lateral etching, which results in smaller values of the width W_{QPC} and larger values of the length L_{QPC} of the constriction than specified a priori by the chosen design dimensions (see Fig. 2.8). The extent of the lateral etching depends on different parameters like etching time or mask dimensions and has to be quantified via several introductory test samples. For the equilibrium reservoirs, the influence of lateral etching is negligible.

Using the developed process, it is possible to reproducibly fabricate constrictions with a minimal step width of $\Delta W_{\mathrm{QPC}} \approx 50\,\mathrm{nm}$. In this context, Fig. 2.7f shows scanning electron micrographs of exemplary QPC devices with different width values W_{QPC}. In all cases, the length of the QPC is $L_{\mathrm{QPC}} \approx 500\,\mathrm{nm}$. It should be noted that the controllable and reproducible definition

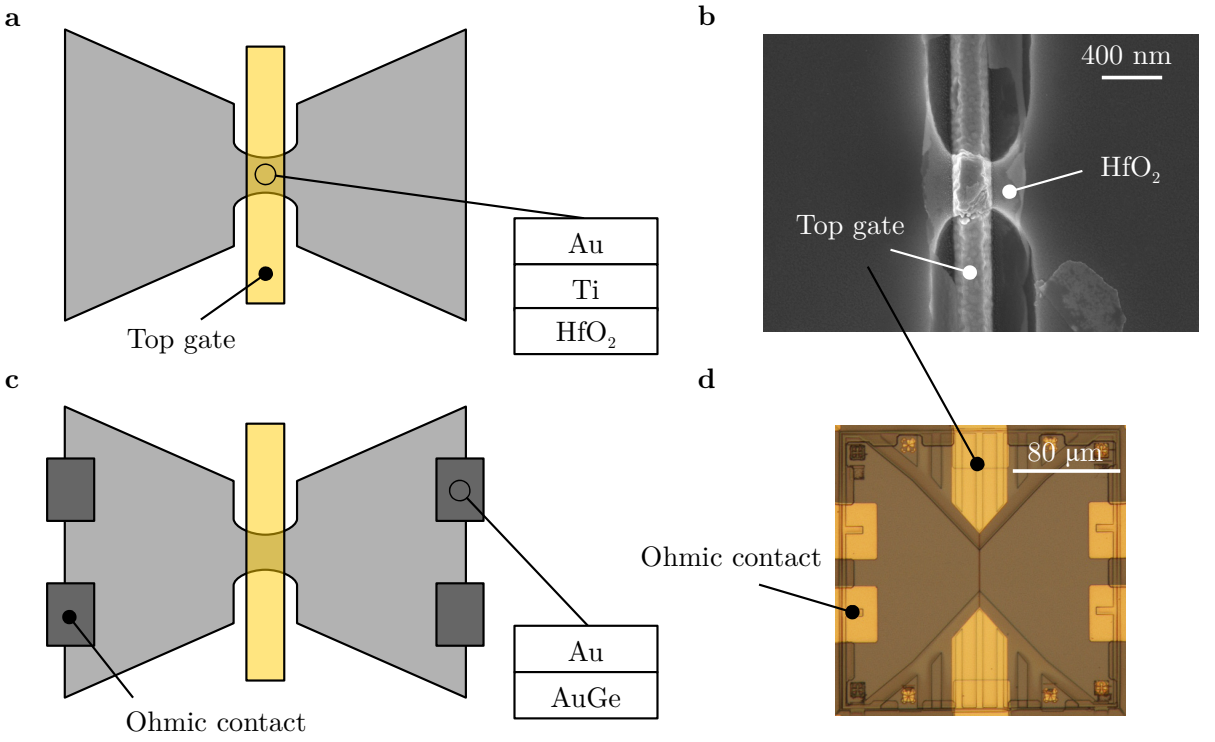

Figure 2.9: **a**, **b**, Sketch and scanning electron micrograph of a QPC covered by a top gate electrode. The layer stack of the gate electrode is indicated. **c**, **d**, Sketch and optical micrograph of a final QPC device. The layer stack of the ohmic contacts is indicated.

of nanometre scale constrictions via a wet etching process is a technological breakthrough not achieved before (see for example Ref. [43]).

After the inner mesa is defined, the surrounding and so far unstructured sample areas have to be etched. This so-called outer mesa consists of segments to be acting as gate leads, as ohmic contacts and as bonding pads (see Fig. 2.10b). Since the required level of resolution and accuracy is lower in this final etching step, optical lithography is used to pattern the etch mask.

Definition of the gate electrode and ohmic contacts

The next lithography step deals with patterning the top gate electrode using EBL, which is sketched in Fig. 2.9a. To ensure a high yield of working QPC devices, several aspects have to be taken into account. First, in order to prevent cracks within the gate electrode along the mesa edges, a sufficiently thick Ti/Au stack has to be metallized. Being able to deposit a metal stack of high thickness requires a long-chain polymethyl methacrylate (PMMA) resist system with regard to the subsequent lift-off. The reason is that a long-chain PMMA system exhibits a higher resist layer thickness than alternatives with a smaller chain length (assuming identical spin-coating and baking parameters). Furthermore, to ensure a complete development of the exposed area, a short ultrasonic pulse is included in the development process after the EBL exposure. Afterwards, the risk of remaining parasitic PMMA residues within the resist-free area is further reduced by treating the sample with a short oxygen plasma.

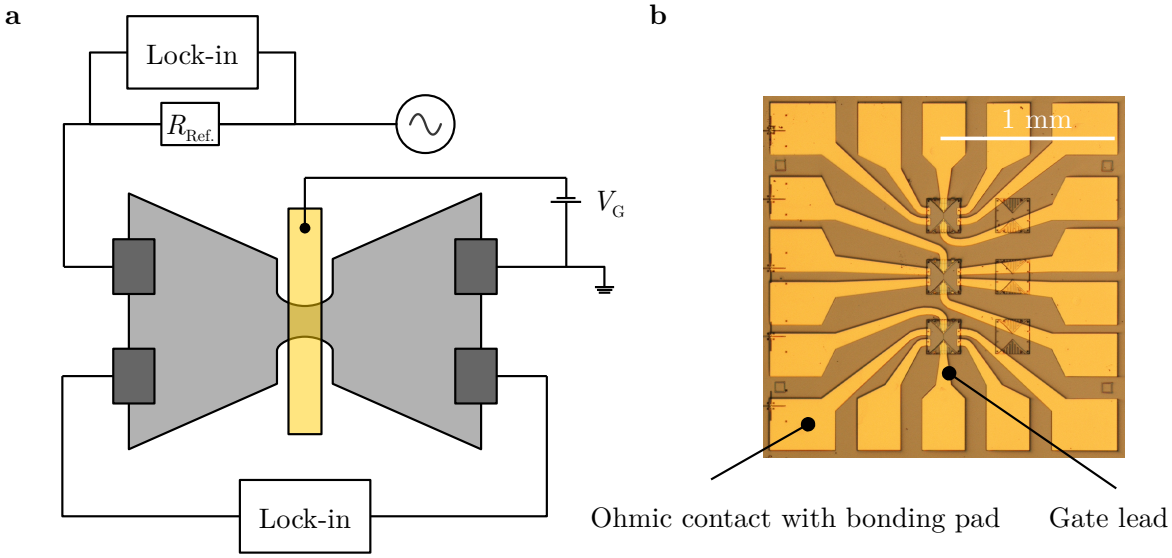

Figure 2.10: **a**, Schematic of the utilized measurement setup. **b**, Optical micrograph of a full sample, which exhibits three single QPC devices.

Subsequent to this preparative step, a low temperature ($T < 40\,^{\circ}\text{C}$) atomic layer deposition (ALD) process is utilized to deposit a film of HfO_2, which serves as a dielectric. Lastly, the Ti/Au stack is metallized. Figure 2.9b shows a scanning electron micrograph of an exemplary QPC covered by a top gate electrode. The length of the gate electrode is $L_{\text{Gate}} \approx 250\,\text{nm}$, similar for all standard QPC samples presented within the scope of this thesis.

The device is finalized by patterning ohmic contacts (AuGe/Au stack) using common optical lithography methods (see Fig. 2.9c,d). The ohmic contacts are placed far away from the centre of the QPC ($d_{\text{Ohmics}} \approx 80\,\mu\text{m} > 10 \times l_{\text{e}}$) in order to allow for full energy relaxation in the reservoirs and to avoid geometrical resonances. The width of the ohmic contacts increases towards the outer samples areas. There, the ohmic contacts terminate forming the so-called bonding pads (see Fig. 2.10b). The latter enable the usage of convenient wedge-wedge bonding techniques after the finalized sample is glued to a chip carrier. In addition to the ohmic contacts, also the EBL defined gate electrode requires a wedge-wedge bonding suited extension towards the outer sample areas. These so-called gate leads (see Fig. 2.10b) can be patterned together with the ohmic contacts or in a dedicated process step.

2.4 Transport characterization of HgTe based quantum point contacts

All devices presented within the scope of this thesis were fabricated from HgTe quantum wells epitaxially grown on CdZnTe substrates and sandwiched between HgCdTe barriers (see Fig. 2.7b). An iodine doping layer increases the overall electron density of the quantum well and is thus reducing the serial resistance of the reservoirs. The layer thicknesses of the utilized heterostructures are quantified using X-ray diffraction analysis and the relevant material

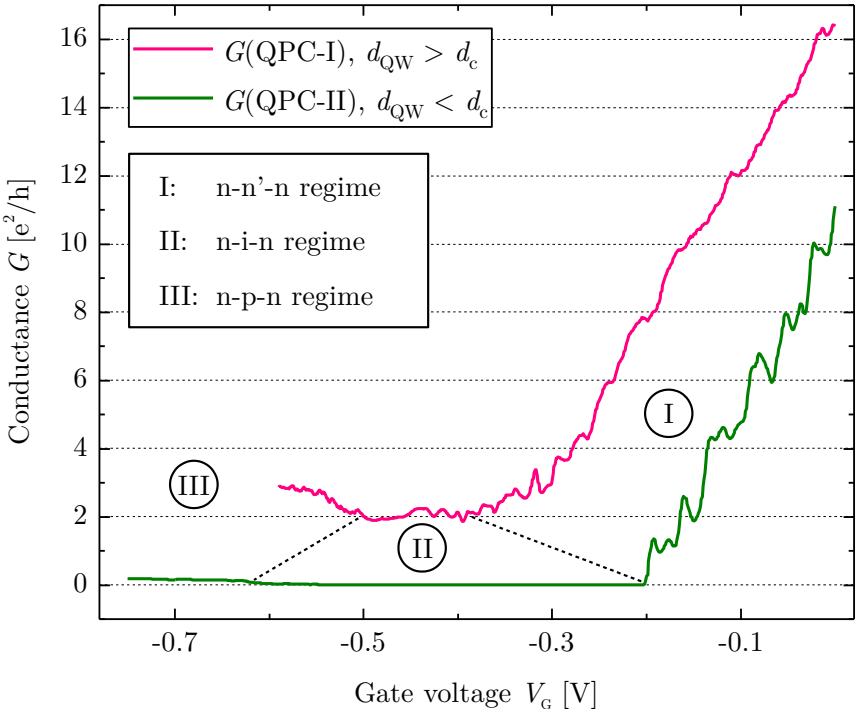

Figure 2.11: Gate voltage V_G dependence of the conductance G of QPC-I ($d_{QW} > d_c$) and QPC-II ($d_{QW} < d_c$). The conductance is divided into three regimes indicated by the dashed lines and the Roman numerals (I: n-n'-n, II: n-i-n and III: n-p-n regime). A serial resistance of $R_{Serial} = 260\,\Omega$ for QPC-I and $R_{Serial} = 1650\,\Omega$ for QPC-II is subtracted. In both cases, the width of the QPC is $W_{QPC} \approx 100\,nm$.

parameters are deduced from measurements of reference Hall bar samples. The device and material parameters of all samples discussed within the course of this thesis are presented in dedicated tables at the end of each chapter.

The transport measurements were performed in helium-4 cryostats at a temperature of $T = 1.4\,K$ using standard 4-point low frequency low bias lock-in techniques. A sketch of the corresponding measurement setup is shown in Fig. 2.10a. Complementary measurements presented in Chapter 4 were conducted in a dilution refrigerator with a base temperature of $T = 25\,mK$. An optical micrograph of a full sample is presented in Fig. 2.10b. Every QPC device is attached to four ohmic contacts and every top gate electrode is connected to two gate leads.

2.4.1 Comparison of topological and trivial devices

The conductance G as a function of gate voltage V_G of a topological (QPC-I) and a trivial (QPC-II) device of similar width ($W_{QPC} \approx 100\,nm$) is shown in Fig. 2.11. A serial resistance of $R_{Serial} = 260\,\Omega$ is subtracted for QPC-I and a value of $R_{Serial} = 1650\,\Omega$ is subtracted for the case of QPC-II (see also Appendix B). The higher subtracted value for QPC-II stems from the lower electron mobility (see Tab. 2.1), which causes a higher serial resistance of the ungated sample areas. The latter is related to the conception of QPC devices, which allows for transport experiments only in local 4-point measurement geometries. Thus, the resistive contribution of

both reservoirs $R_{\mathrm{Serial}} = 2 \cdot R_{\mathrm{Reservoir}}$ is added to the resistance of the QPC, which is described by $R = 1/N \cdot h/2e^2 + R_{\mathrm{Serial}}$.

For both devices, conductance steps of integer values of $\Delta G \approx 2e^2/h$ can be identified with decreasing gate voltage values within the n-n'-n regime. The reduced cleanness of the plateaus for QPC-II can be attributed to the lower material quality of the trivial quantum well, which for example increases the probability of scattering centres to be located within the vicinity of the QPC. The conductance saturates around $G_{\mathrm{QSH}} \approx 2e^2/h$ for QPC-I with entering the n-i-n regime, while it drops to $G \approx 0$ for QPC-II. For the case of QPC-I, the residual conductance of $G_{\mathrm{QSH}} \approx 2e^2/h$ demonstrates the presence of the QSH state, whereas a real gap and thus suppressed transport is observed for QPC-II. For even more negative gate voltages, slightly increasing conductance values for both devices are associated with entering the n-p-n regime. The slow increase of conductance in the n-p-n regime is attributed to the low mobility for p-conduction and the wave function mismatch between n- and p-conducting states [44]. The observed characteristics of all three transport regimes are consistent with predictions by Ref. [44].

The presence of conductance quantization in the n-n'-n regime of QPC-I and QPC-II indicates ballistic 1D transport through the QPC. The ballistic condition

$$l_{\mathrm{e}} \gg L_{\mathrm{Gate}} \approx 250\,\mathrm{nm} \tag{2.16}$$

is met for the topological as well as for the trivial device (see Tab. 2.1). In this context, Fig. 2.12a–c shows the gate voltage dependence of the conductance of the topological devices QPC-III, QPC-IV and QPC-V. For all three samples, the conductance decreases within the n-n'-n regime and saturates around the residual conductance of $G_{\mathrm{QSH}} \approx 2e^2/h$ within the n-i-n regime. Regarding the n-n'-n regime, only QPC-III and QPC-V exhibit the emergence of plateaus due to ballistic 1D transport (subtraction of a serial resistance of $R_{\mathrm{Serial}} = 150\,\Omega$ and $R_{\mathrm{Serial}} = 1450\,\Omega$, respectively), whereas no conductance quantization can be identified for the case of QPC-IV. However, as shown in Tab. 2.1, the condition formulated by Eq. 2.16 is met for all three devices.

A possible reason to explain the absence of quantization caused by ballistic 1D transport for the case of QPC-IV is provided by Ref. [45]. There, the authors predict that random long-range potential fluctuations within QPC devices based on doped heterostructures could lead to the breakdown of conductance quantization – even though if ballistic transport conditions would be expected from reference characterization measurements. This circumstance can then lead to pronounced variations in transport between nominally identical devices [45].

Moreover, a further argument is related to intrinsic material quality fluctuations of the underlying HgTe quantum well. Since the values of electron density and electron mobility are obtained by analysing standard Hall bars, they result from averaging transport properties of an area of $A = L_{\mathrm{HB}} \cdot W_{\mathrm{HB}} \approx (600 \cdot 200)\,\mu\mathrm{m}^2$. For QPC-IV, the transport behaviour of the whole device is determined by a gated area of merely $A = L_{\mathrm{Gate}} \cdot W_{\mathrm{QPC}} \approx (250 \cdot 200)\,\mathrm{nm}^2$, thus making quality deviations in both directions off the Hall bar benchmark value plausible. Areas of the

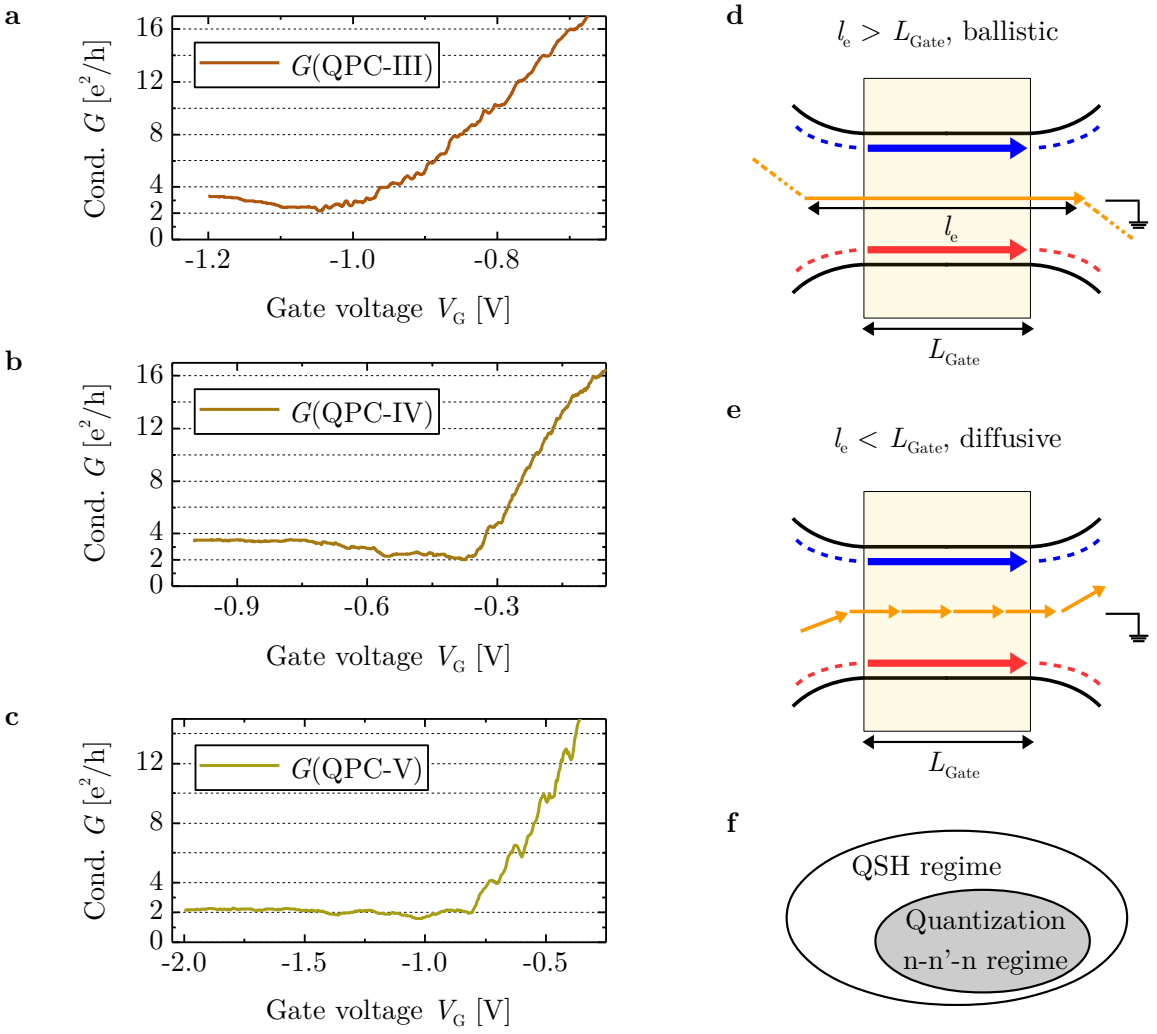

Figure 2.12: **a**–**c**, Gate voltage V_G dependence of the conductance G of QPC-III ($W_{QPC} \approx 150\,nm$), QPC-IV ($W_{QPC} \approx 200\,nm$) and QPC-V ($W_{QPC} \approx 250\,nm$). For QPC-III and QPC-V, a serial resistance of $R_{Serial} = 150\,\Omega$ and $R_{Serial} = 1450\,\Omega$ is subtracted, respectively. **d**, **e**, Sketch of trivial ballistic and diffusive 1D transport through a topological QPC. **f**, Observed interrelations of the emergence of transport regimes in topological QPC devices.

2DEG with more pronounced disorder would then nullify the met ballistic condition of Eq. 2.16 with passing a certain threshold level concerning material quality, whereas QSH edge channel transport would remain unaffected due to topological protection (sketched in Fig. 2.12d,e).

The latter is of particular interest, since it implies that the QSH regime can emerge despite an overall diffusive transport regime. This assumption is backed by the fact that the QSH regime is always present when observing quantization due to ballistic 1D transport, while the reverse conclusion is not true (see QPC-IV). Moreover, the hypothetical case of quantization due to ballistic 1D transport without an identifiable QSH regime is not observed within the scope of this thesis (excluding edge channel hybridization). These interrelations are visualized in Fig. 2.12f. Lastly, the reasoning of intrinsic material quality fluctuations also accounts for the larger to be subtracted serial resistance value for the case of QPC-V than for the other topological devices.

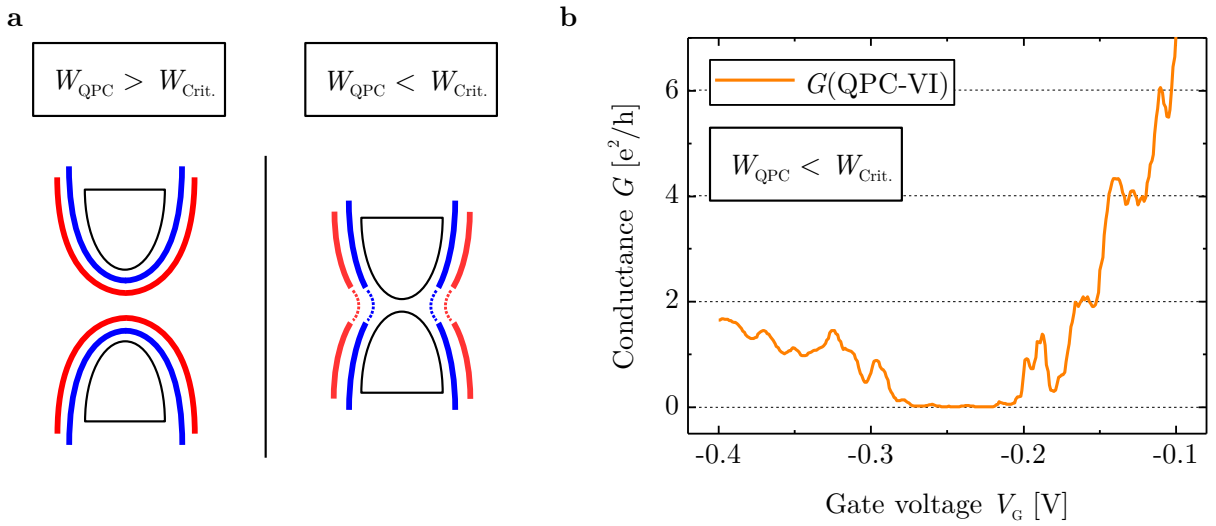

Figure 2.13: **a**, Sketch of two topological QPC devices. When the width of the QPC drops below a threshold value $W_{\text{Crit.}}$, the QSH edge channel wave functions hybridize, thus leading to suppressed topological conductance within the QPC. **b**, Gate voltage V_G dependence of the conductance G of QPC-VI ($d_{QW} > d_c$). A serial resistance of $R_{\text{Serial}} = 1600\,\Omega$ is subtracted. The width of QPC-VI is $W_{QPC} \approx 50\,\text{nm}$.

2.4.2 Conductance of a narrow topological device

For narrow QPC devices with $W_{QPC} < W_{\text{Crit.}} \approx 75\,\text{nm}$, the occurrence of pronounced hybridization effects due to the mixing of the QSH edge channel wave functions is predicted by Ref. [46]. There, the authors argue that such samples are characterized by the suppression of topological conductance, which is sketched in Fig. 2.13a. The latter causes a drop of the overall conductance to $G \approx 0$ within the n-i-n regime – despite the topological nature of the underlying HgTe quantum well [46].

Figure 2.13b shows the gate voltage dependence of the conductance of QPC-VI. The device is fabricated from a quantum well with $d_{QW} > d_c$ and exhibits a width of $W_{QPC} \approx 50\,\text{nm}$, thus $W_{QPC} < W_{\text{Crit.}}$. A serial resistance of $R_{\text{Serial}} = 1600\,\Omega$ is subtracted. In agreement with the data of QPC-I, conductance steps of integer values of $\Delta G \approx 2e^2/h$ can be identified within the n-n'-n regime with decreasing gate voltage values. However, contrary to QPC-I, the conductance does not saturate at $G_{QSH} \approx 2e^2/h$ within the n-i-n regime, but drops to $G \approx 0$. This behaviour is attributed to the afore outlined hybridization effects of the QSH edge channel wave functions in narrow QPC devices. The increase of conductance for even more negative gate voltages is associated with entering the n-p-n regime.

In this context, the presence of unperturbed QSH quantization for QPC-I ($W_{QPC} \approx 100\,\text{nm}$) provides an upper limit regarding the width W_{HEC} of the helical edge channels. Furthermore, the discussed transport behaviour of QPC-VI ($W_{QPC} \approx 50\,\text{nm}$) contributes to define a lower limit. Combining both reference points thus enables an estimation of the width of one helical edge channel, which yields $25\,\text{nm} < W_{HEC} < 50\,\text{nm}$ for quantum wells with $d_{QW} = 7\,\text{nm}$.

A recent report estimated the width of the helical edge channels by employing the superconducting diffraction pattern of a topological Josephson junction to be $W_{HEC} \geq 180\,\text{nm}$ [47],

which is considerably larger than the upper limit of the afore presented range. Other imaging techniques like microwave impedance mismatch [48], scanning squid [49] as well as scanning gate [50] experiments seem to give an even wider estimate of the QSH edge channel wave function width. Adjusting the width of a QPC thus is to date the most accurate experimental method to estimate the width of helical edge channels.

2.4.3 Trivial one-dimensional transport in a topological device

In order to establish a profound picture of QPC devices in QSH systems, it is also necessary to analyse the trivial ballistic 1D transport behaviour in such devices. The work of *Büttiker* [28] contributed to the understanding of the trivial conductance through a QPC by means of transmitted quantum channels (or subbands). Temperature dependent transport data can be utilized to approximate the energetic spacing ΔE of these subbands, which is referred to as subband spacing. Since the width of the thermal smearing function $\mathrm{d}f/\mathrm{d}E_\mathrm{F}$ is approximately $4k_\mathrm{B}T$ (k_B is the Boltzmann constant), the conductance quantization within the n-n'-n regime is expected to vanish for $T \gtrapprox \Delta E/4k_\mathrm{B}$ [23]. In this context, the gate voltage dependence of the conductance of QPC-I for different values of the temperature is presented in Fig. 2.14a. The quantization due to trivial ballistic 1D transport disappears between $T = 4.2\,\mathrm{K}$ and $T = 10\,\mathrm{K}$, thus yielding a range of the subband spacing of $1.4\,\mathrm{meV} < \Delta E < 3.4\,\mathrm{meV}$.

A second method to quantify the subband spacing was first discussed by *Patel et al.* [51]. There, the authors explicated that the application of a sufficiently high direct current (DC) bias voltage V_DC over a QPC device results in an aligning of the Fermi level[2] of the source with one subband, while the Fermi level of the drain is aligned with the subsequent subband. The latter induces the emergence of plateaus in the differential conductance $\mathrm{d}I/\mathrm{d}V$ of the device at odd integer values of e^2/h. The position of these plateaus with regard to the applied bias voltage can then directly be related to the subband spacing of the examined QPC device [51–53].

The bias voltage dependence of the differential conductance of QPC-I for different values of the gate voltage is shown in Fig. 2.14b. The formation of plateau-like shapes for $\mathrm{d}I/\mathrm{d}V > 2e^2/h$ can be observed for bias voltages between $V_\mathrm{DC} \approx 2.2\,\mathrm{mV}$ and $V_\mathrm{DC} \approx 3.2\,\mathrm{mV}$ (pink circles), hence yielding a subband spacing of $2.2\,\mathrm{meV} < \Delta E < 3.2\,\mathrm{meV}$ and thus narrowing down the afore determined range. Beyond that, the deduced values are comparable with those of electrostatically defined QPC devices in GaAs based 2DEGs (see for example Ref. [54]).

The similarity between trivial and topological QPC devices reveals itself even more in a further context. It should be noted that for a QSH system, the conductance of the n-n'-n regime of a QPC sample is offset by $\Delta G \approx 2e^2/h$ due to the residual conductance of the helical edge channels. Thus, the so-called sub-open regime, which emerges below the first subband and hence for $G \in [0; 2]\, e^2/h$ in trivial devices, occurs for $G \in [2; 4]\, e^2/h$ in topological devices. For trivial QPC devices, this peculiar transport regime exhibits a frequently observed plateau-like shape under bias and/or

[2] Note that the Fermi level at $T = 0\,\mathrm{K}$ is the Fermi energy.

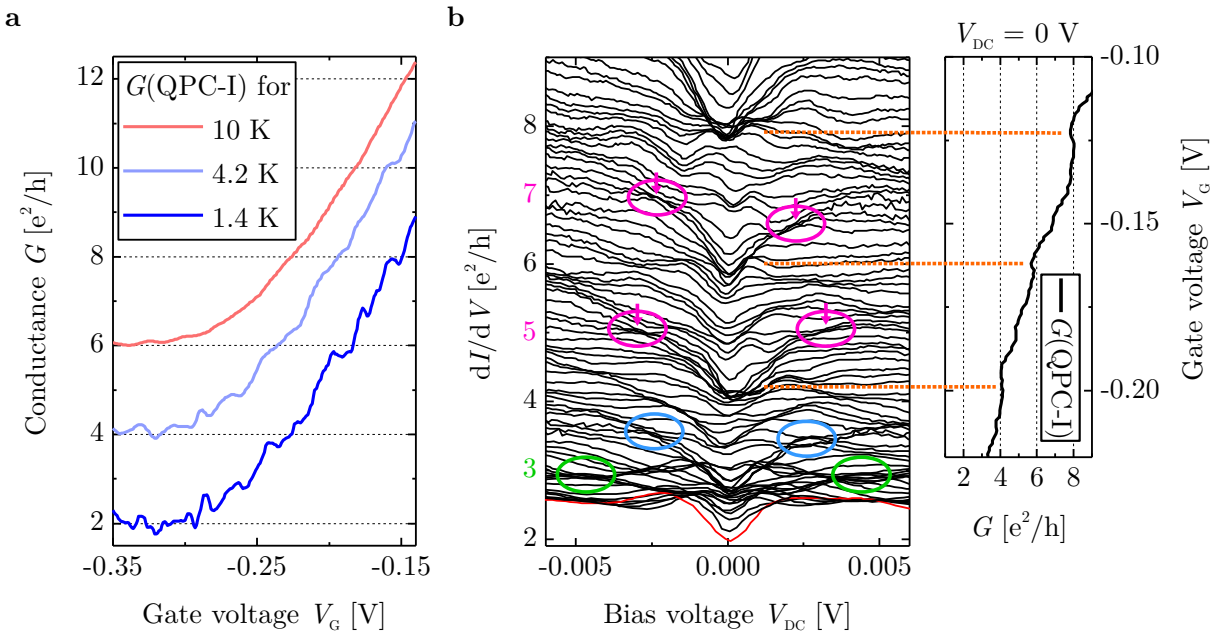

Figure 2.14: **a**, Gate voltage V_G dependence of the conductance G of QPC-I for different values of the temperature. The curves are vertically offset for clarity by $\Delta G = 2e^2/h$. **b**, Bias voltage V_DC dependence of the differential conductance $\mathrm{d}I/\mathrm{d}V$ of QPC-I for different values of the gate voltage. The pink circles highlight plateaus at odd integer values of e^2/h for $\mathrm{d}I/\mathrm{d}V > 4e^2/h$, while the blue and green circles indicate plateau-like features within the sub-open regime. The arrows point at the read out values of the bias voltage. The accumulation around the red trace is attributed to modes with predominant QSH character. The data of panel **a** and **b** was acquired performing another measurement in addition to the data shown in Fig. 2.11. The shift of the (differential) conductance traces with regard to the applied gate voltage between the measurements is due to thermal cycling.

gate voltage influence around $G \approx 0.7 \cdot 2e^2/h$, which is mostly signified as 0.7 anomaly and usually attributed to electron-electron-interaction effects [55–58] (see also Section 4.2.2). In Fig. 2.14b, the blue circles highlight the formation of plateau-like shapes within the sub-open regime of QPC-I around $\mathrm{d}I/\mathrm{d}V \approx 3.5e^2/h$. For the case of a topological QPC, features related to the 0.7 anomaly are expected to appear at a value of $\mathrm{d}I/\mathrm{d}V = (1+0.7) \cdot 2e^2/h = 3.4e^2/h$. Hence, the observed plateaus around $\mathrm{d}I/\mathrm{d}V \approx 3.5e^2/h$ are attributed to the emergence of the 0.7 anomaly.

Moreover, the bias voltage dependence of the differential conductance of QPC-I reveals another feature at $\mathrm{d}I/\mathrm{d}V \approx (1+0.5) \cdot 2e^2/h = 3e^2/h$, which is indicated by the green circles in Fig. 2.14b. The latter corresponds to a situation in which the Fermi level of one reservoir lies above the first subband, while the other reservoir lies within the pinch-off regime of the trivial 1D conductance contribution [56]. The fact that it is possible to detect these signatures in topological QPC devices – shifted by $\Delta\mathrm{d}I/\mathrm{d}V \approx 2e^2/h$, but otherwise equivalent to trivial QPC samples – provides explicit proof of the unperturbed coexistence of helical and trivial transport modes. The red trace in Fig. 2.14b highlights the transition from the lower end of the sub-open regime to the QSH regime. The discussion of the latter under temperature and bias voltage influence is not part of this thesis.

2.5 Conclusion

The implementation of a working QPC technology in a QSH system represents a trailblazing development in the field of 2D-TIs and allows for a multitude of future experiments. Proposed applications of high interest facilitated by this technological breakthrough are for example spin-controllable devices [59, 60] or the examination of parafermions [61]. A further experiment of high significance is enabled by the opening of helical gaps in narrow topological QPC devices, since such samples are envisaged to act as an essential building block in the context of detecting Majorana Kramers pairs [62]. Furthermore, the all-electrically controllable conductance range of $G \geq 0$ suggests the usage of narrow QPC devices as barriers of variable resistance in topological samples. Hence, such narrow QPCs can be integrated in various setups, for example in the context of zero-bias tunnelling spectroscopy experiments [63].

2.6 Sample overview

QPC No.	d_{QW} [nm]	W_{QPC} [nm]	L_{QPC} [nm]	L_{Gate} [nm]	$n_{\mathrm{e}}(0\,\mathrm{V})$ [cm^{-2}]	$\mu_{\mathrm{e}}(0\,\mathrm{V})$ [$\mathrm{cm}^2\mathrm{V}^{-1}\mathrm{s}^{-1}$]	l_{e} [µm]	Layer thicknesses [nm]
I	7.0	100	500	250	$5.2 \cdot 10^{11}$	$2.7 \cdot 10^5$	3.2	70/9/70/7/50
II	5.5	100	500	250	$5.1 \cdot 10^{11}$	$1.5 \cdot 10^5$	1.8	71/10/71/5.5/51
III	7.0	150	500	250	$5.2 \cdot 10^{11}$	$2.7 \cdot 10^5$	3.2	70/9/70/7/50
IV	7.0	200	500	250	$5.2 \cdot 10^{11}$	$2.7 \cdot 10^5$	3.2	70/9/70/7/50
V	7.0	250	500	250	$4.8 \cdot 10^{11}$	$2.3 \cdot 10^5$	2.6	81/10/81/7/59
VI	7.0	50	500	250	$5.2 \cdot 10^{11}$	$2.7 \cdot 10^5$	3.2	70/9/70/7/50

Table 2.1: Summary of the sample and material parameters for each discussed QPC device indicated by Roman numerals. The layer thickness values refer to the sketched layer stack shown in Fig. 2.7b. The given numbers (from right to left) are attributed to the sketched layers from top to bottom. The thickness of the buffer as well as of the substrate is not included.

Bibliography

[1] K. v. Klitzing, G. Dorda, and M. Pepper, *New Method for High-Accuracy Determination of the Fine-Structure Constant Based on Quantized Hall Resistance,* Physical Review Letters **45**, 494 (1980).

[2] R. B. Laughlin, *Quantized Hall conductivity in two dimensions,* Physical Review B **23**, 5632 (1981).

[3] D. J. Thouless, M. Kohmoto, M. P. Nightingale, and M. den Nijs, *Quantized Hall Conductance in a Two-Dimensional Periodic Potential,* Physical Review Letters **49**, 405 (1982).

[4] C. L. Kane and E. J. Mele, *Quantum Spin Hall Effect in Graphene,* Physical Review Letters **95**, 226801 (2005).

[5] C. Wu, B. A. Bernevig, and S.-C. Zhang, *Helical Liquid and the Edge of Quantum Spin Hall Systems,* Physical Review Letters **96**, 106401 (2006).

[6] H. Min, J. E. Hill, N. A. Sinitsyn, B. R. Sahu, L. Kleinman, and A. H. MacDonald, *Intrinsic and Rashba spin-orbit interactions in graphene sheets,* Physical Review B **74**, 165310 (2006).

[7] Y. Yao, F. Ye, X.-L. Qi, S.-C. Zhang, and Z. Fang, *Spin-orbit gap of graphene: First-principles calculations,* Physical Review B **75**, 041401 (2007).

[8] B. A. Bernevig, T. L. Hughes, and S.-C. Zhang, *Quantum Spin Hall Effect and Topological Phase Transition in HgTe Quantum Wells,* Science **314**, 1757 (2006).

[9] C. Kane, *Chapter 1 – Topological Band Theory and the Z_2 Invariant,* in *Topological Insulators*, Contemporary Concepts of Condensed Matter Science, Vol. 6 (Elsevier, Amsterdam, 2013).

[10] C. Brüne, H. Buhmann, and L. Molenkamp, *Chapter 5 – Quantum Spin Hall State in HgTe,* in *Topological Insulators*, Contemporary Concepts of Condensed Matter Science, Vol. 6 (Elsevier, Amsterdam, 2013).

[11] J. Chu and A. Sher, *Physics and properties of narrow gap semiconductors* (Springer, New York, 2008).

[12] J. Wiedenmann, *Induced topological superconductivity in HgTe based nanostructures*, Ph.D. thesis, Julius-Maximilians-Universität Würzburg (2018).

[13] C. Brüne, C. X. Liu, E. G. Novik, E. M. Hankiewicz, H. Buhmann, Y. L. Chen, X. L. Qi, Z. X. Shen, S. C. Zhang, and L. W. Molenkamp, *Quantum Hall Effect from the Topological Surface States of Strained Bulk HgTe,* Physical Review Letters **106**, 126803 (2011).

[14] P. Leubner, *Strain-engineering of the Topological Insulator HgTe*, Ph.D. thesis, Julius-Maximilians-Universität Würzburg (2017).

[15] A. Pfeuffer-Jeschke, *Bandstruktur und Landau-Niveaus quecksilberhaltiger II-VI-Heterostrukturen*, Ph.D. thesis, Julius-Maximilians-Universität Würzburg (2000).

[16] B. Büttner, C. X. Liu, G. Tkachov, E. G. Novik, C. Brüne, H. Buhmann, E. M. Hankiewicz, P. Recher, B. Trauzettel, S. C. Zhang, and L. W. Molenkamp, *Single valley Dirac fermions in zero-gap HgTe quantum wells,* Nature Physics **7**, 418 (2011).

[17] B. Büttner, *Micromagnetic Sensors and Dirac Fermions in HgTe Heterostructures*, Ph.D. thesis, Julius-Maximilians-Universität Würzburg (2012).

[18] M. König, *Spin-related transport phenomena in HgTe-based quantum well structures*, Ph.D. thesis, Julius-Maximilians-Universität Würzburg (2007).

[19] S.-Q. Shen, *Topological Insulators* (Springer, Berlin, 2012).

[20] M. König, S. Wiedmann, C. Brüne, A. Roth, H. Buhmann, L. W. Molenkamp, X. L. Qi, and S.-C. Zhang, *Quantum Spin Hall Insulator State in HgTe Quantum Wells,* Science **318**, 766 (2007).

[21] A. Roth, C. Brüne, H. Buhmann, L. W. Molenkamp, J. Maciejko, X. L. Qi, and S.-C. Zhang, *Nonlocal Transport in the Quantum Spin Hall State,* Science **325**, 294 (2009).

[22] C. Brüne, A. Roth, H. Buhmann, E. M. Hankiewicz, L. W. Molenkamp, J. Maciejko, X. L. Qi, and S.-C. Zhang, *Spin polarization of the quantum spin Hall edge states,* Nature Physics **8**, 486 (2012).

[23] C. W. J. Beenakker and H. V. Houten, *Quantum Transport in Semiconductor Nanostructures,* Solid State Physics **44**, 1 (1991).

[24] H. van Houten, C. Beenakker, and B. van Wees, *Chapter 2 – Quantum Point Contacts,* in *Nanostructured Systems*, Semiconductors and Semimetals, Vol. 35 (Elsevier, Amsterdam, 1992).

[25] T. Ihn, *Semiconductor Nanostructures: Quantum States and Electronic Transport* (Oxford University Press, Oxford, 2010).

[26] B. J. van Wees, H. van Houten, C. W. J. Beenakker, J. G. Williamson, L. P. Kouwenhoven, D. van der Marel, and C. T. Foxon, *Quantized conductance of point contacts in a two-dimensional electron gas,* Physical Review Letters **60**, 848 (1988).

[27] D. A. Wharam, T. J. Thornton, R. Newbury, M. Pepper, H. Ahmed, J. E. F. Frost, D. G. Hasko, D. C. Peacock, D. A. Ritchie, and G. A. C. Jones, *One-dimensional transport and the quantisation of the ballistic resistance,* Journal of Physics C: Solid State Physics **21**, L209 (1988).

[28] M. Büttiker, *Quantized transmission of a saddle-point constriction,* Physical Review B **41**, 7906 (1990).

[29] J. Heyder, *The 0.7 anomaly in quantum point contacts: a microscopic model for the first conductance step*, Ph.D. thesis, Ludwig–Maximilians–Universität München (2014).

[30] S. Datta, *Electronic transport in mesoscopic systems* (Cambridge university press, Cambridge, 1995).

[31] B. Brun, *Electron interactions in mesoscopic physics: scanning gate microscopy and interferometry at a quantum point contact*, Ph.D. thesis, Université de Grenoble (2014).

[32] R. Landauer, *Spatial Variation of Currents and Fields Due to Localized Scatterers in Metallic Conduction,* IBM Journal of Research and Development **1**, 223 (1957).

[33] L. I. Glazman, G. B. Lesovik, D. E. Khmelnitskii, and R. I. Shekhter, *Reflectionless quantum transport and fundamental ballistic-resistance steps in microscopic constrictions,* JETP Letters **48**, 238 (1988).

[34] A. Yacoby and Y. Imry, *Quantization of the conductance of ballistic point contacts beyond the adiabatic approximation,* Physical Review B **41**, 5341 (1990).

[35] A. Szafer and A. D. Stone, *Theory of quantum conduction through a constriction,* Physical Review Letters **62**, 300 (1989).

[36] N. Tombros, A. Veligura, J. Junesch, M. H. D. Guimarães, I. J. Vera-Marun, H. T. Jonkman, and B. J. van Wees, *Quantized conductance of a suspended graphene nanoconstriction,* Nature Physics **7**, 697 (2011).

[37] H. Overweg, A. Knothe, T. Fabian, L. Linhart, P. Rickhaus, L. Wernli, K. Watanabe, T. Taniguchi, D. Sánchez, J. Burgdörfer, F. Libisch, V. I. Fal'ko, K. Ensslin, and T. Ihn, *Topologically Nontrivial Valley States in Bilayer Graphene Quantum Point Contacts,* Physical Review Letters **121**, 257702 (2018).

[38] H. Hou, Y. Kozuka, J.-W. Liao, L. W. Smith, D. Kos, J. P. Griffiths, J. Falson, A. Tsukazaki, M. Kawasaki, and C. J. B. Ford, *Quantized conductance of one-dimensional strongly correlated electrons in an oxide heterostructure,* Physical Review B **99**, 121302 (2019).

[39] A. Jouan, G. Singh, E. Lesne, D. C. Vaz, M. Bibes, A. Barthélémy, C. Ulysse, D. Stornaiuolo, M. Salluzzo, S. Hurand, J. Lesueur, C. Feuillet-Palma, and N. Bergeal, *Quantized conductance in a one-dimensional ballistic oxide nanodevice,* Nature Electronics **3**, 201 (2020).

[40] M. J. Mühlbauer, *Nanolithography on Mercury Telluride*, Ph.D. thesis, Julius-Maximilians-Universität Würzburg (2015).

[41] K. Bendias, S. Shamim, O. Herrmann, A. Budewitz, P. Shekhar, P. Leubner, J. Kleinlein, E. Bocquillon, H. Buhmann, and L. W. Molenkamp, *High Mobility HgTe Microstructures for Quantum Spin Hall Studies,* Nano Letters **18**, 4831 (2018).

[42] M. K. Bendias, *Quantum Spin Hall Effect – A new generation of microstructures*, Ph.D. thesis, Julius-Maximilians-Universität Würzburg (2018).

[43] P. Debray, S. M. S. Rahman, J. Wan, R. S. Newrock, M. Cahay, A. T. Ngo, S. E. Ulloa, S. T. Herbert, M. Muhammad, and M. Johnson, *All-electric quantum point contact spin-polarizer,* Nature Nanotechnology **4**, 759 (2009).

[44] D. Nanclares, L. R. F. Lima, C. H. Lewenkopf, and L. G. G. V. D. da Silva, *Tunable spin-polarized edge transport in inverted quantum-well junctions,* Physical Review B **96**, 155302 (2017).

[45] J. A. Nixon, J. H. Davies, and H. U. Baranger, *Breakdown of quantized conductance in point contacts calculated using realistic potentials,* Physical Review B **43**, 12638 (1991).

[46] M. Papaj, L. Cywiński, J. Wróbel, and T. Dietl, *Conductance oscillations in quantum point contacts of InAs/GaSb heterostructures,* Physical Review B **93**, 195305 (2016).

[47] S. Hart, H. Ren, T. Wagner, P. Leubner, M. Mühlbauer, C. Brüne, H. Buhmann, L. W. Molenkamp, and A. Yacoby, *Induced superconductivity in the quantum spin Hall edge,* Nature Physics **10**, 638 (2014).

[48] E. Y. Ma, M. R. Calvo, J. Wang, B. Lian, M. Mühlbauer, C. Brüne, Y.-T. Cui, K. Lai, W. Kundhikanjana, Y. Yang, M. Baenninger, M. König, C. Ames, H. Buhmann, P. Leubner, L. W. Molenkamp, S.-C. Zhang, D. Goldhaber-Gordon, M. A. Kelly, and Z.-X. Shen, *Unexpected edge conduction in mercury telluride quantum wells under broken time-reversal symmetry,* Nature Communications **6**, 7252 (2015).

[49] K. C. Nowack, E. M. Spanton, M. Baenninger, M. König, J. R. Kirtley, B. Kalisky, C. Ames, P. Leubner, C. Brüne, H. Buhmann, L. W. Molenkamp, D. Goldhaber-Gordon, and K. A. Moler, *Imaging currents in HgTe quantum wells in the quantum spin Hall regime,* Nature Materials **12**, 787 (2013).

[50] M. König, M. Baenninger, A. G. F. Garcia, N. Harjee, B. L. Pruitt, C. Ames, P. Leubner, C. Brüne, H. Buhmann, L. W. Molenkamp, and D. Goldhaber-Gordon, *Spatially Resolved Study of Backscattering in the Quantum Spin Hall State,* Physical Review X **3**, 021003 (2013).

[51] N. K. Patel, L. Martin-Moreno, M. Pepper, R. Newbury, J. E. F. Frost, D. A. Ritchie, G. A. C. Jones, J. T. M. B. Janssen, J. Singleton, and J. A. A. J. Perenboom, *Ballistic transport in one dimension: additional quantisation produced by an electric field,* Journal of Physics: Condensed Matter **2**, 7247 (1990).

[52] N. K. Patel, J. T. Nicholls, L. Martin-Moreno, M. Pepper, J. E. F. Frost, D. A. Ritchie, and G. A. C. Jones, *Evolution of half plateaus as a function of electric field in a ballistic quasi-one-dimensional constriction,* Physical Review B **44**, 13549 (1991).

[53] L. Martin-Moreno, J. T. Nicholls, N. K. Patel, and M. Pepper, *Non-linear conductance of a saddle-point constriction,* Journal of Physics: Condensed Matter **4**, 1323 (1992).

[54] B. J. van Wees, L. P. Kouwenhoven, E. M. M. Willems, C. J. P. M. Harmans, J. E. Mooij, H. van Houten, C. W. J. Beenakker, J. G. Williamson, and C. T. Foxon, *Quantum ballistic and adiabatic electron transport studied with quantum point contacts,* Physical Review B **43**, 12431 (1991).

[55] K. J. Thomas, J. T. Nicholls, M. Y. Simmons, M. Pepper, D. R. Mace, and D. A. Ritchie, *Possible Spin Polarization in a One-Dimensional Electron Gas,* Physical Review Letters **77**, 135 (1996).

[56] A. Kristensen, H. Bruus, A. E. Hansen, J. B. Jensen, P. E. Lindelof, C. J. Marckmann, J. Nygård, C. B. Sørensen, F. Beuscher, A. Forchel, and M. Michel, *Bias and temperature dependence of the 0.7 conductance anomaly in quantum point contacts,* Physical Review B **62**, 10950 (2000).

[57] C. Sloggett, A. I. Milstein, and O. P. Sushkov, *Correlated electron current and temperature dependence of the conductance of a quantum point contact,* The European Physical Journal B **61**, 427 (2008).

[58] F. Bauer, J. Heyder, E. Schubert, D. Borowsky, D. Taubert, B. Bruognolo, D. Schuh, W. Wegscheider, J. V. Delft, and S. Ludwig, *Microscopic origin of the '0.7-anomaly' in quantum point contacts,* Nature **501**, 73 (2013).

[59] F. Dolcini, *Full electrical control of charge and spin conductance through interferometry of edge states in topological insulators,* Physical Review B **83**, 165304 (2011).

[60] V. Krueckl and K. Richter, *Switching Spin and Charge between Edge States in Topological Insulator Constrictions,* Physical Review Letters **107**, 086803 (2011).

[61] C. Fleckenstein, N. T. Ziani, and B. Trauzettel, *$\mathbb{Z}_4$ parafermions in Weakly Interacting Superconducting Constrictions at the Helical Edge of Quantum Spin Hall Insulators,* Physical Review Letters **122**, 066801 (2019).

[62] J. Li, W. Pan, B. A. Bernevig, and R. M. Lutchyn, *Detection of Majorana Kramers Pairs Using a Quantum Point Contact,* Physical Review Letters **117**, 046804 (2016).

[63] H. O. H. Churchill, V. Fatemi, K. Grove-Rasmussen, M. T. Deng, P. Caroff, H. Q. Xu, and C. M. Marcus, *Superconductor-nanowire devices from tunneling to the multichannel regime:*

Zero-bias oscillations and magnetoconductance crossover, Physical Review B **87**, 241401 (2013).

3

Quantum spin Hall interferometer state in HgTe based quantum point contacts

In this chapter, the occurrence of quantum interference effects in the quantum spin Hall regime of narrow quantum point contact devices fabricated from HgTe quantum wells with a thickness of $d_{\mathrm{QW}} = 7\,\mathrm{nm}$ *is discussed. The associated emergence of an interferometer state is explained utilizing a model based on band structure calculations and the relevant quantum phases are introduced – the Aharonov-Bohm phase, the dynamical Aharonov-Casher phase and the spin-orbit Berry phase. Subsequently, measurements of the magnetoconductance within the quantum spin Hall regime of an exemplary device are presented. The data exhibits Aharonov-Bohm characteristic oscillations and the corresponding period is in quantitative agreement with the device dimensions. These observations are accompanied by a periodic modulation of the gate voltage dependence of the conductance in the quantum spin Hall regime as well as by an inversion of the afore mentioned magnetoconductance pattern for different values of the gate voltage, which provides evidence for the impact of the dynamical Aharonov-Casher phase. Moreover, a phase shift within the first Aharonov-Bohm period is reported, which is attributed to the accumulation of a spin-orbit Berry phase of* π*. To illustrate the interplay of all three quantum phases, the obtained data is compared with analytic model considerations. Afterwards, an experimental sanity check of the proposed ring formation model is provided. Lastly, the data of two more devices is presented, reproducing all key effects.*

3.1 Emergence of a quantum spin Hall interferometer state

The comparability between the width of a QPC device and the Fermi wavelength of the underlying 2D system is of fundamental importance for trivial ballistic 1D (and thus quantized) transport to occur within the n-n'-n regime. However, for the case of 2D-TIs, it furthermore enables the observability of a physical phenomenon which has so far been a topic of merely theoretical considerations – the emergence of quantum interference effects within the QSH regime. In theoretical publications, it is an established method to propose QSH interferometers based on two neighbouring point-like QPCs [1–3]. In these scenarios, the QPCs act as two consecutive inter-edge couplers between the helical edge states, thus enabling the formation of a closed QSH ring. While these suggestions still lack experimental examination, the subsequent explications are going to show that – under certain conditions – already a single HgTe based QPC device with finite dimensions (not point-like) is sufficient to provide the experimental framework for a QSH interferometer.

3.1.1 Interference in quantum mechanical systems

The occurrence of interference effects within the scope of quantum transport experiments is related to the wave-particle duality of matter – a cornerstone of quantum mechanics. In this regard, the quantum mechanical behaviour of electrons is no different than for example the one of neutrons or even molecules [4]. In an experimental context, the archetypal approach to discuss interference and the wave-particle duality of matter is the double slit experiment.

There, a wave of light or matter is diffracted by two slits with a width smaller than the associated wavelength and an interference pattern emerges on an observation screen placed further behind. The complex-valued probability amplitude t for transmission through the upper split is described by $t_1 = a_1 \mathrm{e}^{\mathrm{i}\theta_1}$, whereas $t_2 = a_2 \mathrm{e}^{\mathrm{i}\theta_2}$ captures the transmission through the lower slit. In both cases, a_1 and a_2 represent positive real numbers between 0 and 1 and θ_1 as well as θ_2 are real-valued transmission phases. The intensity on the observation screen is then given by

$$\mathcal{T} = |t_1 + t_2|^2 = a_1^2 + a_2^2 + 2a_1 a_2 \cos\delta \,, \tag{3.1}$$

where $\delta = \theta_1 - \theta_2$ describes the phase difference. The first two terms $a_1^2 + a_2^2$ on the right hand side of the above equation represent the classical transmission probability, i.e. the sum of the two individual transmission probabilities. The third term $2a_1 a_2 \cos\delta$ captures the impact of quantum interference [5]. For an introduction to the topic, the interested reader is referred to Ref. [6].

A generalized form of the double slit experiment setup is represented by a two-path interferometer. The latter is sketched in Fig. 3.1 and is applicable to a lot of experiments examining interference effects. Particles entering the interferometer loop are split into two partial waves by a beam splitter and traverse the ring geometry half clockwise and half counterclockwise in the upper and lower interferometer arm, respectively. They interfere in the exit region (beam

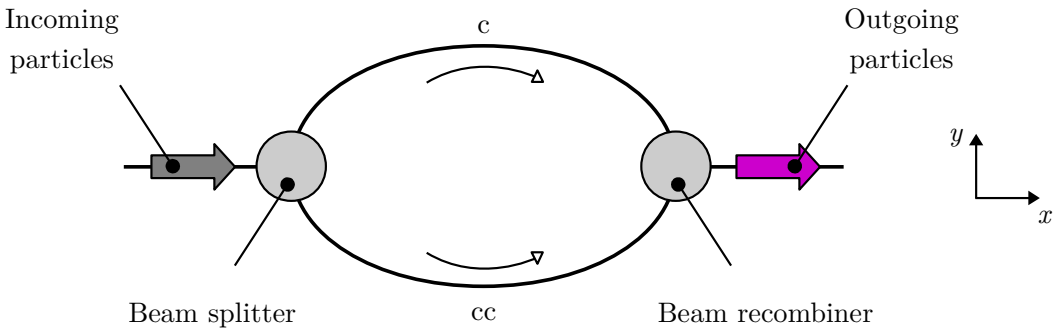

Figure 3.1: Sketch of a two-path interferometer. The incoming particles are split into two partial waves by a beam splitter at the entrance of the ring and traverse the ring half clockwise (c) and half counterclockwise (cc), respectively. They interfere in the exit region (beam recombiner) and subsequently leave the interferometer. Path geometries with higher winding numbers and the occurrence of reflections are neglected.

recombiner) and subsequently leave the interferometer [7]. For analysing interference effects in semiconductor nanostructures, the ring geometry has to be defined electrostatically by using gate electrodes [8] or physically by etching mesa structures [9]. Moreover, interference patterns are detected by using contacts instead of an interference screen.

3.1.2 Formation of a quantum spin Hall ring

In order to form a QSH interferometer, it is necessary to realize a closed ring geometry purely based on helical edge channels. Furthermore, the transport through both interferometer arms has to be phase-coherent and equally probable. Thus, for a single QPC device, a transport situation is required in which reservoir electrons with randomized spin couple to both helical edge channels with the same probability. A narrow QPC device based on a HgTe quantum well with a thickness of $d_{\mathrm{QW}} = 7\,\mathrm{nm}$ provides an unpretentious realization of such a transport regime.

To understand how an interferometer state forms within the QSH regime of such a device, the corresponding band structure shown in Fig. 3.2a has to be analysed. It is calculated for a semi-finite ribbon with $W_{\mathrm{y}} = 100\,\mathrm{nm}$ and $d_{\mathrm{QW}} = 7\,\mathrm{nm}$ using $\mathbf{k} \cdot \mathbf{p}$ theory, which is based on the eight-band Kane model [10]. The colour code indicates the spatial extension of the wave function in the y direction expressed by the associated standard deviation σ_{y}. It can be observed that the spatial extension of the QSH edge channels strongly depends on the position of the Fermi energy. The largest spatial extension in y direction arises when the Fermi energy is located in the vicinity of the Dirac point (regime II in Fig. 3.2a), while the QSH edge channels become more localized at the device edges when the Fermi energy is approaching the n- or p-conducting regime (regime I and III). It should be noted that the calculation neglects any temperature effect ($T = 0\,\mathrm{K}$) and thus exhibits a finite gap of $\Delta E \approx 3.5\,\mathrm{meV}$ around the Dirac point due to hybridization.

A QSH ring structure emerges when the wave function of the average incident electrons overlaps with both helical edge channels simultaneously, i.e. when incident electrons from the reservoir have equal probability to enter either of the two QSH edge channels (see Fig. 3.2c). This situation is realized when the width of the constriction W_{QPC}, the Fermi wavelength λ_{F} of

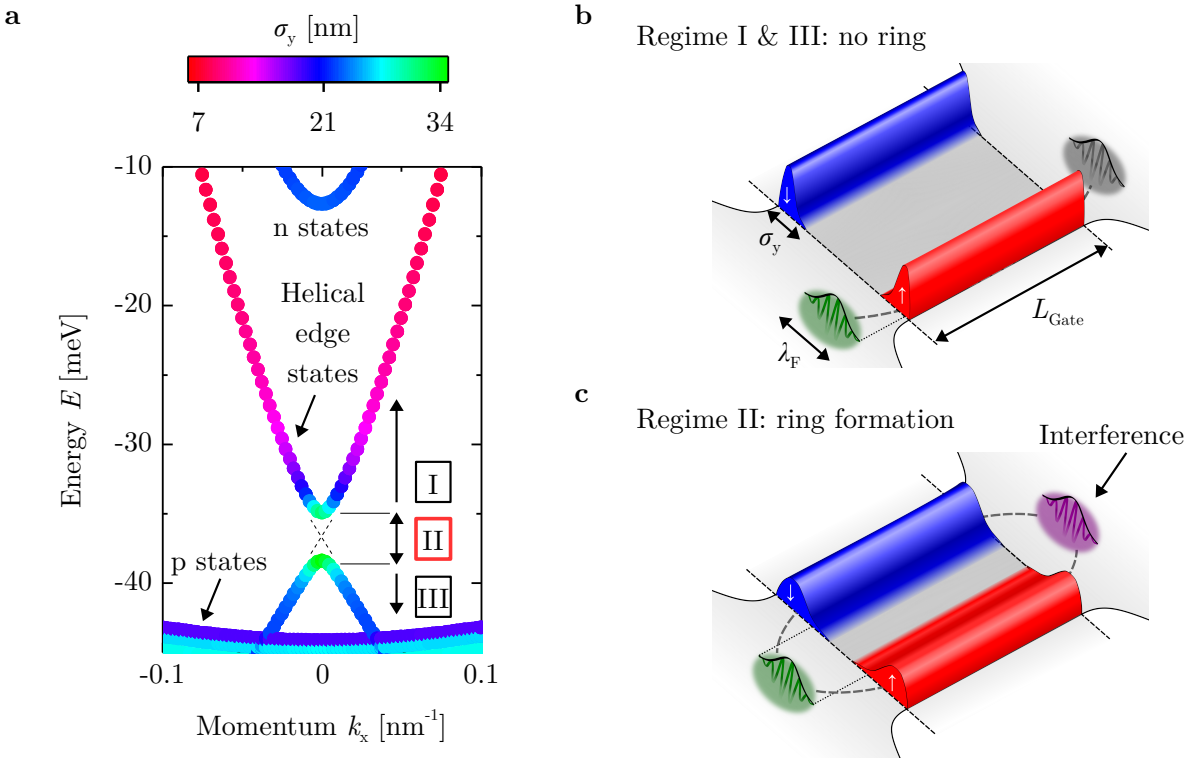

Figure 3.2: **a**, $\mathbf{k}\cdot\mathbf{p}$ band structure calculation for a semi-finite ribbon with $W_y = 100\,\text{nm}$ and $d_{QW} = 7\,\text{nm}$. The colour code indicates the standard deviation σ_y of the wave function in y direction, which is categorized by three regimes. **b**, **c**, Emergence of a QSH interferometer within regime II, when the condition defined by Eq. 3.2 is met.

the incident electrons and the spatial extension of the helical edge states σ_y meet the condition

$$2\sigma_y + \lambda_F \gtrapprox W_{QPC}\,. \tag{3.2}$$

Furthermore, both possible propagation paths are externally indistinguishable within the utilized device concept, thus enabling the occurrence of interference effects when transmitted electrons are leaving the QSH ring [6, 8].

For being able to apply Eq. 3.2 to the case of a QPC device with a width of $W_{QPC} \approx 100\,\text{nm}$ based on a HgTe quantum well with $d_{QW} = 7\,\text{nm}$, a quantification of the Fermi wavelength λ_F of the incident electrons is necessary. The latter corresponds to the *de Broglie wavelength* of electrons at the Fermi energy and can be calculated using

$$\lambda_F = \frac{h}{p_F} = \frac{h}{m^* v_F} = \frac{h}{\hbar k_F} = \frac{2\pi}{\sqrt{(4\pi n_e)/(g_s g_v)}} = \sqrt{\frac{2\pi}{n_e}}\,, \tag{3.3}$$

where $v_F = \hbar k_F / m^*$ represents the Fermi velocity for the case of a 2DEG (k_F is the Fermi wave vector). By utilizing the electron density of the equilibrium reservoirs obtained from reference Hall bar measurements (see Tab. 3.1), Eq. 3.3 yields a value of $\lambda_F \approx 35\,\text{nm}$ for the case of QPC-I. Thus, the condition of Eq. 3.2 is met for regime II, where $\sigma_y > 30\,\text{nm}$. Hence, the formation of

a QSH ring within a QPC device of appropriate width depends on the position of the Fermi energy. As a consequence, the QSH interferometer state can be switched on and off depending on the localization length of the QSH edge channels and therefore by the applied gate voltage (see Fig. 3.2b,c).

3.2 Relevant quantum phases

The formation of a QSH interferometer enables various novel experiments based on the accumulation of different quantum phases. In order to identify relevant quantum phases contributing to interference effects in the above outlined scenario, it is helpful to recapitulate the fundamental transport situation:

- QSH edge channels carry spin-polarized electrons;
- HgTe quantum wells exhibit strong Rashba spin-orbit coupling [11, 12].

Taking these considerations into account, three quantum phase contributions are expected to be detectable analysing narrow QPC devices based on HgTe quantum wells with $d_{\mathrm{QW}} = 7\,\mathrm{nm}$ [13].

3.2.1 Aharonov-Bohm phase

In 1959, *Aharonov and Bohm* [14] predicted the occurrence of a phase shift between two interfering partial waves of a charged particle, when their afore taken paths (defined by γ_1 and γ_2) have enclosed a magnetic flux ϕ (see Fig. 3.3 for a sketch). The latter can be described by a vector potential $\mathbf{A}(\mathbf{r})$. The presence of the magnetic flux modifies the transmission phases according to

$$\theta_i(\phi) = \theta_i(0) - \frac{|e|}{\hbar}\int_{\gamma_i} \mathbf{A} d\mathbf{s}\,. \tag{3.4}$$

Consequently, the phase difference between the partial waves

$$\delta(\phi) = \delta(0) - \frac{|e|}{\hbar}\int_{\gamma_1-\gamma_2} \mathbf{A} d\mathbf{s} = \delta(0) - 2\pi\frac{\phi}{\phi_0} \tag{3.5}$$

depends on the magnetic flux ϕ with $\phi_0 = h/|e|$ representing the magnetic flux quantum. Thus, the flux-dependent transmission term

$$\mathcal{T}(\phi) = a_1^2 + a_2^2 + 2a_1a_2\cos\left[\delta(0) - 2\pi\frac{\phi}{\phi_0}\right] \tag{3.6}$$

can be identified. Due to the property

$$\mathcal{T}(\phi + n\cdot\phi_0) = \mathcal{T}(\phi)\,, n \in \mathbb{Z}\,, \tag{3.7}$$

it is possible to detect a periodic interference pattern by tuning the magnetic flux ϕ. The phase factor appearing within Eq. 3.6 in addition to the zero magnetic flux case is referred to as the

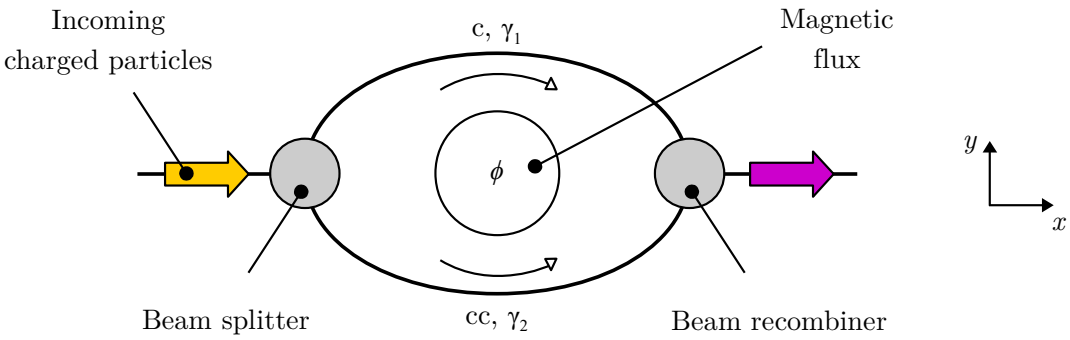

Figure 3.3: Sketch of the acquisition of an AB phase. Partial waves descending from incoming charged particles (for example electrons) encircle a magnetic flux tube enclosing the flux ϕ. The acquisition of the AB phase induces a modulation of the magnetoconductance of the ring structure.

Aharonov-Bohm (AB) phase, which is described by

$$\varphi_{\mathrm{AB}} = -2\pi \frac{\phi}{\phi_0} \,. \tag{3.8}$$

It should be noted that the above considerations are rather generic geometry-wise. For the specific case of partial waves descended from an electron propagating on a circular path around a magnetic flux, the probability to be transmitted through the ring within half a revolution is given by

$$\mathcal{T} = \frac{1}{2}\left[1 + \cos\left(2\pi \frac{\phi}{\phi_0}\right)\right] . \tag{3.9}$$

Considering a 1D transport regime (at zero temperature and neglecting any reflection processes), the corresponding conductance is described by

$$G = G_0 \cdot \mathcal{T} = \frac{e^2}{h}\left[1 + \cos\left(2\pi \frac{\phi}{\phi_0}\right)\right] . \tag{3.10}$$

The magnetic flux threaded through the encircled area A is quantified by

$$\phi = B_{\mathrm{z}} \cdot A \,, \tag{3.11}$$

where B_{z} is the magnetic field applied perpendicular to the ring plane. Thus, the period ΔB_{z} of the oscillating magnetoconductance

$$\Delta B_{\mathrm{z}} = \frac{h/|e|}{A} =: \rho_{\mathrm{AB}} \tag{3.12}$$

is indirectly proportional to the encircled ring area A [5]. The AB effect was experimentally demonstrated for the first time in 1985 by analysing a single metal ring [15]. The detection of the AB effect in ring structures fabricated from semiconductor heterostructures followed shortly after [16–18].

3.2.2 Dynamical Aharonov-Casher phase

In 1984, *Aharonov and Casher* [19] elaborated that an electromagnetic dual to the AB effect exists. It becomes manifest when a neutral particle equipped with a magnetic moment (spin) encircles a charge density λ, which creates a radial electric field. With relativistically transforming the electric field $\mathbf{E}$ into the moving reference frame of the uncharged particle, it becomes obvious that the magnetic moment experiences the magnetic field $\mathbf{B} = c^{-2}\mathbf{v} \times \mathbf{E}$, where c represents the speed of light and $\mathbf{v}$ the electron velocity. Thus, the orientation of the magnetic moment changes due to the influence of this very magnetic field and the induced circular motion of the magnetic moment then leads to the accumulation of another quantum phase – the so-called Aharonov-Casher (AC) phase [5]. This situation is sketched in Fig. 3.4.

It has to be emphasized that the original conception of the AC effect is hardly realizable in semiconductor nanostructures, since electrons and holes are charged particles. However, the scientific community extended the notion of the AC effect to scenarios in which charged particles with spin are moving in arbitrarily oriented electric fields within solids [20–22]. Thus, such a situation is equivalent to the presence of Rashba spin-orbit coupling in semiconductors [5].

In a quantum ring subject to Rashba spin-orbit coupling, time evolution leads to a precession of spins [23]. In the adiabatic regime, the precession axis of the spin eigenstates aligns itself with the direction of an effective magnetic field (see Fig. 3.5b). Since the precession direction of the spin depends on the propagation path γ_i, the two interfering partial waves sketched in Fig. 3.4 carry a phase difference. Hence, an accumulated phase originating from the propagation path dependent spin precession is called a dynamical phase [20, 23]. Due to the causative physical background, this quantum phase is referred to as dynamical AC phase $\varphi_{\mathrm{AC}}^{\mathrm{Dyn.}}$ [20].

In order to get a grasp on the dynamical AC phase, Ref. [5] considers the circular motion of an electron in the presence of Rashba spin-orbit coupling. In analogy to the AB case, a full analytical treatment of the transmission of two interfering partial waves through a two-terminal ring geometry is provided. The dynamical AC phase is found to be described by [5, 24]

$$\varphi_{\mathrm{AC}}^{\mathrm{Dyn.}} = -\pi\left[1 + s\sqrt{1 + \left(\frac{2rm^*\alpha_{\mathrm{R}}}{\hbar^2}\right)^2}\right], s = \pm 1\,, \tag{3.13}$$

where α_{R} is the Rashba coupling strength, r is the radius of the encircled ring and $s = \pm 1$ represents the two spin eigenstates. The associated conductance modulation of a 1D transport regime is then given by [20, 24]

$$G = \frac{e^2}{h}\left\{1 - \cos\left[\pi\sqrt{1 + \left(\frac{2rm^*\alpha_{\mathrm{R}}}{\hbar^2}\right)^2}\right]\right\}. \tag{3.14}$$

Since the Rashba coupling strength α_{R} is controlled by structural inversion asymmetry, changing the gate voltage V_{G} induces a conductance modulation approximately described by $\Delta G \sim \cos(\alpha_{\mathrm{R}})$

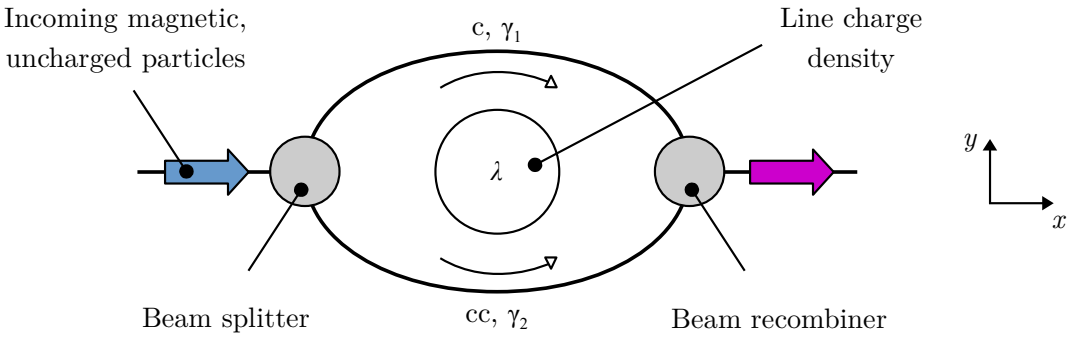

Figure 3.4: Sketch of the acquisition of a dynamical AC phase. Partial waves descending from incoming uncharged particles with a magnetic moment (spin) encircle a tube of constant line charge density λ and thus a radial electric field. In materials with strong Rashba spin-orbit coupling, the acquisition of the dynamical AC phase induces a modulation of the gate voltage dependence of the conductance of the ring structure.

with $\alpha_R \sim V_G$ [20]. It should be noted that the outlined relation between Rashba coupling strength and gate voltage is also valid for the QSH regime [28]. However, in order to accentuate the special nature of the helical spectrum, the Rashba coupling strength within the QSH regime is referred to as ξ_R in the following. After the pioneering work of Ref. [20] concerning the experimental detection of the dynamical AC phase, signatures of the latter have been observed in several experiments [9, 23, 25–27].

3.2.3 Spin-orbit Berry phase

However, the total AC phase φ_{AC}^{Total} accumulated by the spin wave function in quantum rings subject to Rashba spin-orbit coupling does not only consist of the dynamical AC phase component $\varphi_{AC}^{Dyn.}$, but is a sum of a dynamical and a geometric phase factor [29]

$$\varphi_{AC}^{Total} = \varphi_{AC}^{Dyn.} + \varphi_{Geo.}\,. \tag{3.15}$$

Geometric phases are accumulated during the cyclic evolution of a quantum system and solely depend on the geometry of the traversed evolution path. Thus, a geometric phase is not influenced by the dynamics of the underlying system, which makes it robust against dephasing [30, 31]. The special case of adiabatic evolution (parameters within the Hamiltonian are changed slowly) was described by *Berry* [32] in 1984 and the associated acquired quantum phase is referred to as Berry phase. The more general situation for any kind of cyclic evolution, i.e. also covering non-adiabatic evolution, was elaborated by *Aharonov and Anandan* [33] in 1986 and the accumulated phase is referred to as Aharonov-Anandan phase. In both cases, the term cyclic refers to a system which returns to its original state after an evolution [33].

In ring structures, the acquisition of a spin geometric phase arises when the wave function of the electron spin is considered in the presence of a magnetic field and when the electron momentum embeds a closed trajectory in momentum space [34]. It has been predicted that such a phase emerges along with the AB phase if the applied magnetic field does not only exhibit

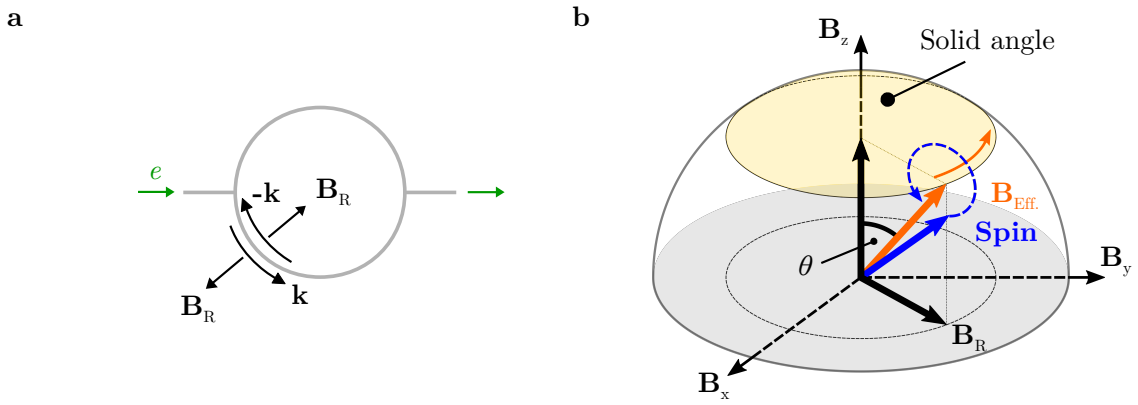

Figure 3.5: **a**, Sketch of a 1D quantum ring subject to Rashba spin-orbit coupling. Electrons transmitted through the ring experience a momentum $\mathbf{k}$ dependent in-plane Rashba field $\mathbf{B}_\mathrm{R}$. **b**, Bloch sphere schematic of the emergence of the dynamical and geometric phase contributions to the total AC phase. A 1D quantum ring subject to an in-plane Rashba field $\mathbf{B}_\mathrm{R}$ and an out-of-plane field $\mathbf{B}_\mathrm{z}$ lies within the x-y-plane. In the adiabatic case, the precession axis of the spin eigenstates aligns itself with the direction of the effective magnetic field $\mathbf{B}_\mathrm{Eff.} = \mathbf{B}_\mathrm{R} + \mathbf{B}_\mathrm{z}$ and the accumulated geometric phase is referred to as spin-orbit Berry phase.

a component normal to the ring plane, but additionally also provides a radial or a tangential component [35–37]. However, since the proposed approaches are relying on textured magnetic fields, they are posing undesired challenges concerning experimental realization.

Instead, a more convenient approach is based on 1D ring structures fabricated from materials exhibiting strong Rashba spin-orbit coupling [34]. Such ring structures host the emergence of the adiabatic regime [21], which entails that the spin precession axis of the propagating electrons aligns itself with the local direction of an emerging, momentum-dependent effective magnetic field $\mathbf{B}_\mathrm{Eff.}$ defined by [21, 34]

$$\mathbf{B}_\mathrm{Eff.} = \mathbf{B}_\mathrm{R} + \mathbf{B}_\mathrm{z}\,, \tag{3.16}$$

where $\mathbf{B}_\mathrm{R}$ describes an in-plane Rashba field (sketched in Fig 3.5a,b). Then, the accumulated spin geometric phase corresponds to a so-called spin-orbit Berry phase [21, 23, 29, 32, 34]

$$\varphi_\mathrm{SB} = \pi[1 - \cos(\theta)]\,, \tag{3.17}$$

which is half the solid angle $\Omega = 2\pi[1 - \cos(\theta)]$ subtended by the effective magnetic field vector. The angle $\theta = \arctan(B_\mathrm{R}/B_\mathrm{z})$ represents the tilt angle between the out-of-plane field component $\mathbf{B}_\mathrm{z}$ and the direction of the effective field $\mathbf{B}_\mathrm{Eff.}$ (see Fig. 3.5b).

For the case of $B_\mathrm{z} = 0\,\mathrm{T}$, Eq. 3.16 yields $\mathbf{B}_\mathrm{Eff.} = \mathbf{B}_\mathrm{R}$, resulting in a tilt angle of $\theta = \pi/2$ and thus a spin-orbit Berry phase of $\varphi_\mathrm{SB} = \pi$. Referring to an interferometer state in narrow HgTe based QPC devices, it should be noted that the associated spin orientation is compatible with QSH edge channels, which exhibit a pronounced in-plane spin component under the influence of Rashba spin-orbit coupling [28, 38, 39]. In such a scenario, the application of a gradually increasing $\mathbf{B}_\mathrm{z}$ vector would then successively decrease the tilt angle θ and hence reduce the accumulated spin-orbit Berry phase.

3.3 Experimental identification of quantum interference effects in the quantum spin Hall regime of device QPC-I

In the following, experimental evidence for the accumulation of an AB phase, of a dynamical AC phase as well as of a spin-orbit Berry phase of π will be presented for the case of QPC-I – thus proving the emergence of a QSH interferometer state. Furthermore, alternative mechanisms hypothetically being able to cause contributions to the observed interference patterns are discussed and subsequently excluded. The observed effects are reproduced by two additional samples, which are discussed in Section 3.5.

3.3.1 Accumulation of an Aharonov-Bohm phase

The magnetoconductance[3] G of QPC-I at $V_\mathrm{G} = -0.261\,\mathrm{V}$ (QSH regime, see Fig. 3.11e) in a field range of $B_\mathrm{z} \in [-1.2; 1.2]\,\mathrm{T}$ is presented in Fig. 3.6a, the corresponding gate voltage V_G dependence of the conductance G is shown in Fig. 3.7a. A modulation with a period of $\rho_\mathrm{AB} \approx 0.172\,\mathrm{T}$ is identifiable, which is indicated by vertical lines in Fig. 3.6a. Inserting $\rho_\mathrm{AB} \approx 0.172\,\mathrm{T}$ into Eq. 3.12 yields an encircled area of $A \approx 24.1 \cdot 10^3\,\mathrm{nm}^2$. This value is consistent with the gated area of QPC-I, which is approximately $A_\mathrm{QPC} = L_\mathrm{Gate} \cdot W_\mathrm{QPC} \approx 250\,\mathrm{nm} \cdot 100\,\mathrm{nm} = 25 \cdot 10^3\,\mathrm{nm}^2$. This conformity quantitatively illustrates the impact of the AB phase and demonstrates electron propagation at the device edges despite spatially extended QSH edge states. Furthermore, the consistency of both values provides an unprecedented experimental proof of the QSH state, since the only possible root cause in the present regime is transport via helical edge channels.

However, within the first AB period ($B_\mathrm{z} = 0\,\mathrm{T} \rightarrow B_\mathrm{z} = 0.172\,\mathrm{T} =: B_0$) a phase shift of π occurs (highlighted by the blue circles in Fig. 3.6a), which is not explainable within the framework of the AB effect. Moreover, this observation is accompanied by an additional modulation of the magnetoconductance (intermediate maximum/minimum), which is indicated by the red arrow in Fig. 3.6a. These deviations from the standard pattern are also visible in Fig. 3.6b, which shows the background corrected magnetoconductance ΔG of QPC-I for $V_\mathrm{G} = -0.261\,\mathrm{V}$. The background corrected magnetoconductance is acquired by subtracting a smooth background (moving average) of the data shown in Fig. 3.6a. For $B_\mathrm{z} > B_0$, the resulting trace is well represented by a cosine function described by

$$\Delta G \sim \cos\left[\left(\frac{2\pi}{\rho_\mathrm{AB}}\right) \cdot B_\mathrm{z}\right] \tag{3.18}$$

with using the afore determined value of $\rho_\mathrm{AB} = 0.172\,\mathrm{T}$. The phase shift of π as well as the additional modulation are highlighted in Fig. 3.6b.

A third approach to demonstrate the accumulation of an AB phase is provided by utilizing the fast Fourier transformation (FFT) method. The latter analyses the frequency spectrum of

[3] It should be noted that the magnetic field dependence of the conductance is referred to as magnetoconductance. However, the ordinate of the associated plots is nonetheless labelled as conductance.

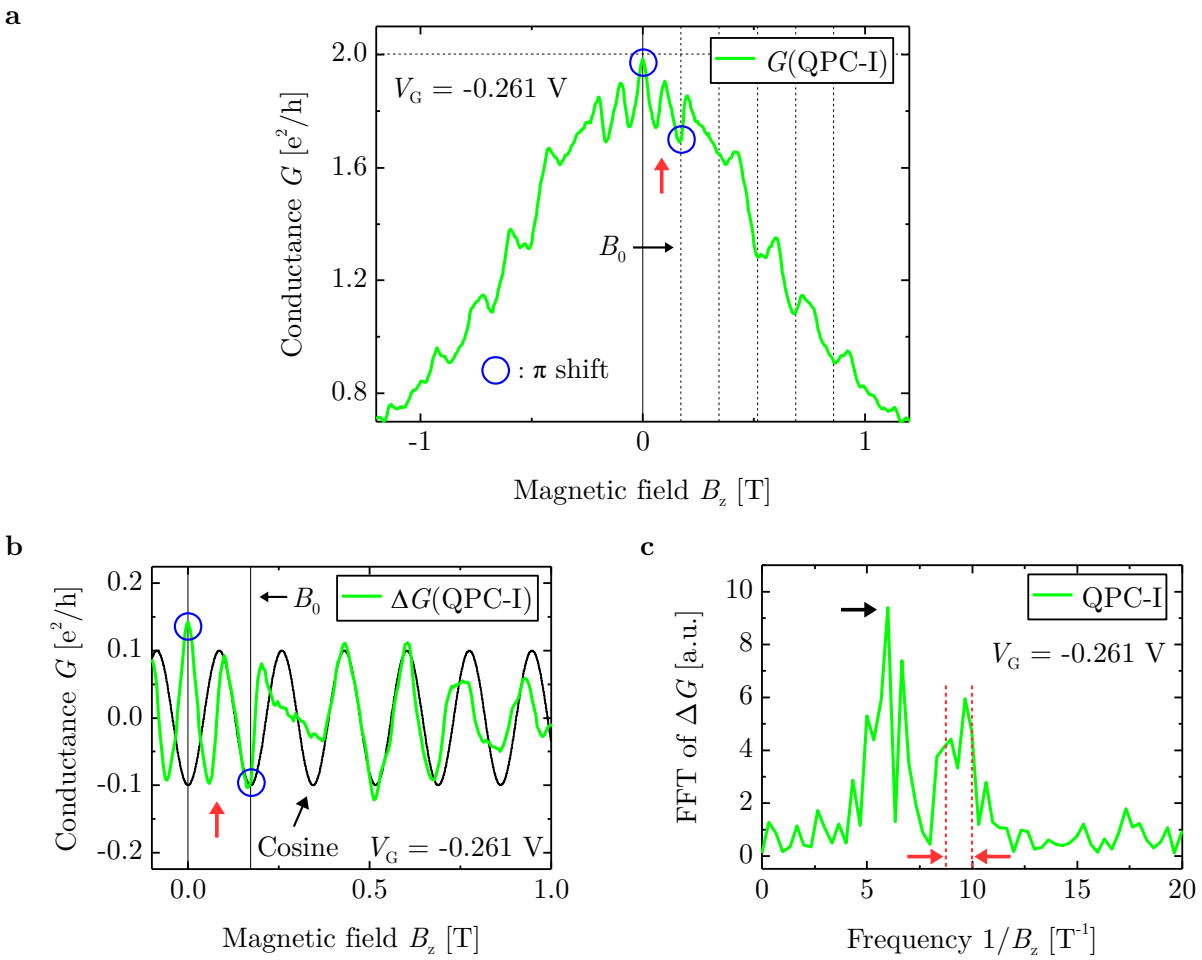

Figure 3.6: **a**, Magnetoconductance G of QPC-I measured at $V_G = -0.261\,V$ (regime II). Periods are indicated by vertical lines. The blue circles highlight a phase shift of π, which emerges within the first AB period. This shift is accompanied by an additional modulation of the magnetoconductance (intermediate maximum/minimum), which is indicated by the red arrow. **b**, Background corrected magnetoconductance ΔG of QPC-I for $V_G = 0.261\,V$ compared with Eq. 3.18 using $\rho_{AB} = 0.172\,T$. **c**, FFT of the background corrected magnetoconductance of QPC-I shown in panel **b**. The frequencies attributed to the AB effect (black arrow) and to the additional modulation within the first AB period (red arrows) are indicated.

a modulated signal and helps to identify dominant components. For magnetoconductance data modulated by the AB effect, it is an established approach to perform FFT analysis based on the derivative $dG(B_z)/dB_z$ [40] or on the background corrected magnetoconductance ΔG [41] – both methods reduce the influence of the slowly varying background. The FFT analysis of the data shown in Fig. 3.6b is presented in Fig. 3.6c. The maximum of the FFT transformed data at $1/B_z \approx 5.9\,T^{-1}$ is attributed to the AB effect (corresponds to $\rho_{AB} \approx 0.17\,T$). The impact of the additional modulation within the first AB period is highlighted by the red arrows.

Moreover, the magnetoconductance of QPC-I presented in Fig. 3.6a exhibits an overall decay for increasing magnetic field values. This observation is in accordance with theory [42–44] and is caused by the breaking of time reversal symmetry. The latter allows for the occurrence of backscattering events, hence reducing the magnetoconductance compared to the $B_z = 0\,T$ case.

3.3.2 Accumulation of a dynamical Aharonov-Casher phase

The gate voltage dependence of the conductance of QPC-I with focus on parts of the QSH regime is shown in Fig. 3.7a. It is well represented by a cosine function described by

$$\Delta G \sim \cos\left[\left(\frac{2\pi}{\rho_{\mathrm{AC}}}\right) \cdot V_{\mathrm{G}}\right] \tag{3.19}$$

and exhibits a period of $\rho_{\mathrm{AC}} \approx 10\,\mathrm{mV}$. This result is of particular interest, since it demonstrates the manipulability of the QSH conductance by all-electrical means, which is attributed to the impact of the dynamical AC phase.

Furthermore, combining the analysis of both so far discussed quantum interference effects, the magnetoconductance of QPC-I is presented in Fig. 3.7b for a certain gate voltage range in 1 mV steps. For reasons of clarity, the derivative $\mathrm{d}G(B_{\mathrm{z}})/\mathrm{d}B_{\mathrm{z}}$ of the magnetoconductance is plotted, which allows for a good differentiation between maxima and minima. The observable equidistant spacing within the fan-like pattern is caused by the AB phase, while the diagonal character of the grid lines demonstrates the impact of the dynamical AC phase [9]. This unperturbed observation of the combination of AB and AC interference provides evidence that both related quantum phases influence the interference conditions within the examined QSH interferometer independently.

The perturbation-free interplay between the AB phase and the dynamical AC phase becomes also visible when analysing single magnetoconductance traces. In this context, Fig. 3.7c shows the magnetoconductance of QPC-I at $V_{\mathrm{G}} = -0.261\,\mathrm{V}$ as well as at $V_{\mathrm{G}} = -0.271\,\mathrm{V}$. The impact of the dynamical AC phase becomes manifest in the inversion of all observable patterns and signatures, while the period ρ_{AB} caused by the accumulation of the AB phase remains unaffected. Both gate voltage values are indicated in Fig. 3.7a,b.

3.3.3 Accumulation of a spin-orbit Berry phase

In order to track down the impact of the spin-orbit Berry phase, the observed phase shift of π within the first AB period of the modulated magnetoconductance has to be recalled. If the effective field $\mathbf{B}_{\mathrm{Eff.}}$ and thus the spin precession axis are assumed to align themselves sufficiently to $\mathbf{B}_{\mathrm{z}}$ within the first AB period, the value of the accumulated spin-orbit Berry phase would reduce to $\varphi_{\mathrm{SB}} \approx 0$ for $B_{\mathrm{z}} \approx B_0$ (see Fig. 3.5b). As a consequence, the net phase balance for the transition $B_{\mathrm{z}} = 0\,\mathrm{T} \rightarrow B_{\mathrm{z}} = B_0$ would yield

$$\Delta\varphi \approx -\varphi_{\mathrm{SB}} + \varphi_{\mathrm{AB}} = -\pi + 2\pi = \pi\,. \tag{3.20}$$

This relation presumes $\varphi_{\mathrm{SB}} = \pi$ for $B_{\mathrm{z}} = 0\,\mathrm{T}$, as it is the case for the adiabatic regime.

Acquisition of a spin-orbit Berry phase of π

To verify the validity of the previous assumption, the gate voltage dependence of the conductance of QPC-I for $B_{\mathrm{z}} = 0\,\mathrm{T}$ and $B_{\mathrm{z}} = B_0$ with focus on parts of the QSH regime is

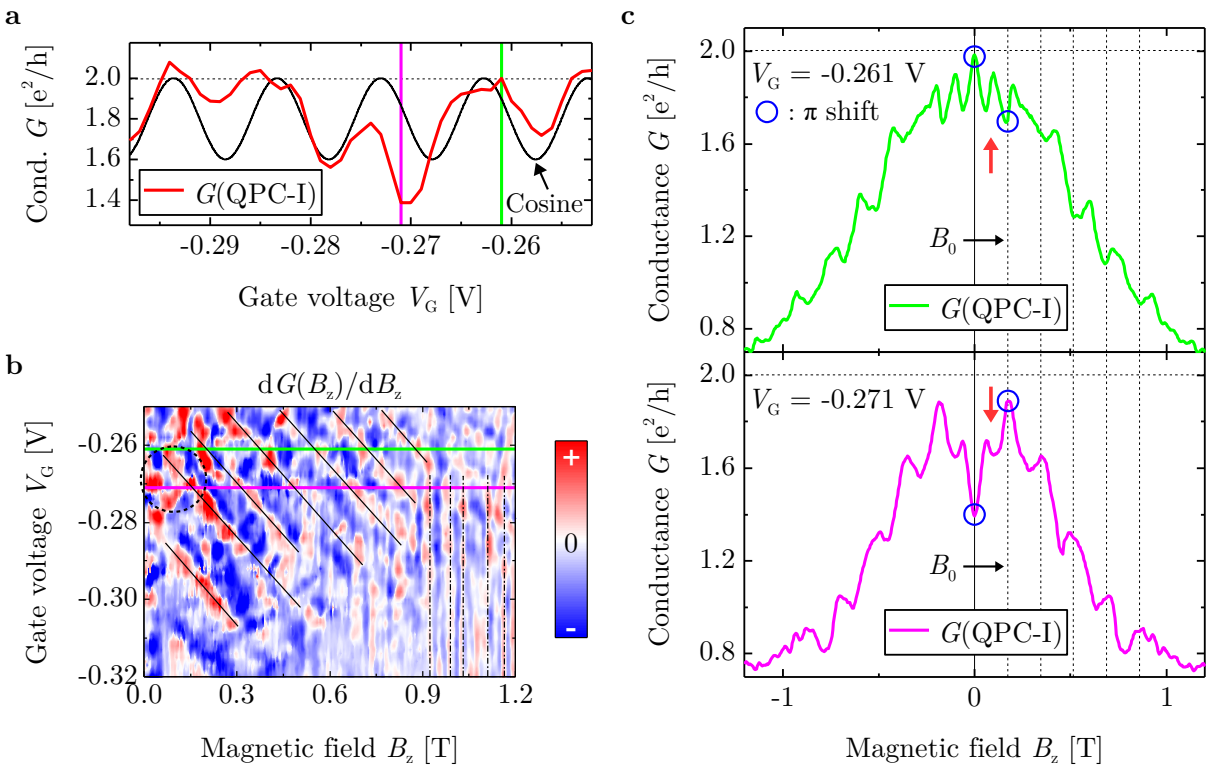

Figure 3.7: **a**, Gate voltage V_G dependence of the conductance G of QPC-I with focus on parts of the QSH regime compared with Eq. 3.19 using $\rho_\mathrm{AC} \approx 10\,\mathrm{mV}$. The vertical lines highlight the gate voltage values of the data presented in panel **c**. The data of panel **a** was acquired performing another measurement in addition to the data shown in Fig. 2.11. The shift of the conductance with regard to the applied gate voltage between both measurements is due to thermal cycling. **b**, Derivative $\mathrm{d}G(B_\mathrm{z})/\mathrm{d}B_\mathrm{z}$ of the magnetoconductance G of QPC-I for different values of the gate voltage. Straight black lines are added as a guide to the eye. The coloured lines indicate the gate voltage values of the data presented in panel **c**. The dashed black circle highlights the area presented in Fig. 3.9a. The vertical dashed-dot-lines point at a gate voltage independent pattern. **c**, Magnetoconductance of QPC-I for two values of the gate voltage (regime II). Periods are indicated by vertical lines. The blue circles highlight a phase shift of π, which emerges within the first AB period. This shift is accompanied by an additional modulation of the magnetoconductance (intermediate maximum/minimum), which is indicated by the red arrows. The green trace is equivalent to the data shown in Fig. 3.6a.

presented in Fig. 3.8a as a first step. The observable range of anti-phase oscillation behaviour is in accordance with a phase shift of π between the two different system conditions. Such a scenario is anticipated by theory for two distinct states of a QSH interferometer, which differ in phase due to the acquisition of a spin Berry phase of π [45, 46].

As a second step, the impact of the spin-orbit Berry phase (Eq. 3.17) is added to the description of the AB phase induced modulation of the magnetoconductance [5] (Eq. 3.18). Moreover, the influence of the dynamical AC phase is included (Eq. 3.19), which altogether yields

$$\Delta G(B_\mathrm{z}, V_\mathrm{G}) \sim \cos\left\{\left[\left(\frac{2\pi}{\rho_\mathrm{AB}}\right)\cdot B_\mathrm{z}\right] - \pi\left[1-\cos\left(\arctan\left(\frac{B_\mathrm{R}}{|B_\mathrm{z}|}\right)\right)\right]\right\}\cdot\cos\left[\left(\frac{2\pi}{\rho_\mathrm{AC}}\right)\cdot V_\mathrm{G}\right]. \quad (3.21)$$

Figure 3.8b shows a fit of the background corrected magnetoconductance for two different values of the gate voltage using Eq. 3.21 with $\rho_\mathrm{AB} = 0.172\,\mathrm{T}$, $B_\mathrm{R} = B_0/2$ and $\cos((2\pi/\rho_\mathrm{AC})\cdot V_\mathrm{G}) = \pm 1$.

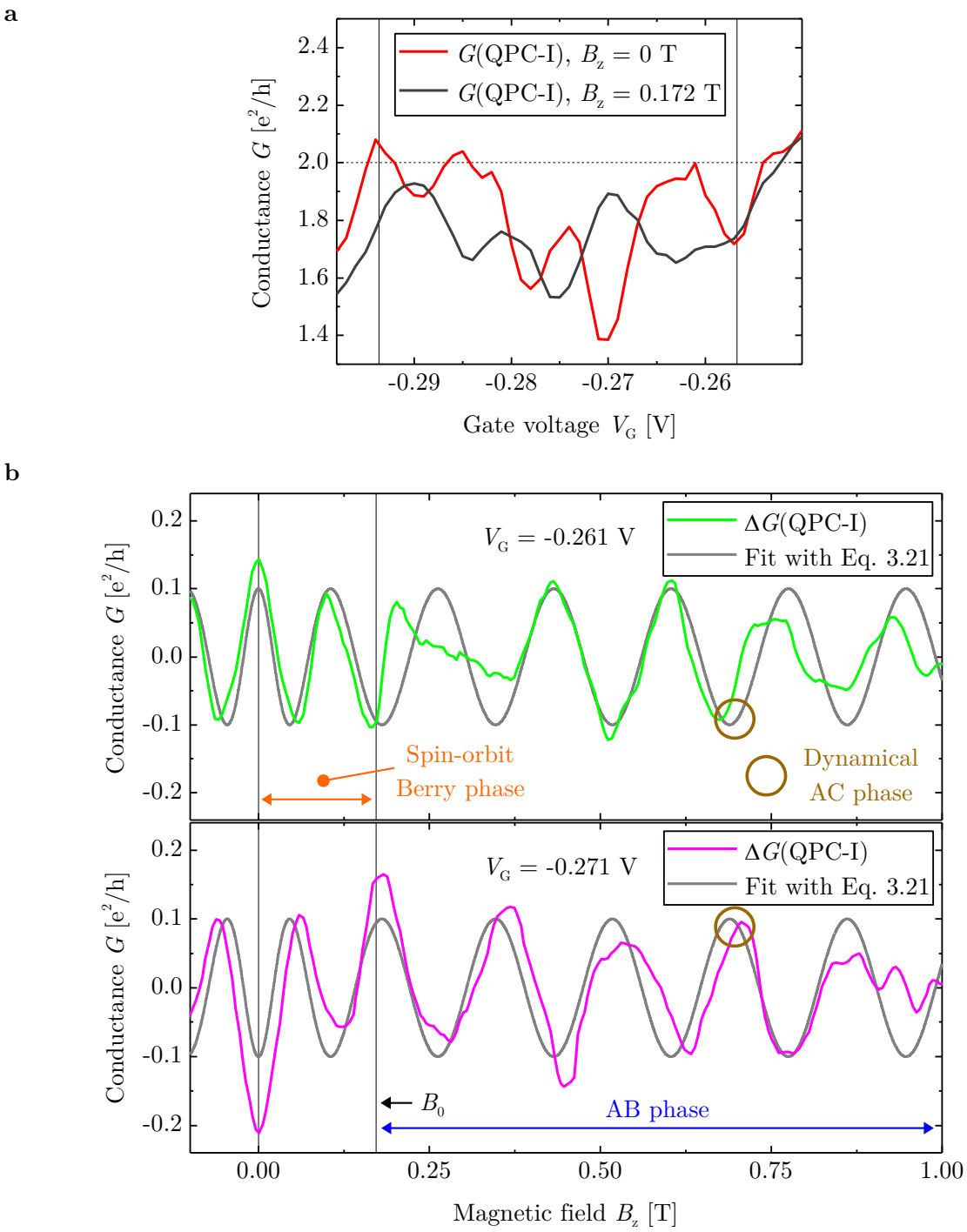

Figure 3.8: **a**, Gate voltage V_G dependence of the conductance G of QPC-I for $B_z = 0\,\mathrm{T}$ and for $B_z = B_0 = 0.172\,\mathrm{T}$ with focus on parts of the QSH regime. The red trace is equivalent to the data shown in Fig. 3.7a. **b**, Background corrected magnetoconductance ΔG of QPC-I for two values of the gate voltage fitted with Eq. 3.21. The fitting parameters are $\rho_{AB} = 0.172\,\mathrm{T}$, $B_R = B_0/2 = 0.086\,\mathrm{T}$ and $\cos[(2\pi/\rho_{AC}) \cdot V_G] = \pm 1$. The impact of the AB phase, of the dynamical AC phase and of the spin-orbit Berry phase of π is indicated.

The impact of the spin-orbit Berry phase of π, of the AB phase as well as of the dynamical AC phase is indicated.

By further including the observed period of the modulation of the gate voltage dependence of the conductance $\rho_{\mathrm{AC}} = 10\,\mathrm{mV}$, Eq. 3.21 can be used to calculate a full 2D pattern of the associated conductance modulation within the spin-orbit Berry phase regime. When calculating the corresponding partial derivative $\partial G(B_{\mathrm{z}}, V_{\mathrm{G}})/\partial B_{\mathrm{z}}$, the analytical description can be compared with the acquired data, which is shown in Fig. 3.9. Moreover, by performing the calculation for larger ranges of the gate voltage and of the magnetic field, a pattern describable by equidistant diagonal lines emerges for $B_{\mathrm{z}} > B_0$, which is shown in Fig. 3.10. The latter is in accordance with experimental observations presented in Fig. 3.7b.

Quantification of the Rashba coupling strength ξ_{R}

The utilized parameter $B_{\mathrm{R}} = B_0/2$ can be approximately related to a quantitative value of the Rashba coupling strength ξ_{R} by using the relation [47]

$$\xi_{\mathrm{R}} = \frac{g\mu_{\mathrm{B}} B_{\mathrm{R}}}{2k}\,, \tag{3.22}$$

where g represents the g-factor, k is the electron momentum and μ_{B} is the Bohr magneton. With using $g \approx 55.5$ [48] and $k \approx 0.01\,\mathrm{nm}^{-1}$ (around the Dirac point, see Fig. 3.2a), Eq. 3.22 yields a value of $\xi_{\mathrm{R}} \approx 13.8\,\mathrm{peVm}$. This result is 5–10× larger than values in ring structures hosting the non-adiabatic regime [23], thus justifying the assumed presence of adiabaticity in QSH interferometers emerging within topological HgTe based QPCs.

Assessment of the results

The model formulated by Eq. 3.21 is based on the assumption of an accumulation of a spin-orbit Berry phase of π at zero magnetic field due to the presence of the adiabatic transport regime. The consistency between the analytic description and the acquired experimental data presented in Fig. 3.8 and Fig. 3.9 legitimizes this hypothesis. Thus, the presence of the spin-orbit Berry phase of π reveals itself indirectly within the first period of the AB modulation of the magnetoconductance – by the observable π shift as well as by the additional modulation (intermediate maximum/minimum).

Moreover, the presented results demonstrate the possibility to appropriately describe the response of the discussed experimental system towards two external parameters. This accordance between analytic model and experiment is noteworthy, since the QSH regime has to be characterized as highly complex and fragile under experimental conditions – above all under the influence of an applied magnetic field. Hence, the presented data demonstrates the resilience of the emerging QSH interferometer state and substantiates the quality of the utilized device technology.

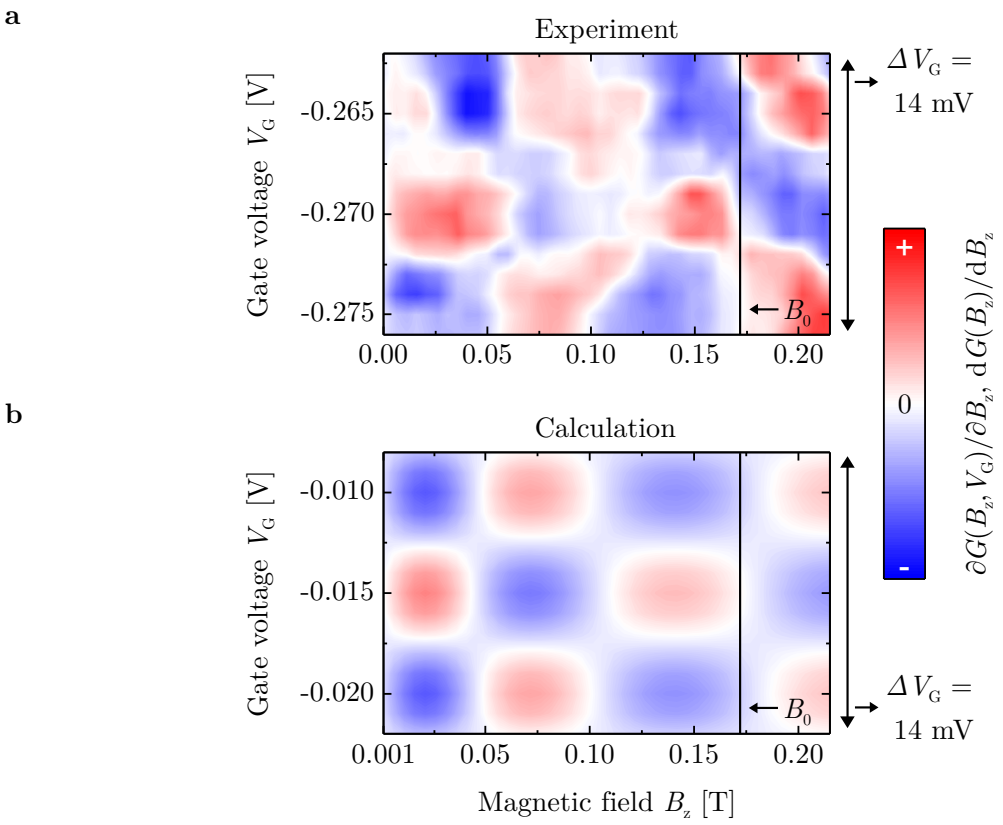

Figure 3.9: **a**, Derivative $dG(B_z)/dB_z$ of the measured magnetoconductance G of QPC-I for different values of the gate voltage V_G with focus on the spin-orbit Berry phase regime. The panel shows a replotted zoom on the data presented in Fig. 3.7b. **b**, Calculation of $\partial G(B_z, V_G)/\partial B_z$ using Eq. 3.21 with $\rho_{AB} = 0.172\,T$, $\rho_{AC} = 10\,mV$ and $B_R = B_0/2 = 0.086\,T$.

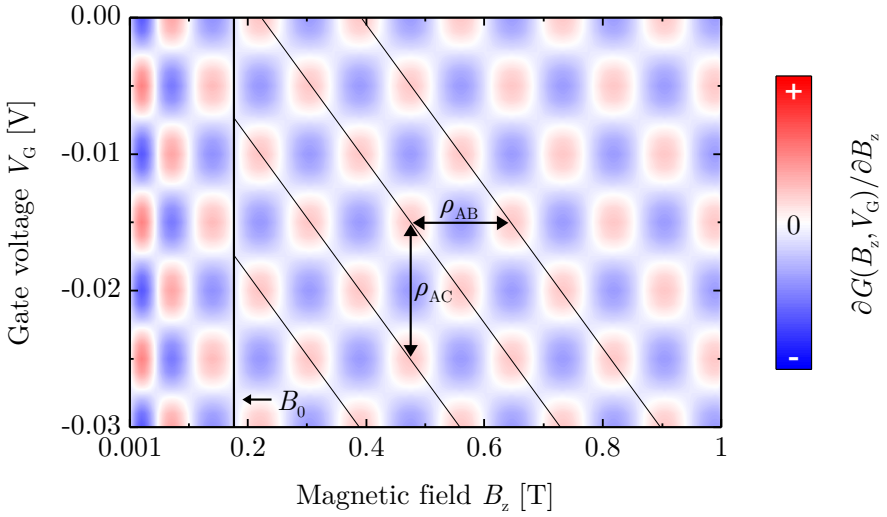

Figure 3.10: Calculation of $\partial G(B_z, V_G)/\partial B_z$ for larger ranges of the gate voltage V_G and of the magnetic field B_z using Eq. 3.21 with $\rho_{AB} = 0.172\,T$, $\rho_{AC} = 10\,mV$ and $B_R = B_0/2 = 0.086\,T$.

3.3.4 Exclusion of alternative mechanisms

Universal conductance fluctuations

The observed periodic modulation of the magnetoconductance within regime II of the QSH regime is attributed to the impact of the AB phase. In the context of some experiments, a modulation of the magnetoconductance can also be related to the occurrence of universal conductance fluctuations (UCF, for an introduction see for example Ref. [5]). However, such an UCF induced modulation is aperiodic [49, 50] and furthermore not assignable to the area of the analysed device (due to the physical origin of UCF). Moreover, the concept of UCF is incompatible with a quantized QSH system per se, since the effect solely emerges in the diffusive transport regime.

Switching between localization effects

The change of sign of the derivative of the magnetoconductance around $B_z = 0\,\mathrm{T}$ for different values of the gate voltage, which is accompanied by an inversion of the whole oscillation pattern, is attributed to the accumulation of a dynamical AC phase. An alternative effect, which would lead to a similar behaviour of the magnetoconductance around $B_z = 0\,\mathrm{T}$, is represented by the hypothetical transition from weak antilocalization (WAL) to weak localization (WL) and vice versa. For an introduction to both effects, the interested reader is referred for example to Ref. [5]. However, also WAL and WL only occur in the diffusive transport regime, which makes them incompatible with a quantized QSH system. A theoretical study of an anticipated switching behaviour between WAL and WL in diffusive inverted HgTe quantum wells is provided by Ref. [51].

3.4 Experimental verification of the quantum spin Hall ring formation model

The proposed model describing the emergence of a QSH interferometer state in topological QPC devices is based on the fulfilment of the condition $2\sigma_y + \lambda_F \gtrapprox W_{QPC}$ (see Eq. 3.2). Thus, the validity of the model can be verified by varying each component of Eq. 3.2 individually and, subsequently, by monitoring the corresponding impact on the magnetoconductance. However, the utilized device concept makes it impossible to modify the Fermi wavelength λ_F of the incident electrons, since this scenario would require separately gated equilibrium reservoirs. Hence, a sanity check of the model can be performed by changing:

- the spatial extension σ_y of the QSH edge states;
- the width W_{QPC} of the QPC device.

While the spatial extension of the helical edge states can be adjusted by tuning the Fermi level, the alteration of the sample width obviously necessitates a QPC device with a larger value of W_{QPC}.

3.4.1 Tuning of the edge channel width

The helical spectrum of the band structure calculation shown in Fig. 3.2a is categorized by three regimes. When the Fermi level is located within regime II, a QSH interferometer state emerges due to spatially extended helical edge channels – based on the assumption that the condition of Eq. 3.2 is met. In such a scenario, as discussed for the case of QPC-I, an AB phase induced modulation of the magnetoconductance is observable. However, if the proposed model capturing the emergence of a QSH interferometer is correct, one would expect the AB modulation of the magnetoconductance to occur only in a limited gate voltage range (regime II). This is related to the fact that with pushing the Fermi level into regime I/III of the helical spectrum, a transition from spatially extended to spatially localized QSH edge channels and thus a reduction of σ_y is taking place (see Fig. 3.2a). Then, after passing a certain threshold value, the condition defined by Eq. 3.2 is not met anymore and the modulation of the magnetoconductance is expected to gradually diminish.

In this context, Fig. 3.11a shows the magnetoconductance of QPC-I for a gate voltage approaching the n-conducting regime (regime I), while Fig. 3.11b presents a measurement close to the p-conducting regime (regime III). In both cases, the periodic modulation of the magnetoconductance is abated. Pushing the Fermi level even further and thus entering the n-n'-n regime (Fig. 3.11c) or the n-p-n regime (Fig. 3.11d) results in an eventual losing of the interference pattern. The corresponding gate voltage dependence of the conductance is shown in Fig. 3.11e. The latter consists of two individual measurements, since the n-n'-n regime was not captured by the measurement of the black trace. The gate voltage values of the data shown in Fig. 3.11a–d are indicated, the green and the magenta trace represent the gate voltage values of the data shown in Fig. 3.7c. It should be noted that the effect of reducing the spatial extension of the QSH edge channels also becomes manifest in the losing of the anti-phase oscillation behaviour shown in Fig. 3.8a.

3.4.2 Alteration of the device width

Since the utilized QPC device concept is based on etched constrictions, modifying the width W_{QPC} in the context of Eq. 3.2 requires a dedicated sample. For this purpose, the device QPC-V with a width of $W_{\mathrm{QPC}} \approx 250\,\mathrm{nm}$ is analysed. Other than that, the sample exhibits the same dimensions and the same quantum well thickness as QPC-I (for details, see Tab. 3.1). Furthermore, the wafer materials utilized for the fabrication of both devices have similar electron densities, thus ensuring that the reservoirs supply electrons with a comparable Fermi wavelength. For QPC-V, the Fermi wavelength of the incident electrons is $\lambda_{\mathrm{F}} \approx 36\,\mathrm{nm}$, while it is $\lambda_{\mathrm{F}} \approx 35\,\mathrm{nm}$ for the case of QPC-I.

Figure 3.12a shows the gate voltage dependence of the conductance of QPC-V, the vertical line indicates the gate voltage value of the data shown in Fig. 3.12d. Conductance steps of $\Delta G \approx 2e^2/h$ can be identified with decreasing gate voltage values within the n-n'-n regime and a residual conductance of $G_{\mathrm{QSH}} \approx 2e^2/h$ is observed within the n-i-n regime. For even more

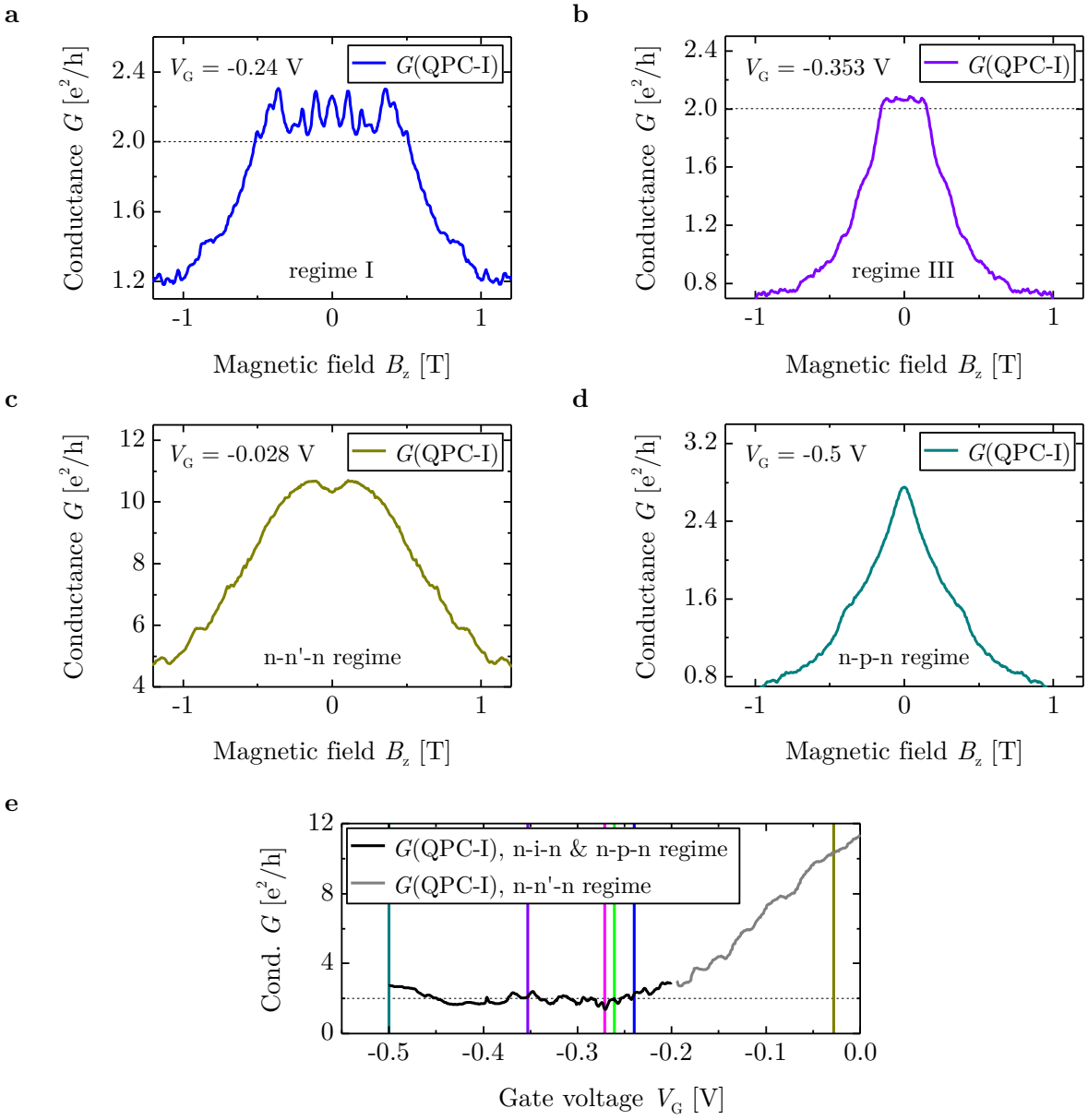

Figure 3.11: **a**–**d**, Magnetoconductance G of QPC-I for different values of the gate voltage V_G. The attributed transport regimes are indicated. **e**, Composite gate voltage dependence of the conductance G of QPC-I. The vertical lines highlight the gate voltage values of the data shown in panels **a**–**d** as well as of the data shown in Fig. 3.7c. The black trace is equivalent to the data shown in Fig. 3.7a. The grey trace is equivalent to the data of QPC-I shown in Fig. 2.11, but is shifted with regard to the gate voltage axis due to reasons of presentation.

negative gate voltages, the slightly increasing conductance values are associated with entering the n-p-n regime. A serial resistance of $R_{\mathrm{Serial}} = 1450\,\Omega$ is subtracted for the corrected trace.

A $\mathbf{k}\cdot\mathbf{p}$ band structure calculation for a semi-finite ribbon with $W_y = 250\,\mathrm{nm}$ and $d_{\mathrm{QW}} = 7\,\mathrm{nm}$ is presented in Fig. 3.12b. In the vicinity of the Dirac point and thus for regime II, the spatial extension of the QSH edge channels exhibits a value of $\sigma_y \approx 35$–$45\,\mathrm{nm}$. Using the upper limit of σ_y as well as the afore mentioned values of W_{QPC} and λ_F, Eq. 3.2 yields $(2\cdot 45 + 36)\,\mathrm{nm} < 250\,\mathrm{nm}$.

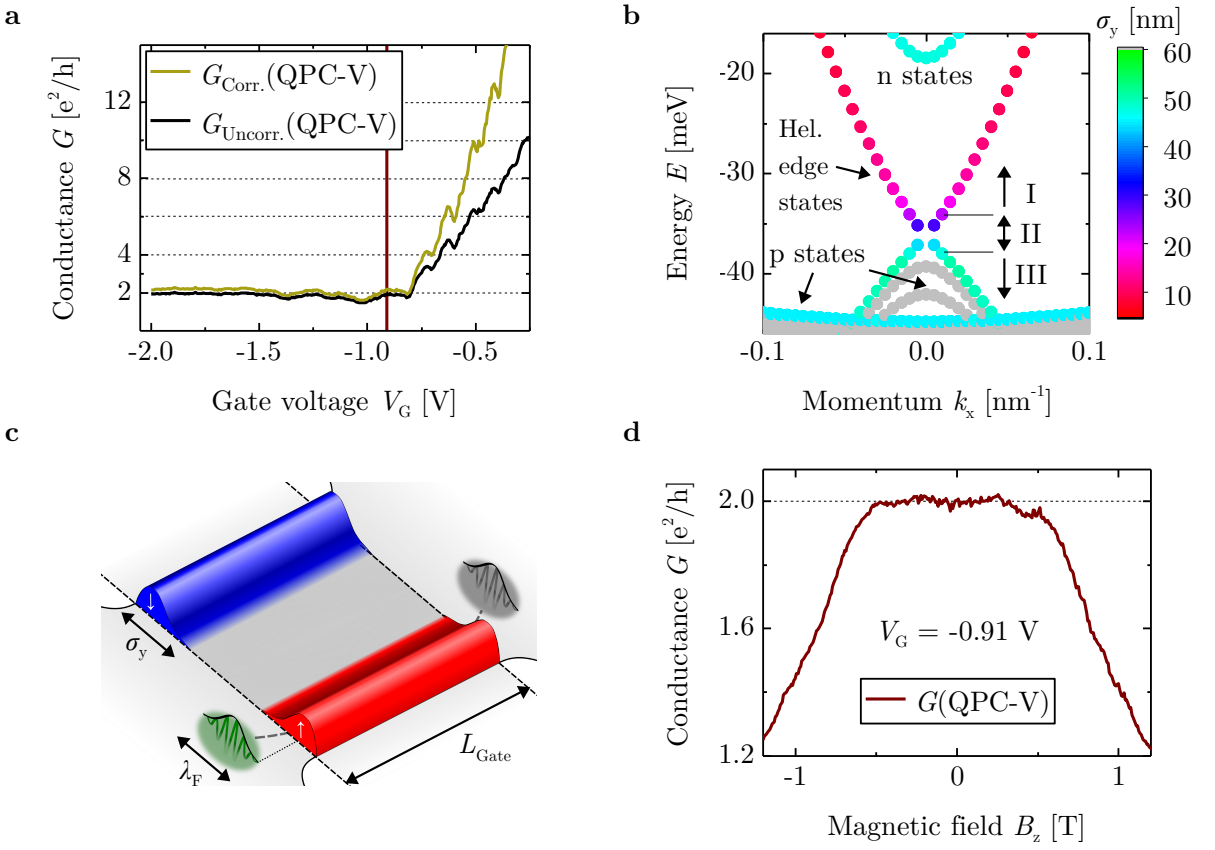

Figure 3.12: **a**, Gate voltage V_G dependence of the conductance G of QPC-V. The device exhibits a width of $W_\mathrm{QPC} \approx 250\,\mathrm{nm}$. The vertical line highlights the gate voltage value of the data presented in panel **d**. A serial resistance of $R_\mathrm{Serial} = 1450\,\Omega$ is subtracted for the corrected trace, which is equivalent to the data shown in Fig. 2.12c. **b**, $\mathbf{k}\cdot\mathbf{p}$ band structure calculation for a semi-finite ribbon with $W_\mathrm{y} = 250\,\mathrm{nm}$ and $d_\mathrm{QW} = 7\,\mathrm{nm}$. The colour code indicates the standard deviation σ_y of the wave function in y direction, which is categorized by three regimes. **c**, For $W_\mathrm{QPC} \gg 100\,\mathrm{nm}$, the condition $2\sigma_\mathrm{y} + \lambda_\mathrm{F} \gtrapprox W_\mathrm{QPC}$ is not met anymore within regime II, thus no interferometer state emerges. **d**, Magnetoconductance G of QPC-V measured at $V_\mathrm{G} = -0.91\,\mathrm{V}$. No serial resistance is subtracted.

Thus, no formation of a QSH interferometer state is expected for the case of QPC-V (see Fig. 3.12c for a sketch), which is in accordance with the data shown in Fig. 3.12d. There, the presented magnetoconductance of QPC-V measured at $V_\mathrm{G} = -0.91\,\mathrm{V}$ does not exhibit an indication of a periodic modulation.

It should be noted that the trend of the change of the spatial localization of the QSH edge channels is slightly different for a ribbon with $W_\mathrm{y} = 250\,\mathrm{nm}$ than for the case of $W_\mathrm{y} = 100\,\mathrm{nm}$ (see Fig. 3.12b). While the transition from regime II to regime I is qualitatively similar for both cases (σ_y decreases), an inverted behaviour is observable for the transition from regime II to regime III. For $W_\mathrm{y} = 250\,\mathrm{nm}$, the value of σ_y increases even further with entering regime III – contrary to the case of $W_\mathrm{y} = 100\,\mathrm{nm}$. However, also within regime III, the condition of Eq. 3.2 is not met ($\sigma_\mathrm{y} \approx 50\,\mathrm{nm}$).

3.5 Reproduction of the results

The observation of the introduced quantum interference effects and thus the emergence of a QSH interferometer state is demonstrated for two more devices. The analysis of QPC-VII (a replica of QPC-I) reveals the influence of the three expected quantum phases and hence reproduces the afore discussed data set entirely. For the case of QPC-VIII, no impact of a spin-orbit Berry phase is observable. This absence is explainable with the geometry of the propagation path, which differs from samples QPC-I and QPC-VII due to altered device dimensions.

3.5.1 Standard type device QPC-VII

Aharonov-Bohm phase

The gate voltage dependence of the conductance of QPC-VII ($\lambda_F \approx 35\,\mathrm{nm}$) is shown in Fig. 3.13a. The conductance exhibits values of $G \in [0.5 \cdot G_{\mathrm{QSH}}; G_{\mathrm{QSH}}]$ within the n-i-n regime, thus showing topological behaviour. Conductance quantization within the n-n'-n regime due to trivial ballistic 1D transport is not observable.

The magnetoconductance of QPC-VII measured at $V_G = -0.28\,\mathrm{V}$ is presented in Fig. 3.13b. The latter reproduces all observations made for QPC-I – a periodic modulation indicated by vertical lines and, with regard to the first AB period, a phase shift of π accompanied by an additional modulation (intermediate maximum/minimum). The magnetic field value of the intermediate minimum $B_z \approx 0.085\,\mathrm{T}$ is referred to as $B^{\dagger}$. Inserting the observable period of $\rho_{\mathrm{AB}} \approx 0.2\,\mathrm{T}$ into Eq. 3.12 yields an encircled area of $A \approx 20.7{\cdot}10^3\,\mathrm{nm}^2$, while the dimensions of the device imply a gated area of approximately $A_{\mathrm{QPC}} = L_{\mathrm{Gate}}{\cdot}W_{\mathrm{QPC}} \approx 250\,\mathrm{nm}{\cdot}100\,\mathrm{nm} = 25{\cdot}10^3\,\mathrm{nm}^2$ (see also Tab. 3.1). The smaller value in comparison with QPC-I could be related to a slightly smaller value of L_{Gate} or a marginally overetched mesa.

Dynamical Aharonov-Casher phase

In order to examine the impact of the dynamical AC phase, a smooth background (moving average) is subtracted from the gate voltage dependence of the conductance of QPC-VII shown in Fig. 3.13a. The result is presented in Fig. 3.13c, where it is analysed using Eq. 3.19. The observable period of $\rho_{\mathrm{AC}} \approx 9\,\mathrm{mV}$ is in accordance with the obtained value for QPC-I. This finding is of particular interest, since it demonstrates that the Rashba coupling strength (and thus the dynamical AC phase induced modulation of the conductance, see Eq. 3.14) is reproducibly tunable for devices of similar geometry and layer stack.

Moreover, a change of sign of the derivative of the magnetoconductance around $B_z = 0\,\mathrm{T}$ for different values of the gate voltage is observed, which is presented in Fig. 3.13d–f. However, the AB phase induced modulation of the magnetoconductance is less distinct than for Fig. 3.13b. One possible reason is a reduced resilience of the QSH interferometer state towards an applied magnetic field due to pronounced potential fluctuations depending on the individual gate voltage value. In this context, also the overall less clean transport behaviour of QPC-VII should be noted (see Fig. 3.13a).

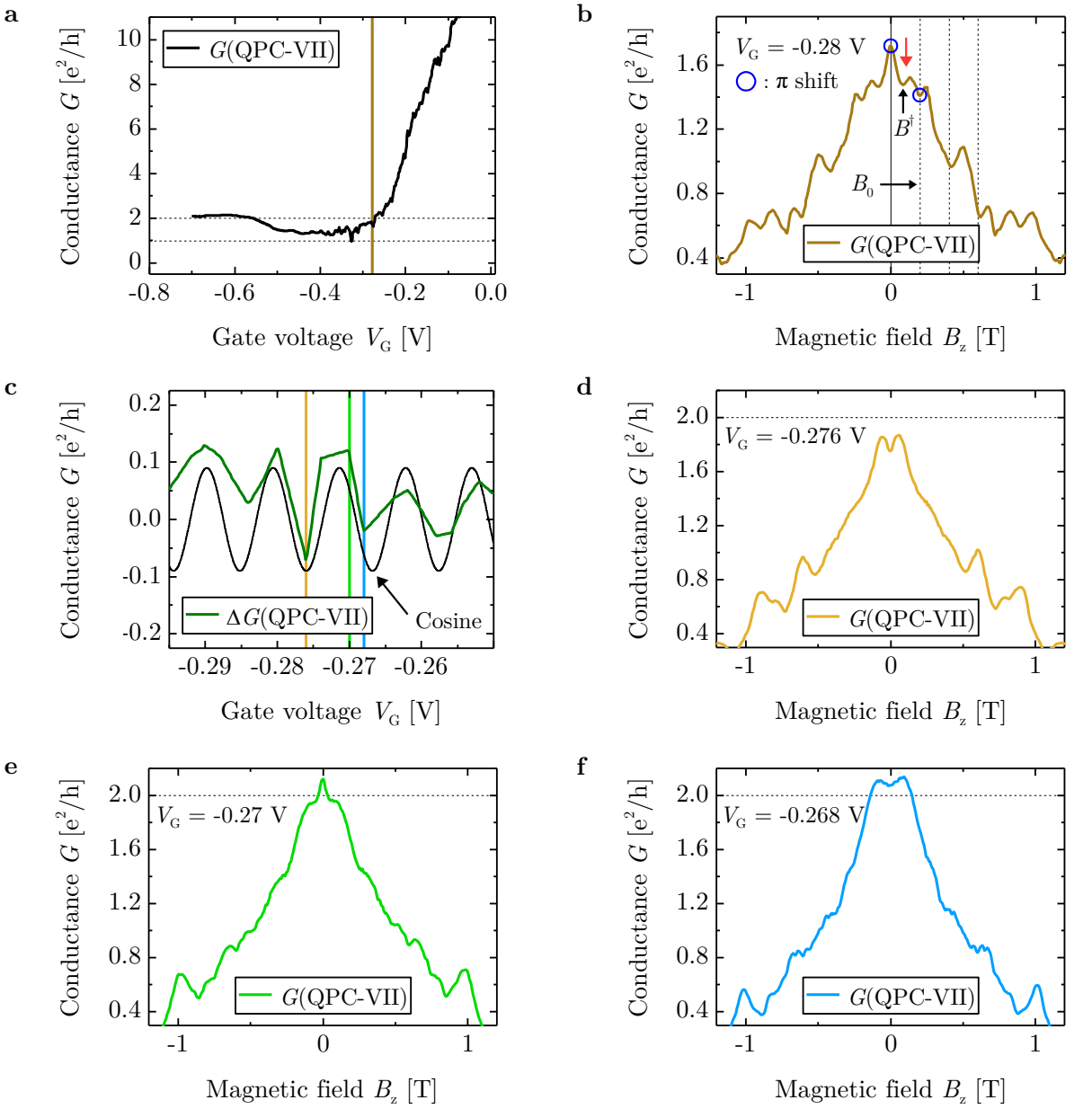

Figure 3.13: **a**, Gate voltage V_G dependence of the conductance G of QPC-VII. The vertical line highlights the gate voltage value of the data shown in panel **b**. **b**, Magnetoconductance G of QPC-VII measured at $V_G = -0.28\,V$ (regime II). Periods are indicated by vertical lines. The blue circles highlight a phase shift of π, which emerges within the first AB period. This shift is accompanied by an additional modulation (intermediate maximum/minimum), which is indicated by the red arrow. The magnetic field value of the intermediate minimum is referred to as $B^\dagger$. **c**, Background corrected gate voltage dependence of the conductance ΔG of QPC-VII with focus on parts of the QSH regime compared with Eq. 3.19 using $\rho_{AC} \approx 9\,mV$. The vertical lines highlight the gate voltage values of the data presented in panels **d**–**f**. **d**–**f**, Magnetoconductance of QPC-VII for different values of the gate voltage.

Spin-orbit Berry phase

Analogue to the case of QPC-I, the accumulation of a spin-orbit Berry phase of π becomes manifest in a phase shift of π and an additional modulation (intermediate maximum/minimum) within the first AB period. Figure 3.14a shows the comparison of the back-

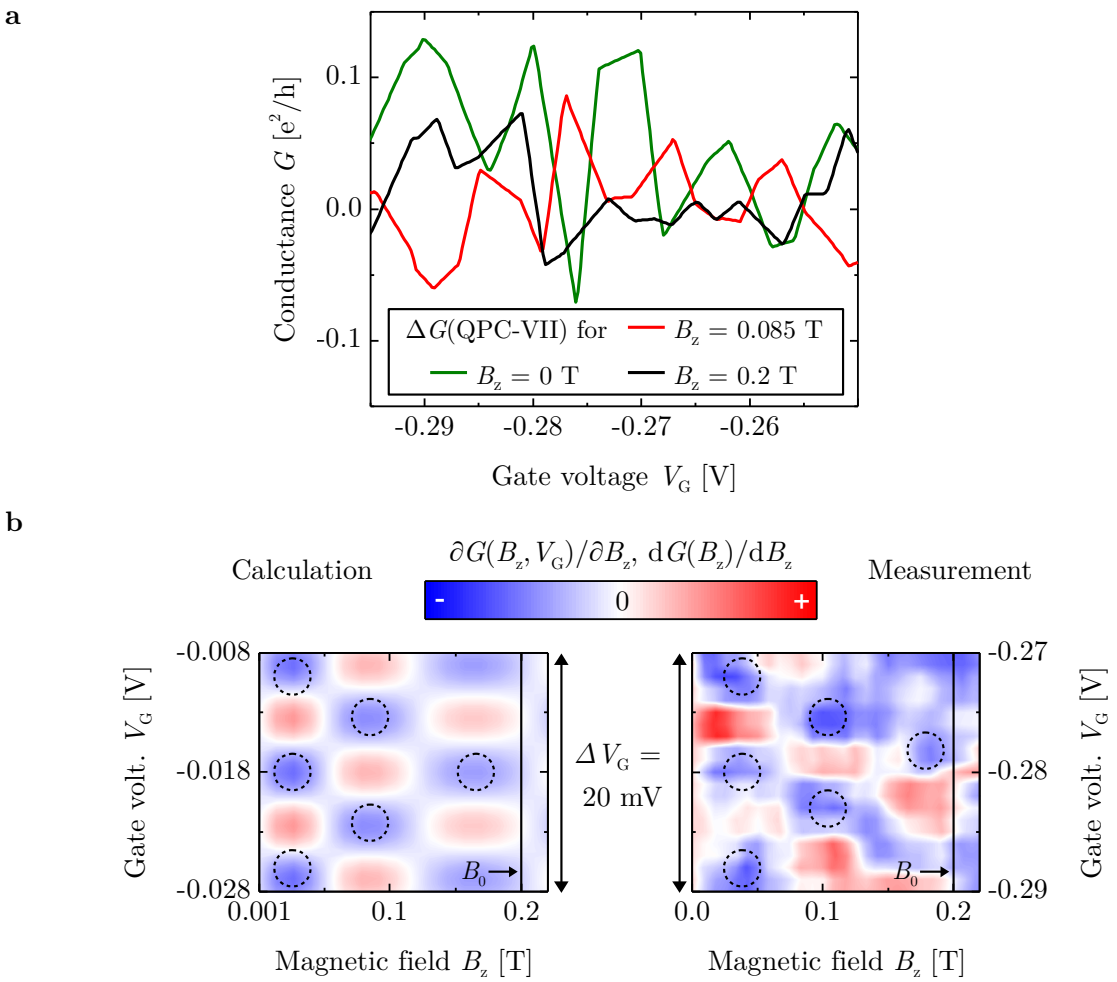

Figure 3.14: **a**, Background corrected gate voltage V_G dependence of the conductance ΔG of QPC-VII with focus on parts of the QSH regime for $B_z = 0\,T$, for $B_z = B^\dagger = 0.085\,T$ and for $B_z = B_0 = 0.2\,T$. The green trace is equivalent to the data shown in Fig. 3.13c. **b**, Derivative $dG(B_z)/dB_z$ of the measured magnetoconductance G of QPC-VII for different values of the gate voltage with focus on the spin-orbit Berry phase regime (right panel). The measured data is compared with a calculation of $\partial G(B_z, V_G)/\partial B_z$ using Eq. 3.21 with $\rho_{AB} = 0.2\,T$, $\rho_{AC} = 9\,mV$ and $B_R = B_0/2 = 0.1\,T$ (left panel). The dashed circles are added as a guide to the eye.

ground corrected gate voltage dependence of the conductance ΔG of QPC-VII for $B_z = 0\,T$ with the case of $B_z = 0.2\,T =: B_0$. Contrary to QPC-I, it does not exhibit an anti-phase behaviour. As before, this circumstance is attributed to a reduced resilience of QPC-VII towards magnetic field influence. However, it has to be noted that not only the type of extremum for $B_z = B_0$, but also the type of extremum described by $B_z = B^\dagger$ in Fig. 3.13b is inverse to the one at $B_z = 0\,T$. The comparison of the $B_z = 0\,T$ case with the measurement for $B_z = B^\dagger = 0.085\,T$ presented in Fig. 3.14a reveals the expected anti-phase behaviour.

Furthermore, Eq. 3.21 can be utilized to calculate a full 2D pattern of the conductance modulation within the spin-orbit Berry phase regime of QPC-VII. The corresponding partial derivative $\partial G(B_z, V_G)/\partial B_z$ can then be compared with a measured data set (see Fig. 3.14b). For calculation purposes, the parameters $\rho_{AB} = 0.2\,T$, $\rho_{AC} = 9\,mV$ and $B_R = B_0/2$ are used.

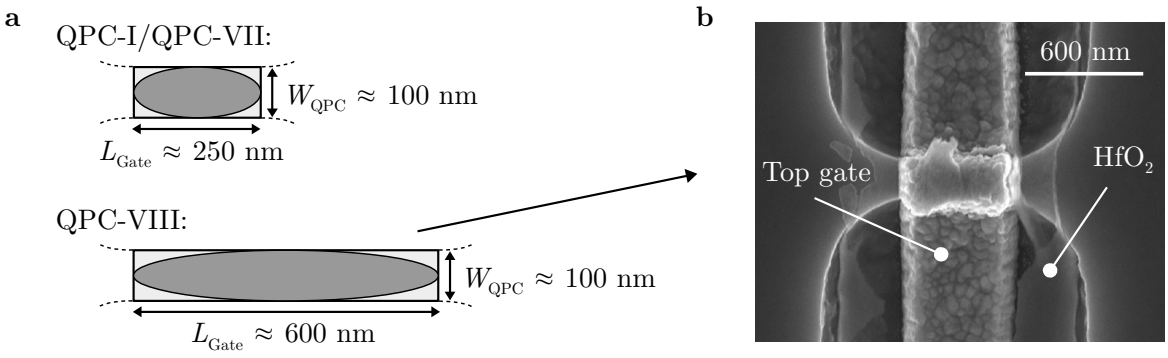

Figure 3.15: **a**, Sketch of the comparison of the gated device area with an ellipse. Relevant dimensions are indicated. **b**, Scanning electron micrograph of an exemplary QPC device with $L_{\mathrm{Gate}} \approx 600\,\mathrm{nm}$.

3.5.2 Elongated type device QPC-VIII

The device geometry of QPC-I, of QPC-VII as well as of QPC-VIII is schematically depicted in Fig. 3.15a. While for both geometries the gated area can be compared with an ellipse, a momentous difference is present with regard to the ratio of the two ellipse axes a/b. Following the work of Ref. [52], the authors predict that for the case of elliptically deformed quantum rings, the stability of the adiabatic regime depends on the aspect ratio of the system – with a threshold around $a/b \approx 0.35$. Below, rapid variations in the growing non-adiabatic term of the total spin geometric phase successively suppress the observability of the spin-orbit Berry phase of π.

Based on the values of ρ_{AB} (for QPC-VIII, see below) and on a value of $W_{\mathrm{QPC}} \approx 100\,\mathrm{nm}$, QPC-I and QPC-VII are characterized by $a/b \approx 0.4$–0.5, while QPC-VIII exhibits a value of $a/b \approx 0.17$. Thus, the analysis of QPC-VIII is assumed to not reveal any identifiable contribution of a spin-orbit Berry phase, which is in accordance with the to be presented data. Figure 3.15b shows a scanning electron micrograph of an exemplary QPC device with $L_{\mathrm{Gate}} \approx 600\,\mathrm{nm}$.

Aharonov-Bohm phase

The gate voltage dependence of the conductance of QPC-VIII ($\lambda_{\mathrm{F}} \approx 35\,\mathrm{nm}$) is shown in Fig. 3.16a. The red circles highlight the formation of plateau-like signatures within the n-n'-n regime. In the first segment of the n-i-n regime, the conductance fluctuates approximately within $G \in [0.5 \cdot G_{\mathrm{QSH}}; 1.2 \cdot G_{\mathrm{QSH}}]$ (see also Fig. 3.16d), thus showing topological behaviour. For more negative gate voltages, the less clean character of the sample becomes evident, which reveals itself also in abiding conductance values of $G < 2e^2/h$ for the n-p-n regime.

The magnetoconductance of QPC-VIII measured at $V_{\mathrm{G}} = -0.239\,\mathrm{V}$ is presented in Fig. 3.16b. It exhibits a periodic modulation indicated by vertical lines. Inserting the observable period of $\rho_{\mathrm{AB}} \approx 0.069\,\mathrm{T}$ into Eq. 3.12 yields an encircled area of $A \approx 60 \cdot 10^3\,\mathrm{nm}^2$, while a gated area of approximately $A_{\mathrm{QPC}} = L_{\mathrm{Gate}} \cdot W_{\mathrm{QPC}} \approx 600\,\mathrm{nm} \cdot 100\,\mathrm{nm} = 60 \cdot 10^3\,\mathrm{nm}^2$ is implied by the device dimensions (see also Tab. 3.1). The background corrected magnetoconductance of QPC-VIII for $V_{\mathrm{G}} = -0.239\,\mathrm{V}$ is presented in Fig. 3.16c, where it is compared with Eq. 3.18 using $\rho_{\mathrm{AB}} = 0.069\,\mathrm{T}$. Signatures associated with the impact of a spin-orbit Berry phase of π are not observable.

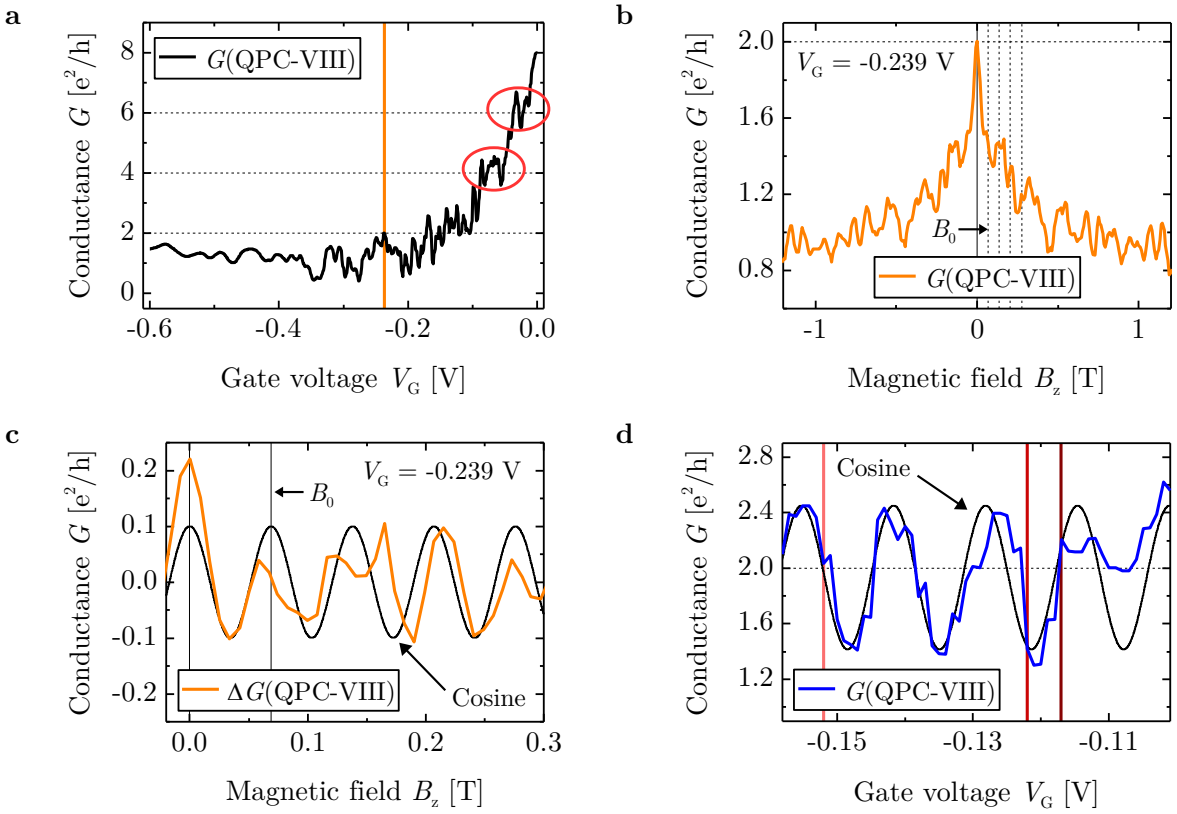

Figure 3.16: **a**, Gate voltage V_G dependence of the conductance G of QPC-VIII. The vertical line highlights the gate voltage value of the data shown in panel **b**, the red circles indicate the formation of plateau-like signatures due to trivial ballistic 1D transport. **b**, Magnetoconductance G of QPC-VIII measured at $V_G = -0.239\,\mathrm{V}$ (regime II). Periods are indicated by vertical lines. **c**, Background corrected magnetoconductance ΔG of QPC-VIII for $V_G = -0.239\,\mathrm{V}$ compared with Eq. 3.18 using $\rho_{AB} = 0.069\,\mathrm{T}$. **d**, Gate voltage dependence of the conductance of QPC-VIII with focus on parts of the QSH regime compared with Eq. 3.19 using $\rho_{AC} \approx 13.5\,\mathrm{mV}$. The vertical lines highlight the gate voltage values of the data presented in Fig. 3.17a–c. The data of panel **d** was acquired performing another measurement in addition to the data shown in panel **a**.

Dynamical Aharonov-Casher phase

An additional measurement of the gate voltage dependence of the conductance of QPC-VIII with focus on the entrance area of the n-i-n regime is presented in Fig. 3.16d. The data is analysed using Eq. 3.19 and a period of $\rho_{AC} \approx 13.5\,\mathrm{mV}$ is observable. Moreover, a change of sign of the derivative of the magnetoconductance around $B_z = 0\,\mathrm{T}$ for different values of the gate voltage is found, which is presented in Fig. 3.17a–c. The reasoning concerning the less clean AB phase induced modulation of the magnetoconductance is equivalent to the case of QPC-VII. Lastly, Fig. 3.17d shows the gate voltage dependence of the conductance of QPC-VIII with focus on parts of the QSH regime for $B_z = 0\,\mathrm{T}$, for $B_z = 0.069\,\mathrm{T} =: B_0$ and for $B_z = 0.172\,\mathrm{T}$ (B_0 for the case of QPC-I). No anti-phase behaviour is observable.

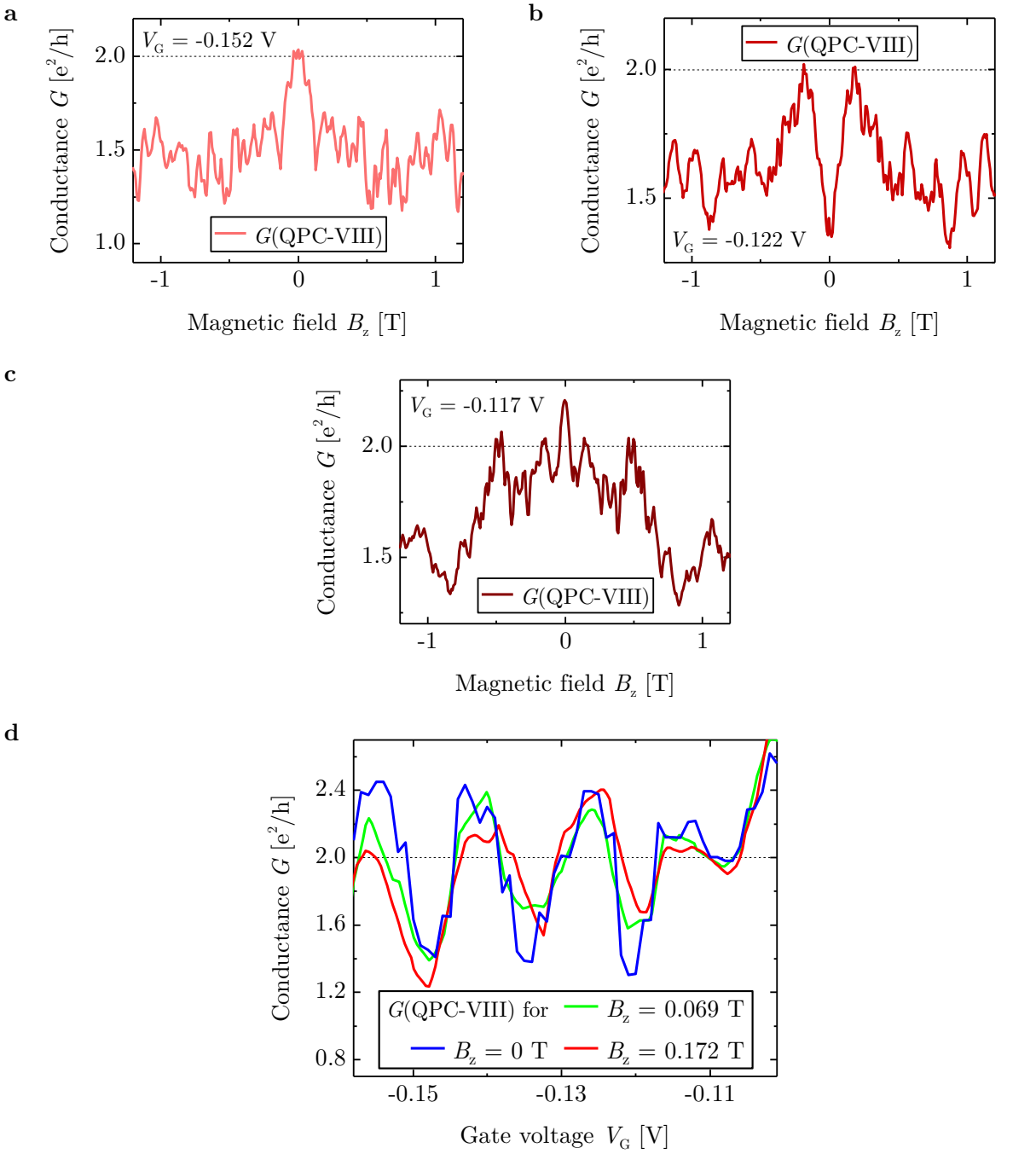

Figure 3.17: **a**–**c**, Magnetoconductance G of QPC-VIII for different values of the gate voltage V_G. **d**, Gate voltage dependence of the conductance G of QPC-VIII with focus on parts of the QSH regime for a magnetic field value of $B_z = 0\,\mathrm{T}$, of $B_z = 0.069\,\mathrm{T} =: B_0$ and of $B_z = 0.172\,\mathrm{T}$ (B_0 for the case of QPC-I). The blue trace is equivalent to the data shown in Fig. 3.16d.

3.6 Conclusion

The realization of a QSH interferometer state in narrow HgTe based QPC devices with a quantum well thickness of $d_{QW} \approx 7\,\mathrm{nm}$ is an experimental novelty not achieved before. The

latter enables the observation of the interplay of the AB phase, of the dynamical AC phase and of a spin-orbit Berry phase of π for the first time – consistent with theoretical expectations for an ideal 1D quantum ring with strong Rashba spin-orbit coupling [13]. Furthermore, the experimental availability of a QSH interferometer state allows for manifold new research possibilities and insights within the field of 2D-TIs.

Since geometric phases are resilient to dephasing, the presence of a spin-orbit Berry phase of π makes the presented QPC devices promising building blocks for various future applications. An utilization of high interest is for example related to the realization of geometric quantum gates within the context of quantum computation [53–55]. Moreover, a device realization anticipated ever since the experimental proof of 2D-TIs is facilitated by the observation of the dynamical AC phase. The latter enables an all-electrically controllable conductance in the QSH regime, thus paving the way to the implementation of a topological transistor. Despite noteworthy progress in realizing such a technology based on electric field induced quantum phase transitions [56, 57], this approach still lacks experimental examination in the context of a fabricated sample – contrary to the case of topological HgTe based QPCs. Optimizing the device concept is expected to result in an oscillation of the QSH conductance within $G \in [0; 2e^2/h]$ [24], thus enabling to switch the QPC from an *on* state to an *off* state and vice versa. Therefore, the presented results provide first evidence in a pure transport framework that topological transistors are attainable.

3.7 Sample overview

QPC No.	d_{QW} [nm]	W_{QPC} [nm]	L_{QPC} [nm]	L_{Gate} [nm]	$n_{\mathrm{e}}(0\,\mathrm{V})$ [cm^{-2}]	$\mu_{\mathrm{e}}(0\,\mathrm{V})$ [$\mathrm{cm}^2\mathrm{V}^{-1}\mathrm{s}^{-1}$]	l_{e} [µm]	Layer thicknesses [nm]
I	7.0	100	500	250	$5.2 \cdot 10^{11}$	$2.7 \cdot 10^5$	3.2	70/9/70/7/50
V	7.0	250	500	250	$4.8 \cdot 10^{11}$	$2.3 \cdot 10^5$	2.6	81/10/81/7/59
VII	7.0	100	500	250	$5.2 \cdot 10^{11}$	$2.7 \cdot 10^5$	3.2	70/9/70/7/50
VIII	7.0	100	1350	600	$5.2 \cdot 10^{11}$	$2.7 \cdot 10^5$	3.2	70/9/70/7/50

Table 3.1: Summary of the sample and material parameters for each discussed QPC device indicated by Roman numerals. The layer thickness values refer to the sketched layer stack shown in Fig. 2.7b. The given numbers (from right to left) are attributed to the sketched layers from top to bottom. The thickness of the buffer as well as of the substrate is not included.

BIBLIOGRAPHY

[1] F. Dolcini, *Full electrical control of charge and spin conductance through interferometry of edge states in topological insulators,* Physical Review B **83**, 165304 (2011).

[2] D. Ferraro, G. Dolcetto, R. Citro, F. Romeo, and M. Sassetti, *Spin current pumping in helical Luttinger liquids,* Physical Review B **87**, 245419 (2013).

[3] G. Dolcetto, M. Sassetti, and T. L. Schmidt, *Edge physics in two-dimensional topological insulators,* Rivista del Nuovo Cimento **39**, 113 (2016).

[4] M. Arndt, O. Nairz, J. Vos-Andreae, C. Keller, G. van der Zouw, and A. Zeilinger, *Wave–particle duality of C_{60} molecules,* Nature **401**, 680 (1999).

[5] T. Ihn, *Semiconductor Nanostructures: Quantum States and Electronic Transport* (Oxford University Press, Oxford, 2010).

[6] R. Feynman, R. Leighton, and M. Sands, *The Feynman Lectures on Physics, Vol. III: The New Millennium Edition: Quantum Mechanics* (Basic Books, New York, 2011).

[7] T. L. Dimitrova and A. Weis, *Single photon quantum erasing: a demonstration experiment,* European Journal of Physics **31**, 625 (2010).

[8] E. Buks, R. Schuster, M. Heiblum, D. Mahalu, and V. Umansky, *Dephasing in electron interference by a 'which-path' detector,* Nature **391**, 871 (1998).

[9] M. König, A. Tschetschetkin, E. M. Hankiewicz, J. Sinova, V. Hock, V. Daumer, M. Schäfer, C. R. Becker, H. Buhmann, and L. W. Molenkamp, *Direct Observation of the Aharonov-Casher Phase,* Physical Review Letters **96**, 076804 (2006).

[10] E. G. Novik, A. Pfeuffer-Jeschke, T. Jungwirth, V. Latussek, C. R. Becker, G. Landwehr, H. Buhmann, and L. W. Molenkamp, *Band structure of semimagnetic* $Hg_{1-y}Mn_yTe$ *quantum wells,* Physical Review B **72**, 035321 (2005).

[11] Y. S. Gui, C. R. Becker, N. Dai, J. Liu, Z. J. Qiu, E. G. Novik, M. Schäfer, X. Z. Shu, J. H. Chu, H. Buhmann, and L. W. Molenkamp, *Giant spin-orbit splitting in a* HgTe *quantum well,* Physical Review B **70**, 115328 (2004).

[12] J. Hinz, H. Buhmann, M. Schäfer, V. Hock, C. R. Becker, and L. W. Molenkamp, *Gate control of the giant Rashba effect in HgTe quantum wells,* Semiconductor Science and Technology **21**, 501 (2006).

[13] K. Richter, *The ABC of Aharonov effects,* Physics **5**, 22 (2012).

[14] Y. Aharonov and D. Bohm, *Significance of Electromagnetic Potentials in the Quantum Theory,* Physical Review **115**, 485 (1959).

[15] R. A. Webb, S. Washburn, C. P. Umbach, and R. B. Laibowitz, *Observation of $\frac{h}{e}$ Aharonov-Bohm Oscillations in Normal-Metal Rings,* Physical Review Letters **54**, 2696 (1985).

[16] G. Timp, A. M. Chang, J. E. Cunningham, T. Y. Chang, P. Mankiewich, R. Behringer, and R. E. Howard, *Observation of the Aharonov-Bohm effect for $\omega_c\tau > 1$,* Physical Review Letters **58**, 2814 (1987).

[17] K. Ishibashi, Y. Takagaki, K. Gamo, S. Namba, S. Ishida, K. Murase, Y. Aoyagi, and M. Kawabe, *Observation of Aharonov-Bohm magnetoresistance oscillations in selectively doped GaAs-AlGaAs submicron structures,* Solid State Communications **64**, 573 (1987).

[18] C. J. B. Ford, T. J. Thornton, R. Newbury, M. Pepper, H. Ahmed, C. T. Foxon, J. J. Harris, and C. Roberts, *The Aharonov-Bohm effect in electrostatically defined heterojunction rings,* Journal of Physics C: Solid State Physics **21**, L325 (1988).

[19] Y. Aharonov and A. Casher, *Topological Quantum Effects for Neutral Particles,* Physical Review Letters **53**, 319 (1984).

[20] J. Nitta, F. E. Meijer, and H. Takayanagi, *Spin-interference device,* Applied Physics Letters **75**, 695 (1999).

[21] D. Frustaglia and K. Richter, *Spin interference effects in ring conductors subject to Rashba coupling,* Physical Review B **69**, 235310 (2004).

[22] B. Molnár, F. M. Peeters, and P. Vasilopoulos, *Spin-dependent magnetotransport through a ring due to spin-orbit interaction,* Physical Review B **69**, 155335 (2004).

[23] F. Nagasawa, J. Takagi, Y. Kunihashi, M. Kohda, and J. Nitta, *Experimental Demonstration of Spin Geometric Phase: Radius Dependence of Time-Reversal Aharonov-Casher Oscillations,* Physical Review Letters **108**, 086801 (2012).

[24] J. Nitta and T. Bergsten, *Time reversal Aharonov–Casher effect using Rashba spin–orbit interaction,* New Journal of Physics **9**, 341 (2007).

[25] T. Bergsten, T. Kobayashi, Y. Sekine, and J. Nitta, *Experimental Demonstration of the Time Reversal Aharonov-Casher Effect,* Physical Review Letters **97**, 196803 (2006).

[26] F. Qu, F. Yang, J. Chen, J. Shen, Y. Ding, J. Lu, Y. Song, H. Yang, G. Liu, J. Fan, Y. Li, Z. Ji, C. Yang, and L. Lu, *Aharonov-Casher Effect in Bi_2Se_3 Square-Ring Interferometers,* Physical Review Letters **107**, 016802 (2011).

[27] F. Nagasawa, D. Frustaglia, H. Saarikoski, K. Richter, and J. Nitta, *Control of the spin geometric phase in semiconductor quantum rings,* Nature Communications **4**, 2526 (2013).

[28] J. I. Väyrynen and T. Ojanen, *Electrical Manipulation and Measurement of Spin Properties of Quantum Spin Hall Edge States,* Physical Review Letters **106**, 076803 (2011).

[29] T.-Z. Qian and Z.-B. Su, *Spin-orbit interaction and Aharonov-Anandan phase in mesoscopic rings,* Physical Review Letters **72**, 2311 (1994).

[30] A. Carollo, I. Fuentes-Guridi, M. Santos França, and V. Vedral, *Geometric Phase in Open Systems,* Physical Review Letters **90**, 160402 (2003).

[31] S. Filipp, J. Klepp, Y. Hasegawa, C. Plonka-Spehr, U. Schmidt, P. Geltenbort, and H. Rauch, *Experimental Demonstration of the Stability of Berry's Phase for a Spin-1/2 Particle,* Physical Review Letters **102**, 030404 (2009).

[32] M. V. Berry, *Quantal phase factors accompanying adiabatic changes,* Proceedings of the Royal Society of London. A. Mathematical and Physical Sciences **392**, 45 (1984).

[33] Y. Aharonov and J. Anandan, *Phase change during a cyclic quantum evolution,* Physical Review Letters **58**, 1593 (1987).

[34] A. G. Aronov and Y. B. Lyanda-Geller, *Spin-orbit Berry phase in conducting rings,* Physical Review Letters **70**, 343 (1993).

[35] D. Loss, P. Goldbart, and A. V. Balatsky, *Berry's phase and persistent charge and spin currents in textured mesoscopic rings,* Physical Review Letters **65**, 1655 (1990).

[36] D. Loss and P. M. Goldbart, *Persistent currents from Berry's phase in mesoscopic systems,* Physical Review B **45**, 13544 (1992).

[37] A. Stern, *Berry's phase, motive forces, and mesoscopic conductivity,* Physical Review Letters **68**, 1022 (1992).

[38] D. G. Rothe and E. M. Hankiewicz, *Tunable polarization in a beam splitter based on two-dimensional topological insulators,* Physical Review B **89**, 035418 (2014).

[39] L. Ortiz, R. A. Molina, G. Platero, and A. M. Lunde, *Generic helical edge states due to Rashba spin-orbit coupling in a topological insulator,* Physical Review B **93**, 205431 (2016).

[40] H. Peng, K. Lai, D. Kong, S. Meister, Y. Chen, X.-L. Qi, S.-C. Zhang, Z.-X. Shen, and Y. Cui, *Aharonov–Bohm interference in topological insulator nanoribbons,* Nature Materials **9**, 225 (2010).

[41] L. A. Jauregui, M. T. Pettes, L. P. Rokhinson, L. Shi, and Y. P. Chen, *Magnetic field-induced helical mode and topological transitions in a topological insulator nanoribbon,* Nature Nanotechnology **11**, 345 (2016).

[42] J. Maciejko, X.-L. Qi, and S.-C. Zhang, *Magnetoconductance of the quantum spin Hall state,* Physical Review B **82**, 155310 (2010).

[43] G. Tkachov and E. M. Hankiewicz, *Ballistic Quantum Spin Hall State and Enhanced Edge Backscattering in Strong Magnetic Fields,* Physical Review Letters **104**, 166803 (2010).

[44] P. Delplace, J. Li, and M. Büttiker, *Magnetic-Field-Induced Localization in 2D Topological Insulators,* Physical Review Letters **109**, 246803 (2012).

[45] W. Chen, W.-Y. Deng, J.-M. Hou, D. N. Shi, L. Sheng, and D. Y. Xing, *π Spin Berry Phase in a Quantum-Spin-Hall-Insulator-Based Interferometer: Evidence for the Helical Spin Texture of the Edge States,* Physical Review Letters **117**, 076802 (2016).

[46] V. Adak, K. Roychowdhury, and S. Das, *Spin Berry phase in a helical edge state: S_z nonconservation and transport signatures,* Physical Review B **102**, 035423 (2020).

[47] M. Wang, H. Saarikoski, A. A. Reynoso, J. P. Baltanás, D. Frustaglia, and J. Nitta, *Geometry-Assisted Topological Transitions in Spin Interferometry,* Physical Review Letters **123**, 266804 (2019).

[48] B. Büttner, C. X. Liu, G. Tkachov, E. G. Novik, C. Brüne, H. Buhmann, E. M. Hankiewicz, P. Recher, B. Trauzettel, S. C. Zhang, and L. W. Molenkamp, *Single valley Dirac fermions in zero-gap HgTe quantum wells,* Nature Physics **7**, 418 (2011).

[49] Y. Imry, *Active Transmission Channels and Universal Conductance Fluctuations,* Europhysics Letters **1**, 249 (1986).

[50] W. J. Skocpol, P. M. Mankiewich, R. E. Howard, L. D. Jackel, D. M. Tennant, and A. D. Stone, *Universal conductance fluctuations in silicon inversion-layer nanostructures,* Physical Review Letters **56**, 2865 (1986).

[51] V. Krueckl and K. Richter, *Probing the band topology of mercury telluride through weak localization and antilocalization,* Semiconductor Science and Technology **27**, 124006 (2012).

[52] Z.-J. Ying, P. Gentile, C. Ortix, and M. Cuoco, *Designing electron spin textures and spin interferometers by shape deformations,* Physical Review B **94**, 081406 (2016).

[53] J. A. Jones, V. Vedral, A. Ekert, and G. Castagnoli, *Geometric quantum computation using nuclear magnetic resonance,* Nature **403**, 869 (2000).

[54] G. Falci, R. Fazio, G. M. Palma, J. Siewert, and V. Vedral, *Detection of geometric phases in superconducting nanocircuits,* Nature **407**, 355 (2000).

[55] E. Sjöqvist, *A new phase in quantum computation,* Physics **1**, 35 (2008).

[56] X. Qian, J. Liu, L. Fu, and J. Li, *Quantum spin Hall effect in two-dimensional transition metal dichalcogenides,* Science **346**, 1344 (2014).

[57] J. L. Collins, A. Tadich, W. Wu, L. C. Gomes, J. N. B. Rodrigues, C. Liu, J. Hellerstedt, H. Ryu, S. Tang, S.-K. Mo, S. Adam, S. A. Yang, M. S. Fuhrer, and M. T. Edmonds, *Electric-field-tuned topological phase transition in ultrathin Na_3Bi,* Nature **564**, 390 (2018).

4

Emergence of an anomalous topological conductance plateau for quantum point contacts based on thick HgTe quantum wells

This chapter is based on the publication:
INTERACTING TOPOLOGICAL EDGE CHANNELS.
Jonas Strunz, Jonas Wiedenmann, Christoph Fleckenstein, Lukas Lunczer, Wouter Beugeling, Valentin L. Müller, Pragya Shekhar, Niccolò Traverso Ziani, Saquib Shamim, Johannes Kleinlein, Hartmut Buhmann, Björn Trauzettel and Laurens W. Molenkamp. *Nature Physics* **16**, 83 (2020).

In this chapter, the conductance pattern of quantum point contacts based on HgTe quantum wells with a thickness of $d_{\mathrm{QW}} = 10.5\,\mathrm{nm}$ *is discussed. For these devices – apart from the expected conductance quantization within the bulk band gap of* $G_{\mathrm{QSH}} \approx 2e^2/h$ *– an additional plateau emerges at* $G \approx e^2/h = 0.5 \cdot G_{\mathrm{QSH}}$*, which is referred to as* 0.5 *anomaly. The appearance of the latter is examined for different device widths and it is observed that the* 0.5 *anomaly occurs only for a specific interval of width values. Subsequently presented temperature and bias voltage dependent measurements of the* 0.5 *anomaly provide evidence that the signature is related to a gapped topological state. Moreover, by analysing a multi-terminal quantum point contact device, it is demonstrated that the regime of the* 0.5 *anomaly is further linked to a backscattered helical edge channel. In order to explain the emergence of the* 0.5 *anomaly, two theoretic models are presented, which both are based on electron-electron interaction effects as an essential ingredient. While the first approach relies on considerations stemming from the Tomonaga-Luttinger liquid theory, the second model covers a helical edge reconstruction mechanism.*

4.1 The 0.5 anomaly and its relation to quantum well thickness

For ballistic transport experiments, the elastic mean free path l_e represents the critical sample parameter. It is known that for the case of HgTe quantum wells, the mean free path – and thus the electron mobility μ_e – is correlated with the quantum well thickness d_{QW}. Hence, the fabrication and examination of QPC devices based on thicker inverted HgTe quantum wells appears self-evident, since the latter are expected to offer superior transport parameters. However, the increase in quantum well thickness entails modifications to the energetic order of subbands within the HgTe quantum well (see Fig. 2.3).

4.1.1 Band structure of inverted HgTe quantum wells beyond the Bernevig-Hughes-Zhang case

While the so far discussed topological QPC devices are based on quantum wells with $d_{QW} = 7\,\text{nm}$, the focus shifts now to QPC samples fabricated from quantum wells with a thickness of $d_{QW} = 10.5\,\text{nm}$ (see Fig. 4.1a). Figure 4.1b shows the band structure calculations for the two quantum well thicknesses, which are performed using $\mathbf{k} \cdot \mathbf{p}$ theory based on the eight-band Kane model [1]. For both cases, the calculated bulk band structure of an infinitely wide slab of quantum well material is represented by the solid black lines. A second calculation using a semi-finite ribbon with a width of $W_y = 150\,\text{nm}$ provides information about the energetic ordering and the spatial extension of topological and trivial states within the QPC (coloured dots in Fig. 4.1b).

The band structure of the $d_{QW} = 7\,\text{nm}$ case is presented in the left panel of Fig. 4.1b. It exhibits an inverted band ordering, where the H_1 subband forms the conduction band and the E_1 subband forms the valence band. It is important to note that the Dirac point lies energetically within the bulk band gap, which is qualitatively consistent with the BHZ model.

The right panel of Fig. 4.1b shows the band structure for the $d_{QW} = 10.5\,\text{nm}$ case. There, the band gap is present between the first two heavy hole type subbands H_1 and H_2. Thus, the H_1 subband forms the conduction band and the H_2 subband determines the valence band edge. The E_1 subband – which is still responsible for the band inversion – lies energetically below the H_2 subband. Consequently, the Dirac point is buried deeply in the valence band. Moreover, it should be stressed that the H_2 valence band exhibits maxima at finite momenta and not at $k = 0$, which makes the band gap indirect. The latter feature is a consequence of the band inversion combined with hybridization effects between the subbands and is referred to as *camel back* [2, 3].

4.1.2 Observation of the 0.5 anomaly

The gate voltage V_G dependence of the conductance G of QPC-IX is presented in Fig. 4.2 – an exemplary QPC device fabricated from a quantum well with $d_{QW} = 10.5\,\text{nm}$. The conductance can be divided into three separate regimes. The trivial regime (n-n'-n regime) shows

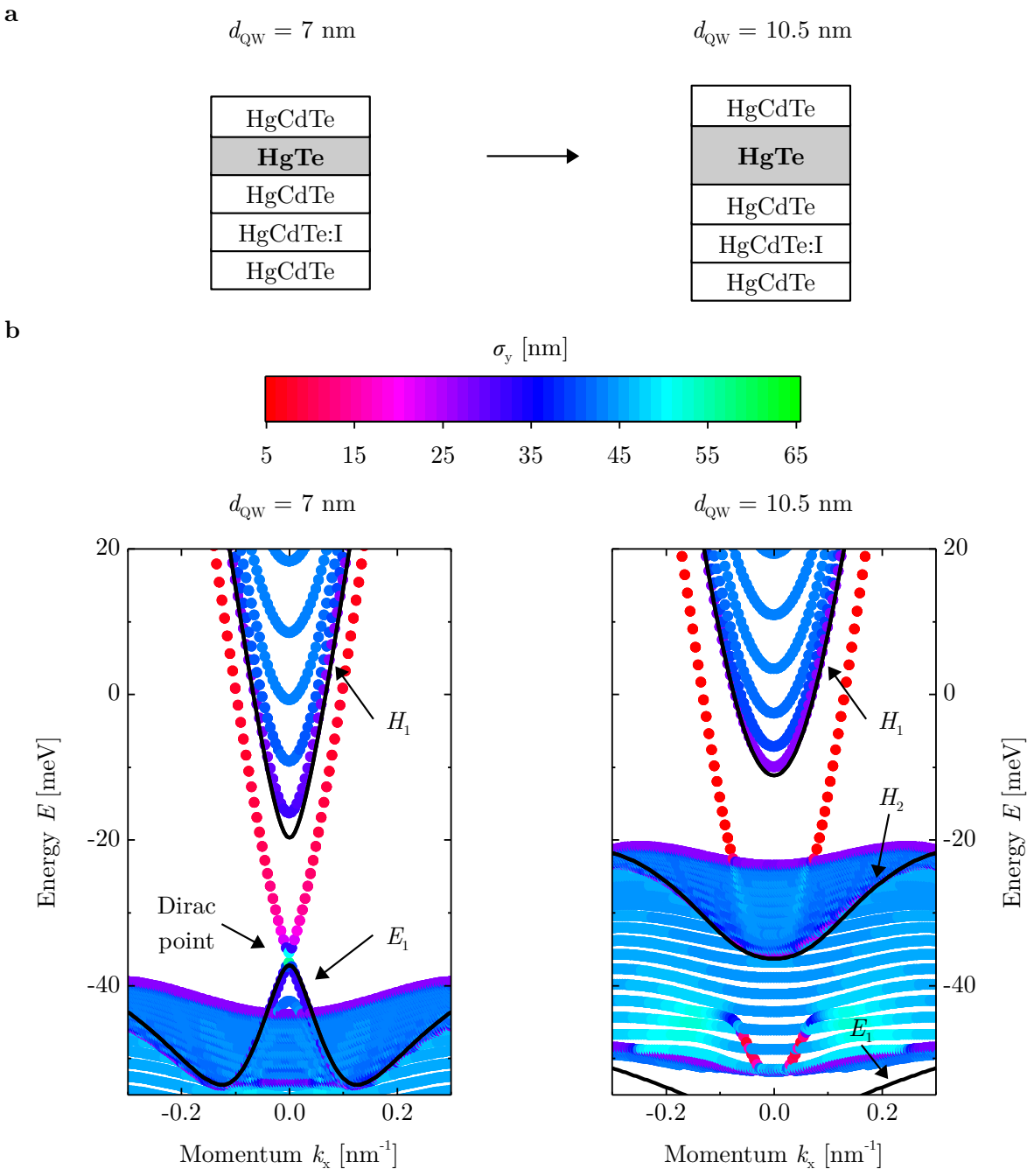

Figure 4.1: **a**, Sketch of the increase of the quantum well thickness d_{QW} from $d_{QW} = 7\,nm$ to $d_{QW} = 10.5\,nm$. **b**, $\mathbf{k} \cdot \mathbf{p}$ band structure calculations for a semi-finite ribbon with a width of $W_y = 150\,nm$ and $d_{QW} = 7\,nm$ (left panel) and $d_{QW} = 10.5\,nm$ (right panel), respectively. The colour code indicates the standard deviation σ_y of the wave function in y direction. The solid black lines represent the bulk band structure.

distinct plateaus up to $G \approx 14e^2/h$ due to trivial ballistic 1D transport. The application of a low magnetic field $B_z = 0.3\,T$ (red trace) is equivalent to subtracting a small serial resistance [4].

The subsequent topological regime is classified into two sub-regimes. First, the conductance saturates around a long plateau at $G_{QSH} \approx 2e^2/h$, which is attributed to the QSH regime (n-i-n

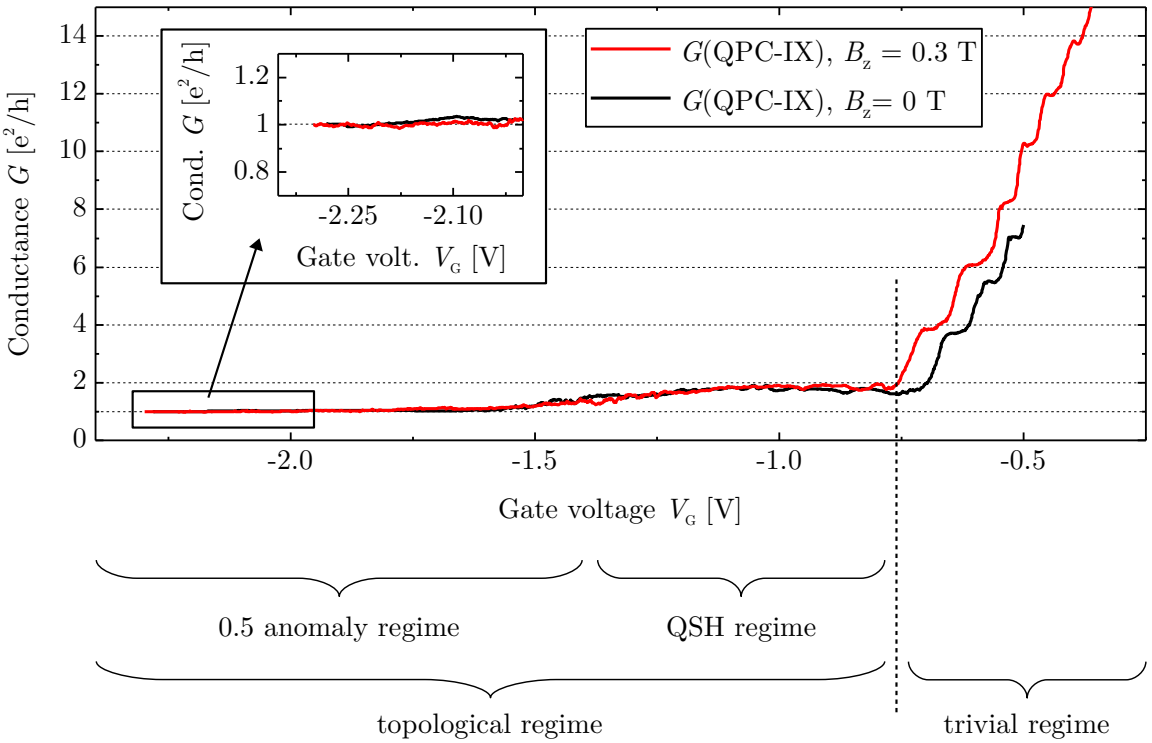

Figure 4.2: Gate voltage V_G dependence of the conductance G of QPC-IX ($d_{QW} = 10.5$ nm), which can be divided into three regimes. The trivial regime (n-n'-n regime) exhibits conductance plateaus up to $G \approx 14e^2/h$ and the QSH regime (n-i-n regime of a topological QPC device) reveals itself by a conductance of $G_{QSH} \approx 2e^2/h$. With entering the 0.5 anomaly regime, the conductance drops to a quantized value of $G \approx e^2/h = 0.5 \cdot 2e^2/h$. Together, the QSH regime and the 0.5 anomaly regime form the topological regime. The inset shows an enlarged view of the 0.5 anomaly regime.

regime of a topological QPC device). However, with tuning the gate voltage successively towards more negative values, no signatures of the n-p-n regime (and thus of an increase in conductance) can be identified within the data shown in Fig. 4.2 – contrary to QPC devices fabricated from quantum wells with $d_{QW} = 7$ nm. Instead, a step-like transition from $G_{QSH} \approx 2e^2/h$ to an even longer plateau at $G \approx e^2/h = 0.5 \cdot G_{QSH}$ occurs. This peculiar phenomenon is labelled as 0.5 anomaly, the corresponding transport regime is referred to as 0.5 anomaly regime.

The inset of Fig. 4.2 demonstrates the precision of the 0.5 anomaly as well as its resilience towards a magnetic field of $B_z \lessapprox 0.3$ T. Due to reasons of consistency, the presentation of conductance data is maintained in units of e^2/h. Thus, the conductance plateau attributed to the 0.5 anomaly appears at $1 \cdot e^2/h$.

Further remarks

A second measurement of the n-n'-n regime of QPC-IX is shown in Fig. 4.3a. With applying a magnetic field of $B_z = 0.3$ T, conductance quantization up to $G \approx 22e^2/h$ is observable. This level of quantization has not been realizable for quantum wells with $d_{QW} = 7$ nm within the scope of this thesis. Thus, this result indicates the superior quality of QPC devices based on quantum wells with $d_{QW} = 10.5$ nm in terms of trivial ballistic 1D transport.

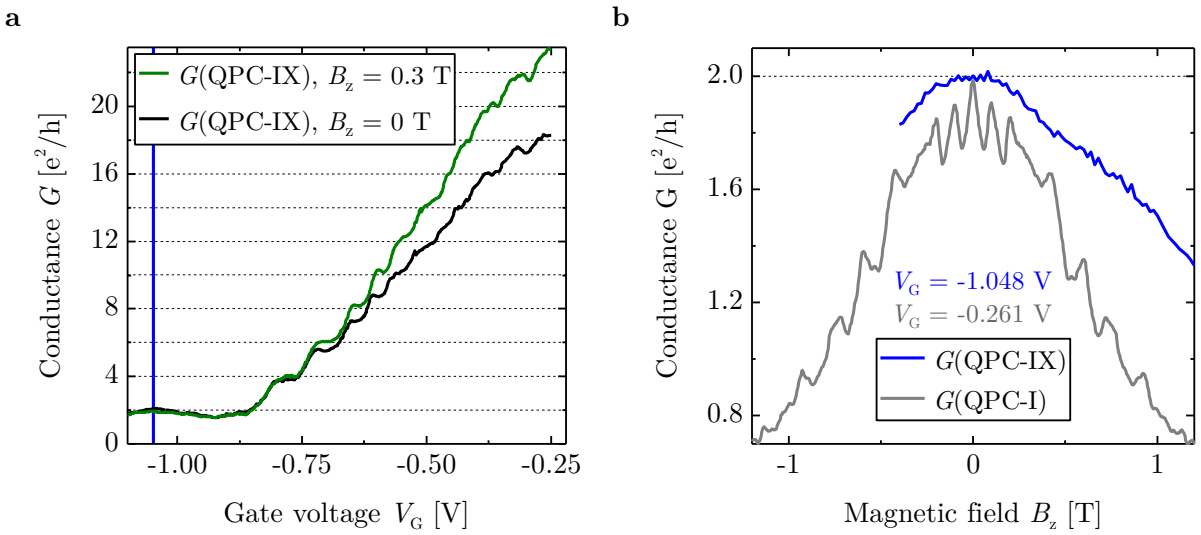

Figure 4.3: **a**, Gate voltage V_G dependence of the conductance G of QPC-IX for $B_z = 0\,T$ and $B_z = 0.3\,T$. The vertical blue line highlights the gate voltage value of the data shown in panel **b**. The data of panel **a** was acquired performing another measurement in addition to the data shown in Fig. 4.2. The shift of the conductance traces with regard to the applied gate voltage between both measurements is due to thermal cycling. **b**, Magnetoconductance G of QPC-IX ($d_{QW} = 10.5\,nm$, blue trace) measured within the QSH regime. The data of QPC-I ($d_{QW} = 7\,nm$, grey trace) is added for comparison purposes and is equivalent to the data presented in Fig. 3.6a.

In Fig. 4.3b, an exemplary measurement of the magnetoconductance G obtained within the QSH regime of QPC-IX is compared with data of QPC-I (equivalent to the data of Fig. 3.6a). No distinct periodic oscillation pattern is observable for the case of QPC-IX, which is consistent with the expectations of the proposed QSH ring formation model in Section 3.1.2. Inserting $W_{QPC} \approx 150\,nm$, $\lambda_F \approx 33\,nm$ (based on the electron density of the wafer material utilized for the fabrication of device QPC-IX, see Tab. 4.1) and $\sigma_y \approx 10\,nm$ (see Fig. 4.1b) into Eq. 3.2 yields $(2 \cdot 10 + 33)\,nm < 150\,nm$, thus no formation of a QSH interferometer state is expected.

4.2 Characterization of the 0.5 anomaly regime

In order to extend the study of the 0.5 anomaly, its dependence on the device width W_{QPC}, on the temperature T and on an applied DC bias voltage V_{DC} will be analysed in the following. Subsequently, the emergence of the 0.5 anomaly is discussed from a single particle picture perspective. These considerations also include implications caused by the peculiar band structure of HgTe quantum wells with $d_{QW} = 10.5\,nm$, i.e. the emergence of the camel back. Moreover, the lithographic fabrication process as well as transport measurements of a novel multi-terminal QPC device are presented. The acquired data demonstrates that the occurrence of the 0.5 anomaly is accompanied by a backscattered QSH edge channel.

4.2.1 Dependence on device width

An overview of the gate voltage dependence of the conductance of various QPC samples with different width values is presented in Fig. 4.4. The 0.5 anomaly can be identified

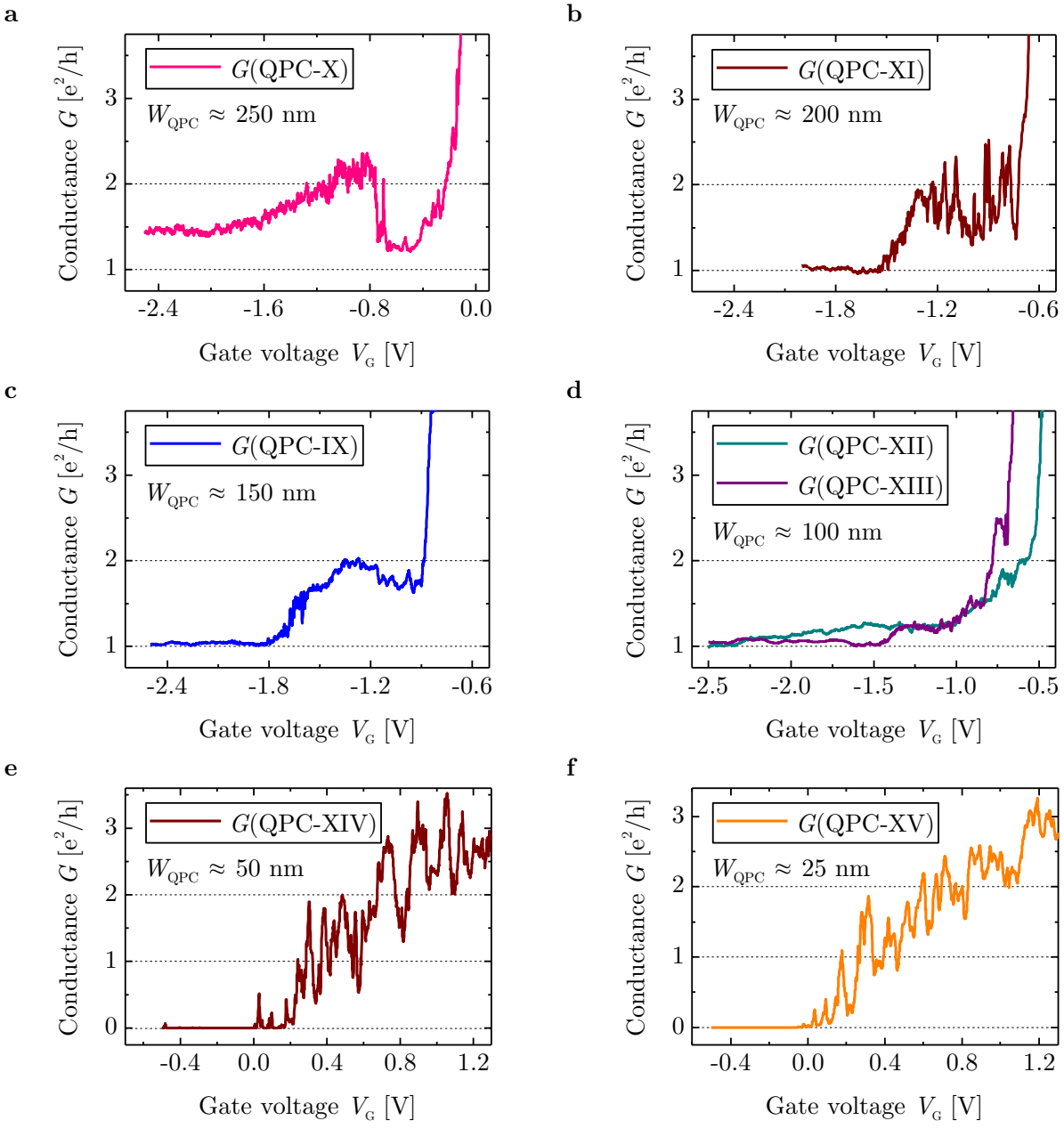

Figure 4.4: **a**–**f**, Width dependence of the 0.5 anomaly regime. In detail, the individual panels show the data for QPC-X (**a**, $W_{\mathrm{QPC}} \approx 250\,\mathrm{nm}$), QPC-XI (**b**, $W_{\mathrm{QPC}} \approx 200\,\mathrm{nm}$), QPC-IX (**c**, $W_{\mathrm{QPC}} \approx 150\,\mathrm{nm}$), QPC-XII and QPC-XIII (**d**, both $W_{\mathrm{QPC}} \approx 100\,\mathrm{nm}$), QPC-XIV (**e**, $W_{\mathrm{QPC}} \approx 50\,\mathrm{nm}$) and QPC-XV (**f**, $W_{\mathrm{QPC}} \approx 25\,\mathrm{nm}$). For the case of QPC-IX, the blue trace in panel **c** was acquired performing another measurement in addition to the data shown in Fig. 4.2. The shift of the conductance G with regard to the applied gate voltage V_{G} between both measurements is due to thermal cycling.

for the devices QPC-IX, QPC-XI, QPC-XII and QPC-XIII (Fig. 4.4b–d), which exhibit device width values of $W_{\mathrm{QPC}} \in [100; 200]\,\mathrm{nm}$. For devices with larger width values such as QPC-X ($W_{\mathrm{QPC}} \approx 250\,\mathrm{nm}$, see Fig. 4.4a), the conductance still drops below $G_{\mathrm{QSH}} \approx 2e^2/h$, but does not reach the value $G \approx 0.5 \cdot G_{\mathrm{QSH}}$ anymore. This observation suggests that an interaction mechanism

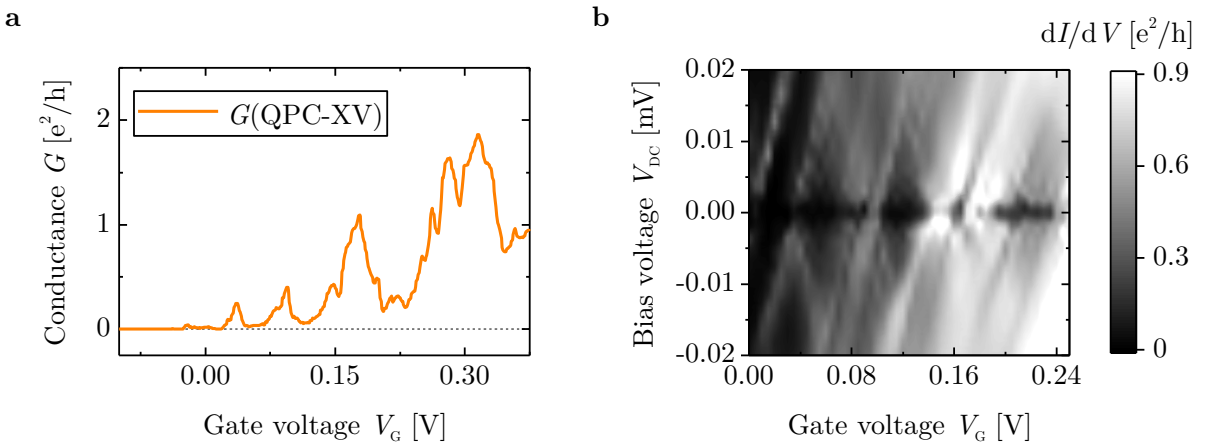

Figure 4.5: **a**, Zoom on the gate voltage V_G dependence of the conductance G of QPC-XV with focus on the entrance to the n-n'-n regime. **b**, Combined gate voltage and bias voltage V_{DC} dependence of the differential conductance dI/dV of QPC-XV.

between the helical edge channels is crucial for the appearance of the 0.5 anomaly. For the case of QPC-XII and QPC-XIII ($W_{QPC} \approx 100\,nm$), no distinct plateau emerges at $G_{QSH} \approx 2e^2/h$ any longer. However, the plateau at $G \approx 0.5 \cdot G_{QSH}$ is still observable. In the context of an interaction driven mechanism responsible for the emergence of the 0.5 anomaly, this behaviour can be attributed to stronger inter-edge interactions in narrower QPC devices.

For all QPC devices exhibiting the 0.5 anomaly, the signature appears at large negative gate voltage values and persists over a wide voltage range. The gate efficiency of the examined devices is known from measurements of reference Hall bar samples with an analogue gate stack to be approximately $\Delta n_e/\Delta V_G \approx 8\text{–}10 \cdot 10^{11}\,cm^{-2}V^{-1}$. Hence, it appears reasonable to conclude that the bulk density in the 0.5 anomaly regime is strongly p-doped with a roughly estimated hole density of $n_h > 1 \cdot 10^{12}\,cm^{-2}$. However, bulk transport through the QPC is suppressed in the 0.5 anomaly regime, which will be discussed in Section 4.2.3.

For very narrow QPC devices such as QPC-XIV ($W_{QPC} \approx 50\,nm$, Fig. 4.4e) and QPC-XV ($W_{QPC} \approx 25\,nm$, Fig. 4.4f), the conductance drops to $G \approx 0$ within the bulk band gap and neither a plateau at $G_{QSH} \approx 2e^2/h$ nor at $G \approx 0.5 \cdot G_{QSH}$ is observable. This absence of topological transport within the bulk band gap is attributed to hybridization effects between the helical edge channels.

In the case of QPC-XV ($W_{QPC} \approx 25\,nm$), the gate voltage dependence of the conductance exhibits signatures which resemble Coulomb blockade oscillations typical for quantum dots (see Fig. 4.5a). This assignment is confirmed by measurements of the combined gate and bias voltage dependence of the differential conductance dI/dV of QPC-XV, which is presented in Fig. 4.5b. The grey scale plot shows diamond shaped structures known from the Coulomb blockade transport regime (see for example Ref. [5]). Hence, the Coulomb blockade diamonds indicate the presence of quasi-zero-dimensional states and thus the formation of electron islands within the gated QPC area.

4.2.2 Dependence on temperature and bias voltage

The temperature dependence of the 0.5 anomaly is presented in Fig. 4.6a for the case of QPC-IX. Up to $T = 1.4\,\mathrm{K}$ (see also Fig. 4.2 and Fig. 4.4), a pronounced step-like transition from $G_{\mathrm{QSH}} \approx 2e^2/h$ to $G \approx e^2/h$ is observable. For higher values of the temperature ($T \geq 4\,\mathrm{K}$), this transition becomes less distinct. Furthermore, the 0.5 anomaly characteristic quantization of $G \approx e^2/h$ is lost and the lowest value of the topological conductance beyond the QSH regime increases with rising temperatures ($G \approx 1.1e^2/h$ at $T = 4\,\mathrm{K}$). With choosing the range of $T \approx 2$–$4\,\mathrm{K}$ as the upper temperature limit up to which the 0.5 anomaly is still observable, a corresponding energy scale of $\Delta E = k_{\mathrm{B}}T \approx 150$–$300\,\mu\mathrm{eV}$ can be defined.

This energy scale is in agreement with the results of the bias voltage dependence of the 0.5 anomaly, which is presented in Fig. 4.6b–e for the case of QPC-XIII. The 0.5 anomaly is observable up to bias voltage values of $V_{\mathrm{DC}} \approx 200$–$400\,\mu\mathrm{V}$ (see Fig. 4.6d), which results in an energy scale of $\Delta E = eV_{\mathrm{DC}} \approx 200$–$400\,\mu\mathrm{eV}$. The consistency of the energy scale values among several devices and different estimation methods substantiates the robust, stable and reproducible character of the 0.5 anomaly.

With increasing the bias voltage further, the differential conductance increases as well until it starts to saturate at $\mathrm{d}I/\mathrm{d}V \approx 2e^2/h$ for $V_{\mathrm{DC}} > 13\,\mathrm{meV}$ (see Fig. 4.6c). This saturation indicates that both edge channels are transmitted through the QPC without perturbation over a large range of gate voltage when a sufficiently high bias voltage is applied (see also Fig. 4.6e). Hence, this observation suggests that the occurrence of the 0.5 anomaly is related to the emergence of a gap within the helical spectrum – caused by interactions in devices with an appropriate width W_{QPC}.

A further interesting feature of the bias voltage dependence of the differential conductance is highlighted by the arrow in Fig. 4.6c. The latter points to the formation of a plateau-like shape around $\mathrm{d}I/\mathrm{d}V \approx 0.8 \cdot 2e^2/h$. Depending on the device, it is sometimes also possible to identify such a feature as a function of gate voltage (see for example Fig. 4.4c).

It is conjectured that this feature is related to the 0.7 anomaly commonly observed in conventional QPC devices [6]. Following the argumentation of Ref. [7], the 0.7 anomaly emerges due to a broadened density of states at the bottom of the first trivial subband in combination with enhanced electron-electron interactions. As a consequence, a small negative conductance correction occurs, which forms a shoulder-like signature around $G \approx 0.7 \cdot 2e^2/h$ – referred to as 0.7 anomaly. Adapted to the present case, the feature at $\mathrm{d}I/\mathrm{d}V \approx 0.8 \cdot 2e^2/h$ appears when the applied bias voltage becomes large enough to touch the lower edge of the interaction induced gap.

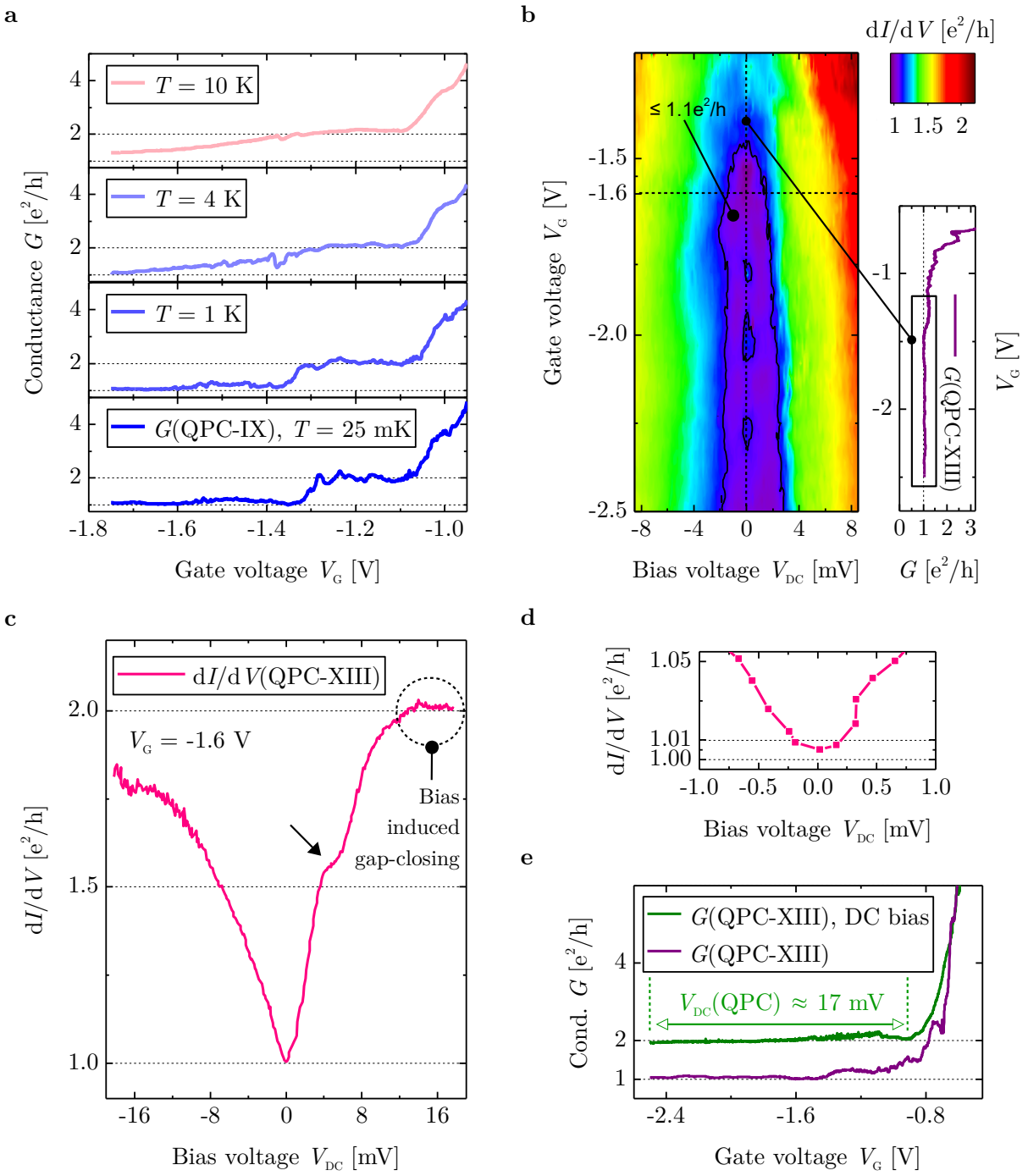

Figure 4.6: **a**, Gate voltage V_G dependence of the conductance G of QPC-IX with focus on the transition from $G_\mathrm{QSH} \approx 2e^2/h$ to $G \approx e^2/h$ for different values of the temperature. **b**, Combined gate voltage and bias voltage V_DC dependence of the differential conductance $\mathrm{d}I/\mathrm{d}V$ of QPC-XIII. The violet area indicates the regime of the 0.5 anomaly. **c**, Line cut of the bias voltage dependence of the differential conductance of QPC-XIII presented in panel **b** for $V_\mathrm{G} = -1.6\,\mathrm{V}$. The arrow indicates the formation of a plateau-like shape around $\mathrm{d}I/\mathrm{d}V \approx 0.8 \cdot 2e^2/h$. The asymmetry of the bias voltage dependence can be attributed to self-gating effects. **d**, Zoom on the low bias voltage regime of panel **c**. **e**, Gate voltage dependence of the conductance of QPC-XIII for no applied bias voltage (violet) and a large applied bias voltage (green). The latter causes a voltage drop of $V_\mathrm{DC} \approx 17\,\mathrm{mV}$ across the sample when the device is in the QSH regime.

4.2.3 Discussion from a single particle picture perspective including band structure considerations

The peculiar band structure of quantum wells with $d_{\mathrm{QW}} = 10.5\,\mathrm{nm}$ is demonstrably crucial for the emergence of the 0.5 anomaly. While the exact physical origin of the latter is still unclear, the so far discussed experimental observations point towards an interaction mechanism between the helical edge states, which opens up a gap in the helical spectrum. In the following, it will be explicated that the burying of the Dirac point and the formation of the camel back have several implications for charge transport and that they are causative for different aspects in the context of observing the 0.5 anomaly.

Figure 4.7a shows a self-consistent $\mathbf{k} \cdot \mathbf{p}$ band structure calculation for a semi-finite ribbon with $W_{\mathrm{y}} = 150\,\mathrm{nm}$ and $d_{\mathrm{QW}} = 10.5\,\mathrm{nm}$, which enables the inclusion of an applied electric field and thus to mimic the influence of the high gate voltages accompanying the 0.5 anomaly regime. By lowering the gate voltage, the Fermi level (indicated by the dashed black line) is pushed into the H_2 bulk subbands. There, the valence band structure exhibits the camel back and the Fermi level gets pinned at the flat valence band edge (high density of states). This circumstance is indicated by the Roman numeral I in Fig. 4.7a. Furthermore, the separation in momentum space between the helical edge states and the bulk states allows for their coexistence without hybridization effects (numeral II). In addition, the large Fermi momentum mismatch between valence and conduction bands suppresses inter-band transitions and hence also suppresses bulk transport in the n-p-n regime (numeral III). These arguments explain the pronounced range in gate voltage of the QSH plateau at $G_{\mathrm{QSH}} \approx 2e^2/h$ as well as the suppression of bulk conductance when entering the valence band. In order to illustrate this behaviour, Fig. 4.7b compares the gate voltage dependence of the conductance of QPC-IX ($d_{\mathrm{QW}} = 10.5\,\mathrm{nm}$) with a wide range gate voltage dependence of the conductance of QPC-I ($d_{\mathrm{QW}} = 7\,\mathrm{nm}$).

The influence of the electric field becomes manifest in the Rashba splitting of the bulk bands, while the dispersion of the helical edge states remains unaffected (see Fig. 4.7a). Nevertheless, the influence of Rashba spin-orbit coupling does induce an energy dependence of the spin-momentum locking within the helical edge states [8, 9], which is indicated by the tilted black arrows (numeral IV). However, the emergence of a gapless generic helical spectrum as well as the previous single particle picture based arguments still cannot explain the occurrence of the 0.5 anomaly.

In the context of discussing the implications of the band structure on transport, a further observation of interest is presented in Fig. 4.7c. There, the gate voltage dependence of the conductance of QPC-IX ($W_{\mathrm{QPC}} \approx 150\,\mathrm{nm}$) and of QPC-XV ($W_{\mathrm{QPC}} \approx 25\,\mathrm{nm}$) is shown for wider ranges of the gate voltage. To ensure comparability between the two devices, both traces are shifted with regard to the gate voltage axis.

For QPC-XV, the conductance drops to $G \approx 0$ caused by hybridization effects of the QSH edge channels. Due to the impact of the camel back, the state of zero conductance (n-i-n regime) persists for a pronounced range of gate voltage. As shown in Fig. 4.7c, this very range is comparable with the total topological regime of QPC-IX, which consists of the QSH regime and the 0.5 anomaly

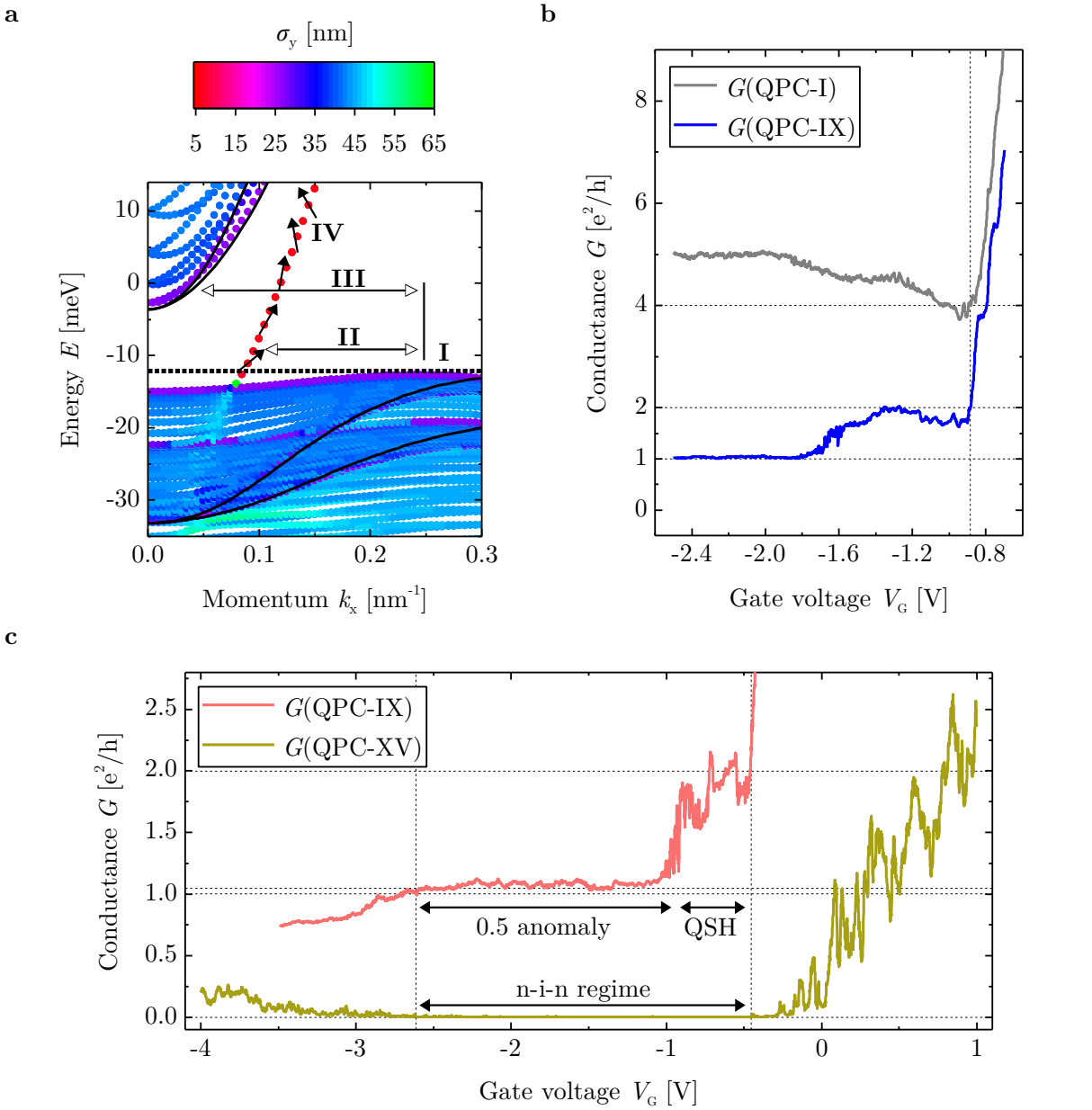

Figure 4.7: **a**, $\mathbf{k}\cdot\mathbf{p}$ band structure calculation for a semi-finite ribbon with $W_y = 150\,\text{nm}$ and and $d_{QW} = 10.5\,\text{nm}$. The colour code indicates the standard deviation σ_y of the wave function in y direction. The solid black lines represent the bulk band structure. The calculation includes the application of a finite electric field to the top of the quantum well. The induced Rashba effect results in a splitting of the bulk bands as well as in a tilting of the spin polarization of the helical edge states (indicated by the black arrows). The meaning of the Roman numerals is discussed in the text. The dashed black line indicates the position of the Fermi level. **b**, Comparison of the gate voltage V_G dependence of the conductance G of QPC-I ($d_{QW} = 7\,\text{nm}$) and QPC-IX ($d_{QW} = 10.5\,\text{nm}$). The blue trace is equivalent to the data shown in Fig. 4.4c. The grey trace represents a measurement of QPC-I over a wider range of gate voltage as for the data shown in Fig 2.11 and is shifted with regard to both axes to ensure comparability (by $\Delta G = 2e^2/h$ with regard to the ordinate). **c**, Gate voltage dependence of the conductance of QPC-IX and of QPC-XV for wider ranges of the gate voltage. Both traces are shifted with regard to the gate voltage axis in order to ensure comparability between the topological regime of QPC-IX and the n-i-n regime of QPC-XV.

regime. This result indicates a similar bulk band gap size of the two samples, which seems convenient since both devices are fabricated from quantum wells with $d_{\mathrm{QW}} = 10.5\,\mathrm{nm}$.

With passing a certain threshold value towards more negative gate voltages, the conductance of QPC-XV increases again, which is attributed to entering the n-p-n regime. Referring to previous statements, this observation can be explained with a lowering of the Fermi level deeper into the valence bands and hence beyond the camel back due to the application of very high gate voltages. In this scenario, the Fermi momentum mismatch between valence and conduction bands is reduced, which eventually enables bulk transport in the n-p-n regime.

Interestingly, this increase of conductance for the case of QPC-XV coincides with a decrease of conductance for the case of QPC-IX – below $G \approx e^2/h$. This behaviour insinuates that the effect causing the 0.5 anomaly seems to be fragile with respect to the influence of occurring bulk transport. Since the so far discussed experiments suggest an inter-edge interaction mechanism between the helical edge states to be responsible for the occurrence of the 0.5 anomaly, a parasitic impact of bulk transport appears reasonable.

4.2.4 Detection of a backscattered state in a multi-terminal device geometry

The 0.5 anomaly regime is characterized by a conductance of $G \approx e^2/h$. This value implies the transmission of one QSH edge channel through the QPC, while the other one is reflected (see Fig. 4.8a for a sketch). Such an assumption of one backscattered helical edge channel can be tested by realizing additional voltage probes in a Hall geometry adjacent to both sides of the QPC, which is sketched in Fig. 4.8b. As long as the device is in the QSH regime, both helical edge channels are transmitted. Then, the expected values of the longitudinal resistance R_{xx} and the transversal resistance R_{xy} are

$$R_{\mathrm{xx}}(\text{1-4, 2-3}) = \frac{h}{2e^2} \quad \text{and} \quad R_{\mathrm{xy}}(\text{1-4, 6-2}) = 0\,. \tag{4.1}$$

However, when one QSH edge channel gets reflected, these values change to

$$R_{\mathrm{xx}}(\text{1-4, 2-3}) = \frac{2h}{3e^2} \quad \text{and} \quad R_{\mathrm{xy}}(\text{1-4, 6-2}) = \frac{h}{3e^2} \tag{4.2}$$

according to predictions by Landauer-Büttiker theory for one backscattered helical edge channel in a six-terminal device at zero magnetic field [10]. It should be noted that these values presume a full reflection of one edge channel as well as a complete transmission of the other edge channel. The fabrication process for such a multi-terminal QPC device was developed within the scope of this thesis.

Device concept and lithographic fabrication

The device concept of a multi-terminal QPC sample is schematically shown in Fig. 4.9a. The mesa can be described by a standard Hall bar geometry, which is modified by an embedded

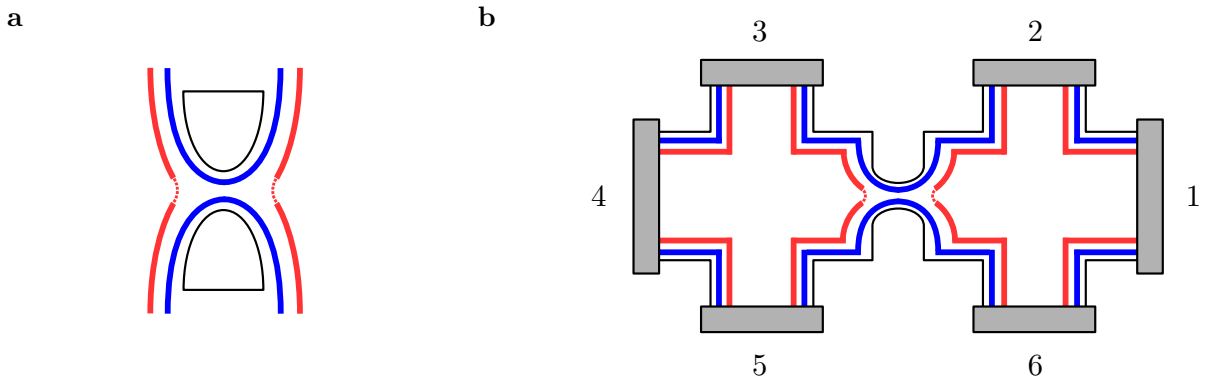

Figure 4.8: **a**, Sketch of a transport situation within a topological QPC device, in which one of the helical edge channels is completely backscattered, while the other one is transmitted through the constriction. **b**, Sketch of the analogous transport situation in a topological multi-terminal QPC device.

constriction in its middle part forming a QPC. In order to be able to tune the Fermi level of the QPC separately from the surrounding reservoirs and thus to enhance device controllability, three individual top gate electrodes are patterned. For the detection of a backscattered state in the context of the 0.5 anomaly, the QPC part of a multi-terminal QPC device has to be tuned to the 0.5 anomaly regime, whereas the adjacent reservoirs have to be tuned to the QSH regime.

The underlying approach of device fabrication is analogue to the concept developed for conventional QPC devices. The etching of the mesa is done in three steps. After the Hall bar geometry is defined in a first etching step, the QPC is etched in a second step using a dedicated etching time (see Fig. 4.9b,c – EBL used for both steps). The outer mesa is etched in a final third step using optical lithography methods.

Subsequently, the three top gate electrodes are structured using EBL. In a first step, the two separated gate electrodes covering the reservoir areas are patterned simultaneously (gate electrode A and B, see Fig. 4.9d–f). The width of the gap W_{Gap} between the two electrodes effectively defines the parameter L_{Gate} of the QPC part of the multi-terminal device. The extent of the gap width can be tuned by design modifications.

Due to the utilized exposure and development parameters, the developed PMMA mask for structuring gate electrode A and B exhibits a pronounced undercut. If the design is chosen such that W_{Gap} is sufficiently small, the two resist-free areas are not separated by a dense line of PMMA anymore. However, a PMMA bridge is formed. Thus, the subsequently deposited HfO_2 layer covers the whole area of the mesa (see the green layer in Fig. 4.9g), while the metallized gate electrodes remain separated. Such a scenario is beneficial for the intended experiment, since HfO_2 sidewalls would have a negative impact on the functionality of the to be structured QPC gate electrode otherwise.

Next, the gate electrode covering the QPC area is patterned (gate electrode C, sketched in Fig. 4.9a,g). In order to avoid ungated areas between the electrodes, the design is chosen such that gate electrode C overlaps with gate electrodes A and B. The deposition of a second film of HfO_2 (grey layer in Fig. 4.9g) ensures that the three gate electrodes remain electrically separated.

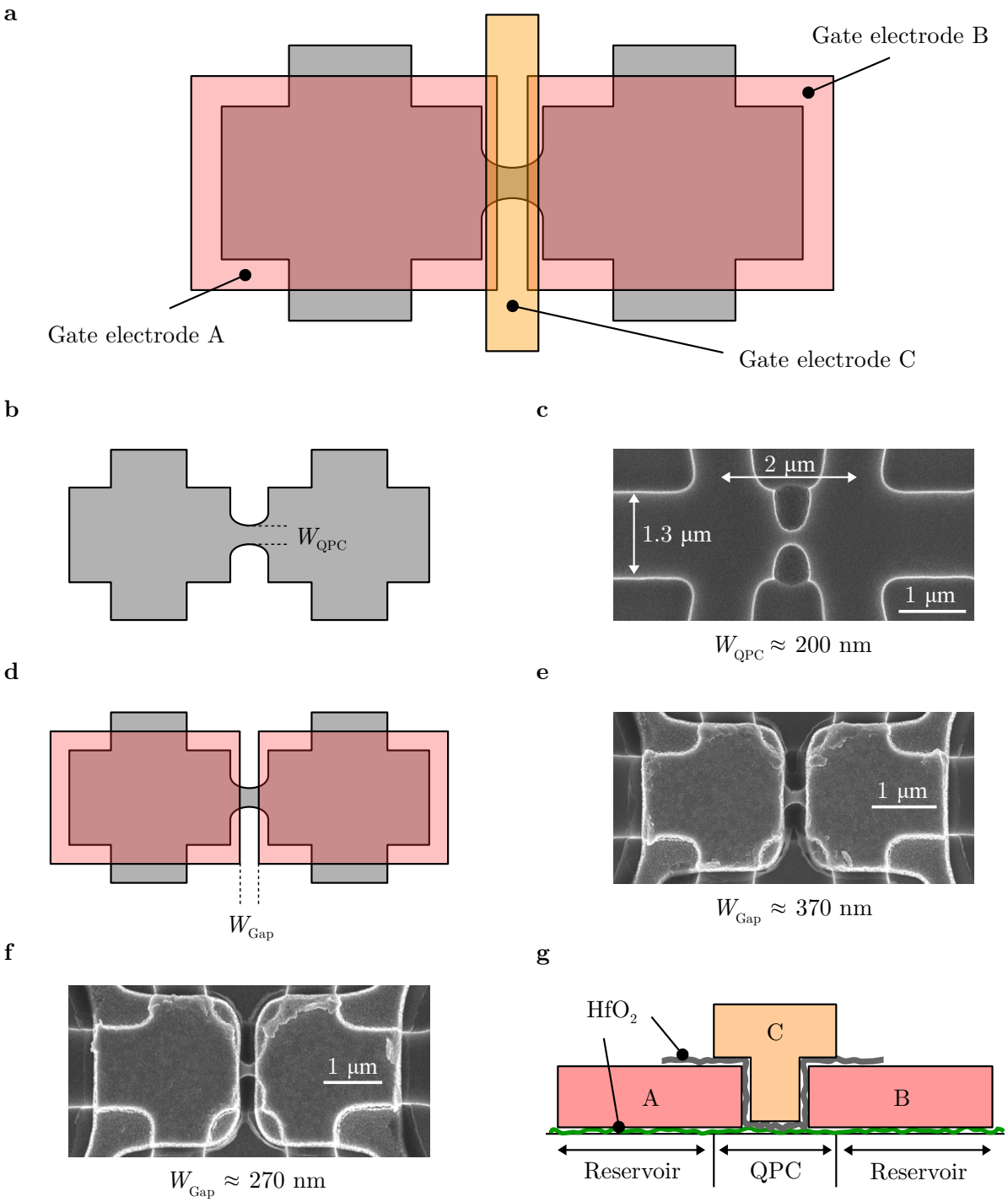

Figure 4.9: **a**, Sketch of the concept of a multi-terminal QPC device. Three individual top gate electrodes are defined. **b**,**c**, Sketch and scanning electron micrograph of the mesa of a multi-terminal QPC device. Relevant dimensions are indicated. **d**, Sketch of the mesa covered by gate electrodes A and B. The electrodes are separated by a gap with a width W_{Gap}. **e**,**f**, Scanning electron micrographs of two exemplary devices covered by gate electrodes A and B. Relevant dimensions are indicated. **g**, Cross section of a final device along the transport axis of the QPC. The gate electrodes, the area of the QPC and of the surrounding reservoirs as well as the two individual HfO_2 layers are indicated.

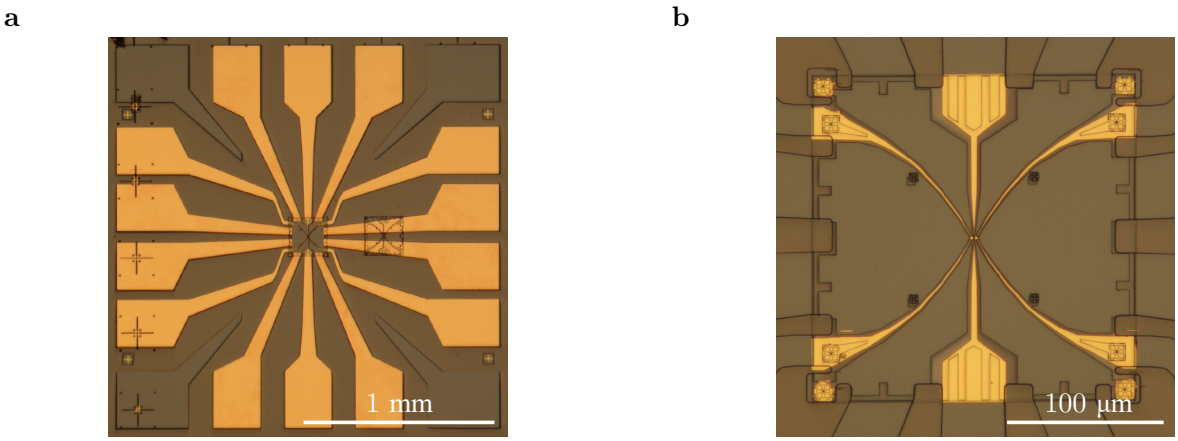

Figure 4.10: **a**, Optical micrograph of a full multi-terminal QPC sample. **b**, Zoom on the central part of the sample. The optical micrograph shows the device after defining the three top gate electrodes.

Furthermore, screening effects are expected to prevent cross-influences between the individual gate electrodes. Lastly, ohmic contacts and gate leads are structured using optical lithography. Complementary optical micrographs of an exemplary multi-terminal QPC device are presented in Fig. 4.10. Process details and parameters are presented in Appendix C.

It should be noted that the fabrication process is still in a preliminary condition. The remaining technological obstacle appears at the interface between gate electrode A/B and gate electrode C. For every fabricated device, the three electrodes are shorted to each other, thus effectively forming one extended top gate electrode covering the whole device. A mere increase of the thickness of the HfO_2 layer associated with gate electrode C (grey layer in Fig. 4.9g) turned out to be not sufficient to solve this problem.

Consequently, the fabricated devices are only working under limited conditions. Due to the outlined situation, the gate action for the two reservoir areas is higher (lower thickness of the HfO_2 layer) than for the QPC area (larger thickness of the HfO_2 layer, combination of the green and grey layer in Fig. 4.9g). Thus, there is only a small range of gate voltage in which the reservoirs are located in the QSH regime before they become p-conducting.

Device characterization

The gate voltage dependence of the two-point conductance $G_{xx}(1\text{-}4, 1\text{-}4)$ of the multi-terminal QPC device QPC-XVI is presented in the upper panel of Fig. 4.11. With lowering the gate voltage, a clear step-like behaviour is observable as well as a transition to a long and stable plateau of low conductance. This plateau is identified as the 0.5 anomaly regime, even though the conductance is not in accordance with the expected value of $G \approx e^2/h$. The latter is due to a gate voltage induced increase of the resistance of the reservoirs, which is also responsible for the shifted position of the QSH plateau and of the plateaus caused by trivial ballistic 1D transport.

The lower panel of Fig. 4.11 shows the simultaneously measured gate voltage dependence of the transversal resistance $R_{xy}(1\text{-}4, 6\text{-}2)$. For the trivial regime and for the QSH regime of the

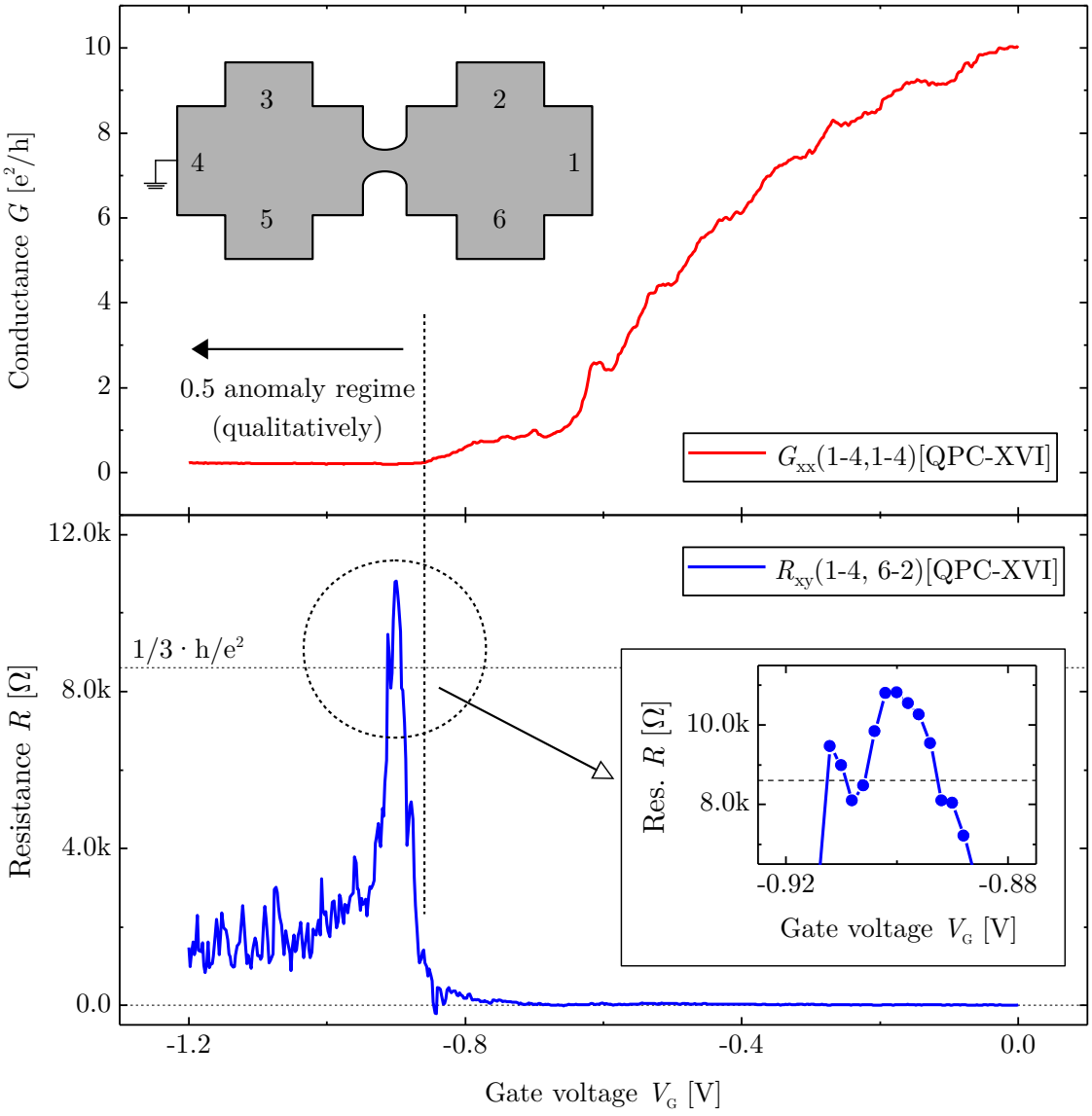

Figure 4.11: Transport analysis of the multi-terminal QPC device QPC-XVI. The upper panel shows the two-point conductance G_{xx}(1-4,1-4) as a function of the gate voltage V_G. The inset of the upper panel shows the contact configuration of the measured device. The lower panel presents the gate voltage dependence of the transversal resistance R_{xy}(1-4,6-2). The inset of the lower panel shows a zoom on the acquired data. Both traces were measured simultaneously and are not shifted with regard to the applied gate voltage.

two-point conductance, the potential difference between contact 6 and contact 2 remains zero, which yields $R_{xy}(1\text{-}4, 6\text{-}2) = 0\,\Omega$. However, as soon as the QPC enters the 0.5 anomaly regime, a significant voltage drop emerges. Moreover, the corresponding transversal resistance exhibits a maximum around $R_{xy}(1\text{-}4, 6\text{-}2) = 1/3 \cdot h/e^2$, thus being in accordance with the value predicted by Landauer-Büttiker calculations for one reflected helical edge channel (see also the inset of the lower panel of Fig. 4.11).

Due to the absence of any magnetic field influence ($B_z = 0\,\mathrm{T}$), the detection of a finite voltage in a Hall geometry in the given transport regime can only be caused by helical edge

channels. Thus, the data presented in Fig. 4.11 proves that the occurrence of the 0.5 anomaly is accompanied by a backscattered helical edge channel. The decrease to lower (but finite) resistance values for more negative gate voltages is attributed to scattering events caused by the impact of occurring p-bulk transport in the reservoirs. Due to device specific issues, contact 3 and contact 5 are not working, thus no further four-point configurations of interest can be analysed.

4.3 Origin of the 0.5 anomaly – differentiation of two models based on electron-electron interactions

The discussion of Section 4.2.3 demonstrates that the emergence of the 0.5 anomaly cannot be captured within the single particle picture. Furthermore, the acquired data suggests that the occurrence of the 0.5 anomaly is caused by an inter-edge interaction mechanism, which is accompanied by the backscattering of one helical edge channel. At the moment, two plausible explanatory models based on electron-electron interactions across the device edges exist.

4.3.1 Tomonaga-Luttinger liquid theory

In the presence of interactions, a 1D system behaves fundamentally different than its counterparts of higher dimensionality. For the 2D and 3D case, the Fermi liquid theory describes interacting electron systems in the context of almost free quasiparticles with an effective mass. However, in the 1D case, this quasiparticle picture collapses. The pictorial reason is that a single particle cannot move without perturbing its neighbours. Thus, only collective excitations are possible, which represent the eigenstates of the system [11]. This very scenario of an interacting 1D system is captured by the Tomonaga-Luttinger liquid (TLL) theory [12–15].

Tomonaga-Luttinger liquid theory in a nutshell

The TLL theory is based on the description of a 1D many-body system consisting of interacting (relativistic) fermions as a model of free bosons. This transformation is referred to as bosonization, which requires a linear energy dispersion. Such a linear spectrum is either present in a 1D gas of relativistic free fermions or can be obtained by the linearization of a parabolic spectrum around the Fermi energy in the context of a many-body system of non-relativistic free fermions [16]. For an in-depth introduction to bosonization, the interested reader is referred for example to Ref. [16].

For a QSH system, a linear energy dispersion is naturally present. In terms of the thus possible description within the scope of the TLL model, the edge states of a QSH insulator are referred to as a helical Luttinger liquid (HLL) [17]. Such a HLL exhibits spin-momentum-locking and consists of bosonic spin σ and charge ρ modes [11], which is sketched in Fig. 4.12b.

The strength of interactions between single particles within the 1D system is described by the Luttinger parameter K_L. Repulsive electron-electron interactions are characterized by

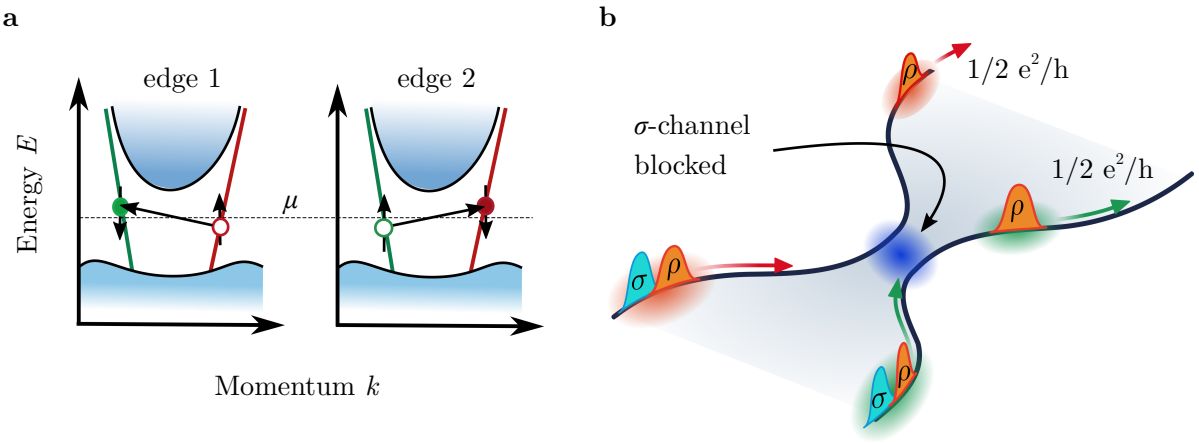

Figure 4.12: **a**, Schematic of the correlated two particle backscattering process, which causes the opening of a spin gap. The Fermi level μ is indicated. **b**, Illustration of the reduction of the QPC conductance in the HLL picture, where σ and ρ indicate the bosonic spin and charge modes.

$0 \leq K_\mathrm{L} < 1$, while attractive interactions are present for $K_\mathrm{L} > 1$. The noninteracting case is represented by $K_\mathrm{L} = 1$ [11, 16, 19]. An estimation of K_L for a HLL can be obtained using [20]

$$K_\mathrm{L} = \left[1 + \frac{2e^2}{\pi\epsilon_0\epsilon_\mathrm{r}\hbar v_\mathrm{F}} \ln\left(\frac{7.1d}{\xi + 0.8d_\mathrm{QW}}\right)\right]^{-1/2}, \tag{4.3}$$

where ϵ_0 is the permittivity of free space, ϵ_r is the dielectric constant, v_F is the Fermi velocity, d is the distance between the edge channels and the top gate electrode, d_QW is the quantum well thickness and $\xi = 2\hbar v_\mathrm{F}/E_\mathrm{Gap}$ with E_Gap representing the bulk band gap of the system under consideration [3, 20].

Opening of a spin gap due to Coulomb interactions

Utilizing the introduced concept of HLLs, a model explaining the occurrence of the 0.5 anomaly can be compiled. Assuming weak repulsive electron-electron interactions across the device edges, Ref. [21] defines a two-particle scattering term which describes a backscattering process between the QSH edge states of opposite sample edges. The process preserves the number of right and left movers and is sketched in Fig. 4.12a.

To be of relevance, the scattering term furthermore requires a sufficiently high magnitude of Rashba coupling strength being present within the examined system. If this condition is met, Ref. [21] demonstrates using bosonization techniques that the correlated backscattering process depicted in Fig. 4.12a acts as a gap to the spin sector of the HLL. This situation is sketched in Fig. 4.12b and is accompanied by a reduced conductance of $G = e^2/h = 0.5 \cdot G_\mathrm{QSH}$. For a detailed analytic description of the discussed mechanism, the interested reader is referred to Refs. [18, 21]. Using $\epsilon_\mathrm{r} = 20$ for HgTe [3], $v_\mathrm{F} = 6 \cdot 10^5\,\mathrm{ms}^{-1}$, $d = 60\,\mathrm{nm}$, $d_\mathrm{QW} = 10.5\,\mathrm{nm}$ and $E_\mathrm{Gap} = 10\,\mathrm{meV}$, Eq. 4.3 yields a value of $K_\mathrm{L} \approx 0.55$, which is in accordance with repulsive interactions. The values of v_F and E_Gap are extracted from the band structure calculation shown in Fig. 4.7a, the

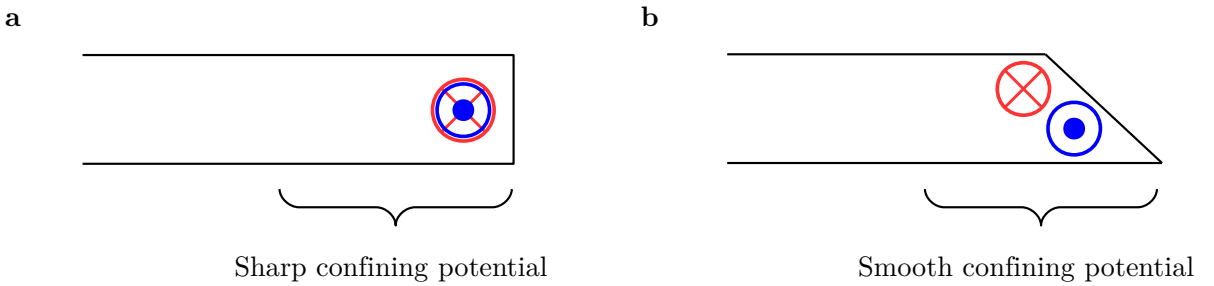

Figure 4.13: **a**, Sketch of a sample hosting the QSH regime with a sharp confining edge potential. The helical edge states lie on top of each other in space. **b**, Sketch of a sample hosting the QSH regime with a smooth confining edge potential. In such a scenario, the authors of Ref. [10] predict the emergence of a helical edge reconstruction mechanism, which leads to a separation of the helical edge states in space.

approximated value of d stems from the addition of the cap layer thickness of the quantum well and the thickness of the Ti/HfO_2 stack.

4.3.2 Helical edge reconstruction

The second model suitable to explain the emergence of the 0.5 anomaly is a helical edge reconstruction mechanism formulated by Ref. [10]. The authors propose that when considering a realistic smooth confining potential at the sample edge instead of an unrealistic sharp one, the pair of counterpropagating helical edge channels becomes separated in space (see Fig. 4.13 for a sketch). If such a scenario is applied to a QPC device, falling below a threshold value of the QPC width causes the wave functions of the inner pair of edge states to overlap earlier than for the outer pair. With further taking repulsive electron-electron interactions into account, the authors expect that such a regime enables a selective backscattering process to take place within the QPC (see Fig. 4.8a). They assume the corresponding conductance pattern to exhibit a second plateau at $G = e^2/h = 0.5 \cdot G_{\mathrm{QSH}}$ in addition to the conventional one at $G_{\mathrm{QSH}} = 2e^2/h$. When the QPC is furthermore embedded in a six-terminal device, the authors predict that the regime of $G = 0.5 \cdot G_{\mathrm{QSH}}$ is accompanied by the emergence of a finite Hall resistance of $R_{\mathrm{xy}}(1\text{-}4, 6\text{-}2) = h/3e^2$ at zero magnetic field. The latter relies on the assumption that the inner edge channel is completely reflected, while the outer one is still entirely transmitted [10]. This situation is sketched in Fig. 4.8b.

4.4 Recapitulating discussion from an experimental perspective

When reviewing the two introduced models in the context of the discussed experimental observations, it has to be noted that both are consistent with the width dependence of the 0.5 anomaly (see Fig. 4.4). This conclusion stems from the fact that an inter-edge interaction mechanism between helical edge channels has to exhibit a dependence on the device width and thus on the distance between the sample edges by conception. Moreover, this consistency is also

given for the observed decrease of conductance below $G \approx e^2/h$ at large negative gate voltage values (see Fig. 4.7c), which is attributed to the impact of arising bulk transport in the n-p-n regime. In this scenario, the latter causes the breakdown of the inter-edge interaction mechanism.

Furthermore, each of the two models is in accordance with the occurrence of the 0.5 anomaly in quantum wells with $d_{\mathrm{QW}} = 10.5\,\mathrm{nm}$, whereas the feature is absent in quantum wells with $d_{\mathrm{QW}} = 7\,\mathrm{nm}$. For both described mechanisms, the pinning of the Fermi level at the camel back is of crucial importance. While it enables a sufficiently large value of Rashba spin-orbit coupling for the spin gap to open in the HLL model, the Fermi level pinning also generates a highly p-doped bulk density within the QPC area. This high density of states of p-carriers causes the formation of a smooth confining potential at the device edge, thus giving rise to the helical edge reconstruction mechanism. Due to the lack of Fermi level pinning for quantum wells with $d_{\mathrm{QW}} = 7\,\mathrm{nm}$, both mechanisms are not applicable, which is in accordance with the experimentally demonstrated absence of the 0.5 anomaly in QPC devices fabricated from such quantum wells.

With regard to the detection of a backscattered helical edge channel in a multi-terminal QPC device, the situation is slightly different. While such an observation is central in the context of the helical edge reconstruction mechanism proposed by Ref. [10], the harmonization of this result with the proposed presence of a spin gap seems less trivial. This is related to the fact that after the emergence of such a gapped state, only the charge mode at each edge remains propagating (see Fig. 4.12b). However, this scenario does not result in a potential difference within an adjacent Hall geometry.

A possible explanation is given by the assumption that the HLL description of the inter-edge interaction mechanism is only valid for the centre of the QPC, where the correlated backscattering process – and thus the opening of a spin gap – takes place. However, the strength of inter-edge interaction reduces when moving away from the centre (increasing the distance between the edges). Consequently, it appears plausible that the correlated two particle picture description of transport collapses to an effective single particle picture transport situation – thus giving rise to the propagation of one helical edge channel.

Since both theoretic models are overall consistent with the experimental observations made in the context of the 0.5 anomaly, it is not possible to discard or favour one of the two mechanisms. From an experimental point of view, the presented results prove in any case the presence of an inter-edge interaction mechanism between helical edge channels, which is accompanied by the formation of a gapped topological state as well as by a backscattered helical edge channel – a novel result observed for the first time in a QSH insulator. Moreover, the transmission of only one helical edge channel is equivalent to the generation of a 100 % spin-polarized current.

4.5 Conclusion

The unexpected observation of the 0.5 anomaly in HgTe quantum wells with $d_{\mathrm{QW}} = 10.5\,\mathrm{nm}$ represents further evidence regarding the significance of realizing a working QPC technology in the context of knowledge gain about QSH systems. Moreover, the discussion of the results

has demonstrated how fundamental the information about the exact band structure is for device realizations beyond the BHZ limit. As explicated, the formation of the camel back – which is not covered by the BHZ model – is crucial for understanding the phenomenon of the 0.5 anomaly. The emergence of the latter is accompanied by a backscattered helical edge channel, which is evidenced by examining a specifically developed multi-terminal QPC device. However, the device technology still exhibits a preliminary character.

A completely functional multi-terminal device to be realized in the future might support the identification of the actual mechanism causing the occurrence of the 0.5 anomaly and is thus expected to help determining which of the two discussed models provides the more reliable description. Beyond an understanding of the 0.5 anomaly in thick HgTe quantum wells, such a device is furthermore of high interest for analysing transport in QPCs in general. Due to its concept, such a multi-terminal QPC sample provides three independently gated device segments – the QPC itself and the two adjacent reservoirs. Hence, the examination of arbitrary combinations of transport regimes within one device becomes possible.

4.6 Sample overview

QPC No.	d_{QW} [nm]	W_{QPC} [nm]	L_{QPC} [nm]	L_{Gate} [nm]	$n_e(0\,V)$ [cm^{-2}]	$\mu_e(0\,V)$ [$cm^2V^{-1}s^{-1}$]	l_e [µm]	Layer thicknesses [nm]
I	7.0	100	500	250	$5.2 \cdot 10^{11}$	$2.7 \cdot 10^5$	3.2	70/9/70/7/50
IX	10.5	150	500	250	$5.9 \cdot 10^{11}$	$3.2 \cdot 10^5$	4.1	73/10/73/10.5/52
X	10.5	250	500	250	$5.9 \cdot 10^{11}$	$3.2 \cdot 10^5$	4.1	73/10/73/10.5/52
XI	10.5	200	500	250	$5.9 \cdot 10^{11}$	$3.2 \cdot 10^5$	4.1	73/10/73/10.5/52
XII	10.5	100	500	250	$5.9 \cdot 10^{11}$	$3.2 \cdot 10^5$	4.1	73/10/73/10.5/52
XIII	10.5	100	500	250	$5.9 \cdot 10^{11}$	$3.2 \cdot 10^5$	4.1	73/10/73/10.5/52
XIV	10.5	50	500	250	$5.9 \cdot 10^{11}$	$3.2 \cdot 10^5$	4.1	73/10/73/10.5/52
XV	10.5	25	500	250	$5.9 \cdot 10^{11}$	$3.2 \cdot 10^5$	4.1	73/10/73/10.5/52
XVI	10	200	500	250	$5.8 \cdot 10^{11}$	$2.0 \cdot 10^5$	2.5	63/9/63/10/45

Table 4.1: Summary of the sample and material parameters for each discussed QPC device indicated by Roman numerals. The layer thickness values refer to the sketched layer stack shown in Fig. 2.7b. The given numbers (from right to left) are attributed to the sketched layers from top to bottom. The thickness of the buffer as well as of the substrate is not included.

BIBLIOGRAPHY

[1] E. G. Novik, A. Pfeuffer-Jeschke, T. Jungwirth, V. Latussek, C. R. Becker, G. Landwehr, H. Buhmann, and L. W. Molenkamp, *Band structure of semimagnetic* $Hg_{1-y}Mn_yTe$ *quantum wells,* Physical Review B **72**, 035321 (2005).

[2] S. Shamim, W. Beugeling, J. Böttcher, P. Shekhar, A. Budewitz, P. Leubner, L. Lunczer, E. M. Hankiewicz, H. Buhmann, and L. W. Molenkamp, *Emergent quantum Hall effects below 50 mT in a two-dimensional topological insulator,* Science Advances **6** (2020).

[3] S. Shamim, W. Beugeling, P. Shekhar, K. Bendias, L. Lunczer, J. Kleinlein, H. Buhmann, and L. W. Molenkamp, *Quantized spin Hall conductance in a magnetically doped two dimensional topological insulator,* Nature Communications **12**, 3193 (2021).

[4] H. van Houten, C. Beenakker, and B. van Wees, *Chapter 2 – Quantum Point Contacts,* in *Nanostructured Systems*, Semiconductors and Semimetals, Vol. 35 (Elsevier, Amsterdam, 1992).

[5] C. Stampfer, J. Güttinger, F. Molitor, D. Graf, T. Ihn, and K. Ensslin, *Tunable Coulomb blockade in nanostructured graphene,* Applied Physics Letters **92**, 012102 (2008).

[6] K. J. Thomas, J. T. Nicholls, M. Y. Simmons, M. Pepper, D. R. Mace, and D. A. Ritchie, *Possible Spin Polarization in a One-Dimensional Electron Gas,* Physical Review Letters **77**, 135 (1996).

[7] F. Bauer, J. Heyder, E. Schubert, D. Borowsky, D. Taubert, B. Bruognolo, D. Schuh, W. Wegscheider, J. V. Delft, and S. Ludwig, *Microscopic origin of the '0.7-anomaly' in quantum point contacts,* Nature **501**, 73 (2013).

[8] J. I. Väyrynen and T. Ojanen, *Electrical Manipulation and Measurement of Spin Properties of Quantum Spin Hall Edge States,* Physical Review Letters **106**, 076803 (2011).

[9] L. Ortiz, R. A. Molina, G. Platero, and A. M. Lunde, *Generic helical edge states due to Rashba spin-orbit coupling in a topological insulator,* Physical Review B **93**, 205431 (2016).

[10] J. Wang, Y. Meir, and Y. Gefen, *Spontaneous Breakdown of Topological Protection in Two Dimensions,* Physical Review Letters **118**, 046801 (2017).

[11] G. Dolcetto, M. Sassetti, and T. L. Schmidt, *Edge physics in two-dimensional topological insulators,* Rivista del Nuovo Cimento **39**, 113 (2016).

[12] S.-i. Tomonaga, *Remarks on Bloch's Method of Sound Waves applied to Many-Fermion Problems,* Progress of Theoretical Physics **5**, 544 (1950).

[13] J. M. Luttinger, *An Exactly Soluble Model of a Many-Fermion System,* Journal of Mathematical Physics **4**, 1154 (1963).

[14] F. D. M. Haldane, *Effective Harmonic-Fluid Approach to Low-Energy Properties of One-Dimensional Quantum Fluids,* Physical Review Letters **47**, 1840 (1981).

[15] F. D. M. Haldane, *'Luttinger liquid theory' of one-dimensional quantum fluids. I. Properties of the Luttinger model and their extension to the general 1D interacting spinless Fermi gas,* Journal of Physics C: Solid State Physics **14**, 2585 (1981).

[16] F. Geißler, *Transport properties of helical Luttinger liquids*, Ph.D. thesis (2017).

[17] C. Wu, B. A. Bernevig, and S.-C. Zhang, *Helical Liquid and the Edge of Quantum Spin Hall Systems,* Physical Review Letters **96**, 106401 (2006).

[18] C. T. Fleckenstein, *Conception and detection of exotic quantum matter in mesoscopic systems*, Ph.D. thesis (2020).

[19] T. Li, P. Wang, H. Fu, L. Du, K. A. Schreiber, X. Mu, X. Liu, G. Sullivan, G. A. Csáthy, X. Lin, and R.-R. Du, *Observation of a Helical Luttinger Liquid in* InAs/GaSb *Quantum Spin Hall Edges,* Physical Review Letters **115**, 136804 (2015).

[20] J. C. Y. Teo and C. L. Kane, *Critical behavior of a point contact in a quantum spin Hall insulator,* Physical Review B **79**, 235321 (2009).

[21] J. Strunz, J. Wiedenmann, C. Fleckenstein, L. Lunczer, W. Beugeling, V. L. Müller, P. Shekhar, N. T. Ziani, S. Shamim, J. Kleinlein, H. Buhmann, B. Trauzettel, and L. W. Molenkamp, *Interacting topological edge channels,* Nature Physics **16**, 83 (2020).

5

Summary

Quantum point contacts (QPCs) are one-dimensional constrictions in an otherwise extended two-dimensional electron or hole system. Since their first realization in GaAs based two-dimensional electron gases [1, 2], QPCs have become basic building blocks of mesoscopic physics and are used in manifold experimental contexts. A so far unrealized goal however is the implementation of QPCs in the new material class of two-dimensional topological insulators, which host the emergence of the so-called quantum spin Hall (QSH) effect [3–5]. The latter is characterized by the formation of conducting one-dimensional spin-polarized states at the device edges, while the bulk is insulating. Consequently, an implemented QPC technology can be utilized to bring the QSH edge channels in close spatial proximity, thus for example enabling the study of interaction effects between the edge states [6, 7]. The thesis at hand describes the technological realization as well as the subsequent experimental characterization and analysis of QPCs in a QSH system for the first time.

After an introduction is given in Chapter 1, the subsequent Chapter 2 starts with discussing the peculiar band structure of HgTe. The emergence of the QSH phase for HgTe quantum wells with an inverted band structure is explained. For the band inversion to occur, the quantum wells have to exhibit a well thickness d_{QW} above a critical value ($d_{\mathrm{QW}} > d_{\mathrm{c}} = 6.3\,\mathrm{nm}$). Subsequently, the concept of QPCs is explicated and the corresponding transport behaviour is analytically described. Following the discussion of relevant constraints when realizing a QPC technology in a QSH system, a newly developed lithography process utilizing a multi-step wet etching technique for fabricating QPC devices based on HgTe quantum wells is presented. Transport measurements of exemplary devices show the expected conductance quantization in steps of $\Delta G \approx 2e^2/h$ within the conduction band for a topological as well as for a trivial ($d_{\mathrm{QW}} < d_{\mathrm{c}}$) QPC. For the topological case, the residual conductance within the bulk band gap saturates at $G_{\mathrm{QSH}} \approx 2e^2/h$ due to presence of the QSH state, while it drops to $G \approx 0$ for the trivial device. Moreover, bias voltage dependent measurements of the differential conductance of an inverted sample provide explicit proof of the unperturbed coexistence of topological and trivial transport modes.

In a next step, Chapter 3 describes the emergence of a QSH interferometer state in narrow QPC devices with a quantum well thickness of $d_{\mathrm{QW}} = 7\,\mathrm{nm}$. Presented band structure calculations reveal that the spatial extension of the QSH edge states depends on the position of the Fermi energy within the bulk band gap. As a consequence, reservoir electrons with randomized spin couple to both edge channels with the same probability under certain conditions, thus causing the formation of a QSH ring. A straightforward model capturing and specifying the occurrence of such a QSH interferometer is provided as well as substantiated by two experimental plausibility checks. After relevant quantum phases are theoretically introduced, the discussion of the obtained data reveals the accumulation of an Aharonov-Bohm phase [8], of a dynamical Aharonov-Casher phase [9] as well as of a spin-orbit Berry phase of π [10] in appropriate QPC devices. These results are consistent with analytic model considerations.

The last part of this thesis, Chapter 4, covers the observation of an unexpected conductance pattern for QPC samples fabricated from quantum wells with $d_{\mathrm{QW}} = 10.5\,\mathrm{nm}$. In these devices, an anomalous plateau at $G \approx e^2/h = 0.5 \cdot G_{\mathrm{QSH}}$ emerges in addition to the QSH phase entailed residual conductance of $G_{\mathrm{QSH}} \approx 2e^2/h$. This so-called 0.5 anomaly occurs only for a specific interval of QPC width values, while it starts to get lost for too large sample widths. Furthermore, presented temperature and bias voltage dependent measurements insinuate that the emergence of the 0.5 anomaly is related to a gapped topological state. Additional characterization of this peculiar transport regime is provided by the realization of a novel device concept, which integrates a QPC within a standard Hall bar geometry. The results of the experimental analysis of such a sample link the occurrence of the 0.5 anomaly to a backscattered QSH channel. Thus, following a single particle perspective argumentation, it is reasoned that only one edge channel is transmitted in the context of the 0.5 anomaly. Two theoretic models possibly explaining the emergence of the 0.5 anomaly – based on electron-electron interactions – are discussed.

To conclude, the implementation of a working QPC technology in a QSH system represents a paramount development in the context of researching two-dimensional topological insulators and enables a multitude of future experiments. QPC devices realized in a QSH system are for example envisaged to allow for the detection of Majorana fermions [11] and parafermions [12]. Furthermore, the reported formation of a QSH interferometer state in appropriate QPC devices is of high interest. The observed dynamical Aharonov-Casher phase in the QSH regime enables a controllable modulation of the topological conductance, thus providing the conceptual basis for a topological transistor [13, 14]. Moreover, due to the resilience of geometric phases against dephasing [15, 16], the presence of a spin-orbit Berry phase of π represents a promising perspective with regard to possible quantum computation concepts [17–19]. Besides that, the transmission of only one QSH edge channel due to the emergence of the 0.5 anomaly is equivalent to 100 % spin polarization, which is an essential ingredient for realizing spintronic applications [20, 21]. Hence, the thesis at hand covers the experimental detection of three effects of fundamental importance in the context of developing new generations of logic devices – based on QPCs fabricated from topological HgTe quantum wells.

BIBLIOGRAPHY

[1] B. J. van Wees, H. van Houten, C. W. J. Beenakker, J. G. Williamson, L. P. Kouwenhoven, D. van der Marel, and C. T. Foxon, *Quantized conductance of point contacts in a two-dimensional electron gas,* Physical Review Letters **60**, 848 (1988).

[2] D. A. Wharam, T. J. Thornton, R. Newbury, M. Pepper, H. Ahmed, J. E. F. Frost, D. G. Hasko, D. C. Peacock, D. A. Ritchie, and G. A. C. Jones, *One-dimensional transport and the quantisation of the ballistic resistance,* Journal of Physics C: Solid State Physics **21**, L209 (1988).

[3] C. L. Kane and E. J. Mele, *Quantum Spin Hall Effect in Graphene,* Physical Review Letters **95**, 226801 (2005).

[4] B. A. Bernevig, T. L. Hughes, and S.-C. Zhang, *Quantum Spin Hall Effect and Topological Phase Transition in HgTe Quantum Wells,* Science **314**, 1757 (2006).

[5] M. König, S. Wiedmann, C. Brüne, A. Roth, H. Buhmann, L. W. Molenkamp, X. L. Qi, and S.-C. Zhang, *Quantum Spin Hall Insulator State in HgTe Quantum Wells,* Science **318**, 766 (2007).

[6] F. Dolcini, *Full electrical control of charge and spin conductance through interferometry of edge states in topological insulators,* Physical Review B **83**, 165304 (2011).

[7] J. Wang, Y. Meir, and Y. Gefen, *Spontaneous Breakdown of Topological Protection in Two Dimensions,* Physical Review Letters **118**, 046801 (2017).

[8] Y. Aharonov and D. Bohm, *Significance of Electromagnetic Potentials in the Quantum Theory,* Physical Review **115**, 485 (1959).

[9] Y. Aharonov and A. Casher, *Topological Quantum Effects for Neutral Particles,* Physical Review Letters **53**, 319 (1984).

[10] A. G. Aronov and Y. B. Lyanda-Geller, *Spin-orbit Berry phase in conducting rings,* Physical Review Letters **70**, 343 (1993).

[11] J. Li, W. Pan, B. A. Bernevig, and R. M. Lutchyn, *Detection of Majorana Kramers Pairs Using a Quantum Point Contact,* Physical Review Letters **117**, 046804 (2016).

[12] C. Fleckenstein, N. T. Ziani, and B. Trauzettel, *$\mathbb{Z}_4$ parafermions in Weakly Interacting Superconducting Constrictions at the Helical Edge of Quantum Spin Hall Insulators,* Physical Review Letters **122**, 066801 (2019).

[13] X. Qian, J. Liu, L. Fu, and J. Li, *Quantum spin Hall effect in two-dimensional transition metal dichalcogenides,* Science **346**, 1344 (2014).

[14] J. L. Collins, A. Tadich, W. Wu, L. C. Gomes, J. N. B. Rodrigues, C. Liu, J. Hellerstedt, H. Ryu, S. Tang, S.-K. Mo, S. Adam, S. A. Yang, M. S. Fuhrer, and M. T. Edmonds, *Electric-field-tuned topological phase transition in ultrathin Na_3Bi,* Nature **564**, 390 (2018).

[15] A. Carollo, I. Fuentes-Guridi, M. Santos França, and V. Vedral, *Geometric Phase in Open Systems,* Physical Review Letters **90**, 160402 (2003).

[16] S. Filipp, J. Klepp, Y. Hasegawa, C. Plonka-Spehr, U. Schmidt, P. Geltenbort, and H. Rauch, *Experimental Demonstration of the Stability of Berry's Phase for a Spin-1/2 Particle,* Physical Review Letters **102**, 030404 (2009).

[17] J. A. Jones, V. Vedral, A. Ekert, and G. Castagnoli, *Geometric quantum computation using nuclear magnetic resonance,* Nature **403**, 869 (2000).

[18] G. Falci, R. Fazio, G. M. Palma, J. Siewert, and V. Vedral, *Detection of geometric phases in superconducting nanocircuits,* Nature **407**, 355 (2000).

[19] E. Sjöqvist, *A new phase in quantum computation,* Physics **1**, 35 (2008).

[20] S. Datta and B. Das, *Electronic analog of the electro-optic modulator,* Applied Physics Letters **56**, 665 (1990).

[21] S. Datta, *How we proposed the spin transistor,* Nature Electronics **1**, 604 (2018).

6

Zusammenfassung

Quantenpunktkontakte (englisch: quantum point contacts, QPCs) sind eindimensionale Engstellen in einem ansonsten zweidimensionalen Elektronen- oder Lochsystem. Seit der erstmaligen Realisierung in GaAs-basierten zweidimensionalen Elektronengasen [1, 2] sind QPCs sukzessive zu einem Grundbestandteil mesoskopischer Physik geworden und erfahren in einer Vielzahl von Experimenten Anwendung. Jedoch ist es bis zur Anfertigung der vorliegenden Arbeit nicht gelungen, QPCs in der neuen Materialklasse der zweidimensionalen topologischen Isolatoren zu realisieren. In diesen Materialien tritt der sogenannte Quanten-Spin-Hall-Effekt (QSH-Effekt) auf [3–5], welcher sich durch die Ausbildung von leitfähigen, eindimensionalen sowie gleichermaßen spinpolarisierten Zuständen an der Bauteilkante auszeichnet, während die restlichen Bereiche der Probe isolierend sind. Ein in einem zweidimensionalen topologischen Isolator realisierter QPC kann demgemäß dafür benutzt werden, die sich stets an der Bauteilkante befindlichen QSH-Randkanäle einander räumlich anzunähern, was beispielsweise die Untersuchung potentieller Wechselwirkungseffekte zwischen ebenjenen Randkanälen ermöglicht [6, 7]. Die vorliegende Arbeit beschreibt die erstmalig erfolgreich durchgeführte Implementierung einer QPC-Technologie in einem QSH-System. Überdies werden die neuartigen Bauteile experimentell charakterisiert sowie analysiert.

Nach einer in Kapitel 1 erfolgten Einleitung der Arbeit beschäftigt sich das nachfolgende Kapitel 2 zunächst mit der besonderen Bandstruktur von HgTe. In diesem Kontext wird die Ausbildung der QSH-Phase für HgTe-Quantentröge mit einer invertierten Bandstruktur erläutert, welche für deren Auftreten eine Mindesttrogdicke von $d_{\mathrm{QW}} > d_{\mathrm{c}} = 6.3\,\mathrm{nm}$ aufweisen müssen. Im Anschluss wird das Konzept eines QPCs allgemein eingeführt sowie das zugehörige Transportverhalten analytisch beschrieben. Überdies werden die Einschränkungen und Randbedingungen diskutiert, welche bei der Realisierung eines QPCs in einem QSH-System Berücksichtigung finden müssen. Darauf folgt die Präsentation des eigens zur QPC-Herstellung entwickelten Lithographieprozesses, welcher auf einer mehrstufigen Anwendung eines für HgTe-Quantentrogstrukturen geeigneten nasschemischen Ätzverfahrens beruht. Die im Nachgang diskutierten Transportmessungen exem-

plarischer Proben zeigen die erwartete Leitwertquantisierung in Schritten von $\Delta G \approx 2e^2/h$ im Bereich des Leitungsbandes – sowohl für eine topologische als auch für eine triviale ($d_{\mathrm{QW}} < d_{\mathrm{c}}$) QPC-Probe. Mit dem Erreichen der Bandlücke saturiert der Leitwert für den topologischen QPC um $G_{\mathrm{QSH}} \approx 2e^2/h$, wohingegen ebenjener für den Fall des trivialen Bauteils auf $G \approx 0$ abfällt. Darüber hinaus belegen durchgeführte Messungen des differentiellen Leitwertes einer invertierten QPC-Probe in Abhängigkeit einer Biasspannung die stabile Koexistenz von topologischen und trivialen Transportmoden.

Gegenstand von Kapitel 3 ist die Beschreibung der Ausbildung eines QSH-Interferometers in QPCs mit geringer Weite, welche unter Verwendung von Quantentrögen mit einer Trogdicke von $d_{\mathrm{QW}} = 7\,\mathrm{nm}$ hergestellt werden. Die Diskussion von Bandstrukturrechnungen legt dar, dass die räumliche Ausdehnung der Randkanäle von der jeweiligen Position der Fermi-Energie im Bereich der Bandlücke abhängt. Hieraus resultiert eine Transportsituation, in welcher – unter bestimmten Voraussetzungen – Reservoir-Elektronen mit randomisiertem Spin an beide QSH-Randkanäle mit gleicher Wahrscheinlichkeit koppeln, was in der Ausbildung eines QSH-Rings resultiert. Diese Ringbildung wird im Rahmen eines durch Plausibilitätsüberprüfung getesteten Modells erklärt und spezifiziert. Danach erfolgt eine theoretische Einführung von drei relevanten Quantenphasen, deren Akkumulation in der Folge für mehrere geeignete QPC-Proben nachgewiesen wird. Es handelt sich hierbei um die Aharonov-Bohm-Phase [8], um die dynamische Aharonov-Casher-Phase [9] sowie um eine Spin-Bahn-Berry-Phase mit einem Wert von π [10]. Diese experimentellen Ergebnisse stehen darüber hinaus im Einklang mit analytischen Modellbetrachtungen.

Das anschließende Kapitel 4 stellt den letzten Teil der Arbeit dar und beschäftigt sich mit der Beobachtung einer anomalen Leitwertsignatur, welche für QPC-Proben basierend auf einer Quantentrogdicke von $d_{\mathrm{QW}} = 10.5\,\mathrm{nm}$ auftritt. Diese Proben zeigen neben der durch die QSH-Phase bedingten Leitwertquantisierung von $G_{\mathrm{QSH}} \approx 2e^2/h$ ein weiteres Leitwertplateau mit einem Wert von $G \approx e^2/h = 0.5 \cdot G_{\mathrm{QSH}}$. Diese sogenannte 0.5-Anomalie ist nur für ein kleines Intervall von QPC-Weiten beobachtbar und wird mit zunehmender Bauteilweite abgeschwächt. Weiterführende Untersuchungen in Abhängigkeit der Temperatur sowie einer angelegten Biasspannung deuten darüber hinaus darauf hin, dass das Auftreten der 0.5-Anomalie mit einem modifizierten topologischen Zustand einhergeht. Überdies wird eine zusätzliche sowie vervollständigende Charakterisierung dieses Transportregimes durch die Realisierung eines neuartigen Bauteilkonzeptes möglich, welches einen QPC in eine standardisierte Hall-Bar-Geometrie integriert. Das Ergebnis der experimentellen Analyse einer solchen Probe verknüpft das Auftreten der 0.5-Anomalie mit der Rückstreuung eines QSH-Randkanals. Demgemäß wird aus Sicht des Einteilchenbildes geschlussfolgert, dass im Kontext der 0.5-Anomalie lediglich ein Randkanal transmittiert wird. Zudem werden zwei theoretische Modelle basierend auf Elektron-Elektron-Wechselwirkungen diskutiert, welche beide jeweils als ursächlicher Mechanismus für das Auftreten der 0.5-Anomalie in Frage kommen.

Abschließend ist zu deduzieren, dass die Implementierung einer QPC-Technologie in einem QSH-System eine bedeutende Entwicklung im Bereich der Erforschung von zweidimensionalen

topologischen Isolatoren darstellt, welche eine Vielzahl zukünftiger Experimente ermöglicht. So existieren beispielsweise theoretische Vorhersagen, dass QPCs in einem QSH-System die Detektion von Majorana- [11] sowie Para-Fermionen [12] ermöglichen. Überdies ist die nachgewiesene Ausbildung eines QSH-Interferometers in geeigneten QPC-Proben eine Beobachtung von großer Folgewirkung. So ermöglicht die beobachtete dynamische Aharonov-Casher-Phase im QSH-Regime die kontrollierbare Modulation des topologischen Leitwertes, was die konzeptionelle Grundlage eines topologischen Transistors darstellt [13, 14]. Eine weitere Anwendungsmöglichkeit wird durch die Widerstandsfähigkeit geometrischer Phasen gegenüber Dephasierung [15, 16] eröffnet, wodurch die nachgewiesene Spin-Bahn-Berry-Phase mit einem Wert von π im Kontext potentieller Quantencomputerkonzepte von Interesse ist [17–19]. Darüber hinaus ist die Transmission von nur einem QSH-Randkanal im Zuge des Auftretens der 0.5-Anomalie äquivalent zu 100 % Spinpolarisierung, was einen Faktor essentieller Relevanz für die Realisierung spintronischer Anwendungen darstellt [20, 21]. Demgemäß beinhaltet die vorliegende Arbeit den experimentellen Nachweis von drei unterschiedlichen Effekten, von welchen jedem einzelnen eine fundamentale Rolle im Rahmen der Entwicklung neuer Generationen logischer Bauelemente zukommen kann – ermöglicht durch die Realisierung von QPCs in topologischen HgTe-Quantentrögen.

BIBLIOGRAPHY

[1] B. J. van Wees, H. van Houten, C. W. J. Beenakker, J. G. Williamson, L. P. Kouwenhoven, D. van der Marel, and C. T. Foxon, *Quantized conductance of point contacts in a two-dimensional electron gas,* Physical Review Letters **60**, 848 (1988).

[2] D. A. Wharam, T. J. Thornton, R. Newbury, M. Pepper, H. Ahmed, J. E. F. Frost, D. G. Hasko, D. C. Peacock, D. A. Ritchie, and G. A. C. Jones, *One-dimensional transport and the quantisation of the ballistic resistance,* Journal of Physics C: Solid State Physics **21**, L209 (1988).

[3] C. L. Kane and E. J. Mele, *Quantum Spin Hall Effect in Graphene,* Physical Review Letters **95**, 226801 (2005).

[4] B. A. Bernevig, T. L. Hughes, and S.-C. Zhang, *Quantum Spin Hall Effect and Topological Phase Transition in HgTe Quantum Wells,* Science **314**, 1757 (2006).

[5] M. König, S. Wiedmann, C. Brüne, A. Roth, H. Buhmann, L. W. Molenkamp, X. L. Qi, and S.-C. Zhang, *Quantum Spin Hall Insulator State in HgTe Quantum Wells,* Science **318**, 766 (2007).

[6] F. Dolcini, *Full electrical control of charge and spin conductance through interferometry of edge states in topological insulators,* Physical Review B **83**, 165304 (2011).

[7] J. Wang, Y. Meir, and Y. Gefen, *Spontaneous Breakdown of Topological Protection in Two Dimensions,* Physical Review Letters **118**, 046801 (2017).

[8] Y. Aharonov and D. Bohm, *Significance of Electromagnetic Potentials in the Quantum Theory,* Physical Review **115**, 485 (1959).

[9] Y. Aharonov and A. Casher, *Topological Quantum Effects for Neutral Particles,* Physical Review Letters **53**, 319 (1984).

[10] A. G. Aronov and Y. B. Lyanda-Geller, *Spin-orbit Berry phase in conducting rings,* Physical Review Letters **70**, 343 (1993).

[11] J. Li, W. Pan, B. A. Bernevig, and R. M. Lutchyn, *Detection of Majorana Kramers Pairs Using a Quantum Point Contact,* Physical Review Letters **117**, 046804 (2016).

[12] C. Fleckenstein, N. T. Ziani, and B. Trauzettel, $\mathbb{Z}_4$ *parafermions in Weakly Interacting Superconducting Constrictions at the Helical Edge of Quantum Spin Hall Insulators,* Physical Review Letters **122**, 066801 (2019).

[13] X. Qian, J. Liu, L. Fu, and J. Li, *Quantum spin Hall effect in two-dimensional transition metal dichalcogenides,* Science **346**, 1344 (2014).

[14] J. L. Collins, A. Tadich, W. Wu, L. C. Gomes, J. N. B. Rodrigues, C. Liu, J. Hellerstedt, H. Ryu, S. Tang, S.-K. Mo, S. Adam, S. A. Yang, M. S. Fuhrer, and M. T. Edmonds, *Electric-field-tuned topological phase transition in ultrathin Na_3Bi,* Nature **564**, 390 (2018).

[15] A. Carollo, I. Fuentes-Guridi, M. Santos França, and V. Vedral, *Geometric Phase in Open Systems,* Physical Review Letters **90**, 160402 (2003).

[16] S. Filipp, J. Klepp, Y. Hasegawa, C. Plonka-Spehr, U. Schmidt, P. Geltenbort, and H. Rauch, *Experimental Demonstration of the Stability of Berry's Phase for a Spin-1/2 Particle,* Physical Review Letters **102**, 030404 (2009).

[17] J. A. Jones, V. Vedral, A. Ekert, and G. Castagnoli, *Geometric quantum computation using nuclear magnetic resonance,* Nature **403**, 869 (2000).

[18] G. Falci, R. Fazio, G. M. Palma, J. Siewert, and V. Vedral, *Detection of geometric phases in superconducting nanocircuits,* Nature **407**, 355 (2000).

[19] E. Sjöqvist, *A new phase in quantum computation,* Physics **1**, 35 (2008).

[20] S. Datta and B. Das, *Electronic analog of the electro-optic modulator,* Applied Physics Letters **56**, 665 (1990).

[21] S. Datta, *How we proposed the spin transistor,* Nature Electronics **1**, 604 (2018).

A

Fabrication process of a HgTe based quantum point contact

Every fabrication of a QPC device starts with an MBE grown wafer, which is cleaved into sample pieces of approximately $(3 \cdot 3)\,\mathrm{mm}^2$ for production purposes. After an initial cleaning step, the mesa is defined by three consecutive etching steps. Within the scope of this thesis, quantum wells with $d_{\mathrm{QW}} \in [5.5; 10.5]\,\mathrm{nm}$ have been utilized for device fabrication. In the following process description, the term *water* refers to the usage of ultra pure water.

Preparative cleaning step

- Ultrasonic bath in acetone for 5 min at 37 kHz and for 5 min at 80 kHz (both at 100 % P).
- Rinse in isopropanol and water (consecutively), dry with nitrogen.

Definition of the mesa – step I (electron beam lithography)

- Spin coating of PMMA 950 K 3 % in ethyl lactate (supplier: Allresist GmbH) for 40 s at 5000 rpm and softbaking for 10 min at 80 °C.
- Exposure with an acceleration voltage of 2.5 kV, a working distance of 10 mm, an aperture of 30 µm, a writing field size of $(204.8 \cdot 204.8)\,\mu\mathrm{m}^2$, an area dose of $90\,\mu\mathrm{C/cm}^2$, a stepsize of 9.4 nm and a magnification of 389×.
- Development in a solution of AR 600-56 (supplier: Allresist GmbH) and isopropanol (1:1) for 60 s, rinse in isopropanol for 60 s, dry with nitrogen.

- Wet etching of the mesa:
  - Dip the sample for 50 s in a solution of hydrofluoric acid and water (1:200).
  - Rinse in water, dry with nitrogen.
  - Etch for 50 s via the pumping method, use a 2 h old solution of an aqueous solution of KI : I_2 : HBr (standard recipe) and water (1:4).
  - Rinse in water, dry with nitrogen, review the etching result.
- Remove the etch mask in acetone, rinse in isopropanol and water (consecutively), dry with nitrogen.

Definition of the mesa – step II (electron beam lithography)

- Spin coating of PMMA 950 K 3 % in ethyl lactate for 40 s at 7000 rpm and softbaking for 10 min at 80 °C.
- Exposure with an acceleration voltage of 2.5 kV, a working distance of 10 mm, an aperture of 30 µm, a writing field size of $(204.8 \cdot 204.8)\,\mu m^2$, an area dose of $160\,\mu C/cm^2$, a stepsize of 9.4 nm and a magnification of 389×.
- Development in a solution of AR 600-56 and isopropanol (1:1) for 60 s, rinse in isopropanol for 60 s, dry with nitrogen.
- Wet etching of the mesa:
  - Dip the sample for 50 s in a solution of hydrofluoric acid and water (1:200).
  - Rinse in water, dry with nitrogen.
  - Etch for 25 s via the pumping method, use a 2 h old solution of an aqueous solution of KI : I_2 : HBr (standard recipe) and water (1:4).
  - Rinse in water, dry with nitrogen, review the etching result.
- Remove the etch mask in acetone, rinse in isopropanol and water (consecutively), dry with nitrogen.

Definition of the mesa – step III (optical lithography)

- Spin coating of AZ ECI 3012 (supplier: Microchemicals GmbH) for 20 s at 6000 rpm and softbaking for 2 min at 80 °C.

- Exposure for 8 s (or longer if necessary) with an intensity of 8 mW/cm^2.
- Development in AZ 726 MIF (supplier: Microchemicals GmbH) for 22 s, rinse in water, dry with nitrogen.
- Wet etching of the mesa:
  - Etch for 90 s via the pumping method, use a 2 h old solution of an aqueous solution of KI : I_2 : HBr (standard recipe) and water (1:4).
  - Rinse in water, dry with nitrogen, review the etching result.
- Remove the etch mask in acetone, rinse in isopropanol and water (consecutively), dry with nitrogen.

Definition of the gate electrode (electron beam lithography)

- Note: to ensure an optimal alignment process during the exposure of the gate electrode design, a set of alignment marks is exposed and thus made resist-free in a first step.
- Spin coating of PMMA 600 K 6 % in ethyl lactate (supplier: Allresist GmbH) for 40 s at 5000 rpm and softbaking for 15 min at 80 °C.
- Exposure with an acceleration voltage of 30 kV, a working distance of 10 mm, an aperture of 30 µm, a writing field size of $(204.8 \cdot 204.8)\,\mu m^2$, an area dose of 750 µC/cm^2, a stepsize of 9.4 nm and a magnification of 390×.
- Development in AR 600-56 for 60 s, rinse in isopropanol for 60 s, dry with nitrogen.
- Exposure with an acceleration voltage of 6.5 kV, a working distance of 10 mm, an aperture of 20 µm, a writing field size of $(204.8 \cdot 204.8)\,\mu m^2$, an area dose of 300 µC/cm^2, a stepsize of 9.4 nm and a magnification of 388×.
- Development in AR 600-56 for 60 s (after 30 s: ultrasonic pulse of 1 s at 80 kHz and 50 % power), rinse in isopropanol for 60 s, dry with nitrogen.
- Execution of a short oxygen plasma cleaning step in order to remove PMMA residuals. The process parameters are strongly depending on the utilized machine. For the QPC devices presented within this thesis, program 70 of the chair's reactive ion etching machine was used. The process was stopped manually 3 s after the machine's readout of the reflected power dropped to 0.
- ALD growth of 90 cycles of HfO_2 at ≈ 35 °C.

- Electron beam physical vapour deposition (EBPVD) based metallization of 5 nm of Ti and of 350 nm of Au.
- Lift-off in acetone for 30 min at 50 °C.
- Rinse in isopropanol and water (consecutively), dry with nitrogen.

Definition of the gate leads (optical lithography)

- Spin coating of AR-N 4340 (supplier: Allresist GmbH) for 20 s at 6000 rpm and softbaking for 2 min at 80 °C.
- Exposure for 20 s with an intensity of 8 mW/cm^2.
- Post exposure bake for 6 min at 80 °C.
- Development in AR 300-47 (supplier: Allresist GmbH) for 42 s, rinse in water, dry with nitrogen.
- EBPVD based metallization of 5 nm of Ti and of 250 nm of Au.
- Lift-off in acetone for 10 min at 50 °C.
- Rinse in isopropanol and water (consecutively), dry with nitrogen.

Definition of the ohmic contacts (optical lithography)

- Spin coating of AR-N 4340 for 20 s at 6000 rpm and softbaking for 2 min at 80 °C.
- Exposure for 20 s with an intensity of 8 mW/cm^2.
- Post exposure bake for 6 min at 80 °C.
- Development in AR 300-47 for 42 s, rinse in water, dry with nitrogen.
- Contact etch process using the chair's ion beam etching machine. Goal: etch $\approx$ 20 nm close to the HgTe layer. Process parameters: beam/extractor voltages of $\pm$0.4 kV, beam current of 8 mA, argon flow of 3.5 sccm. The etching time depends on the thickness of the cap layer. The etching rate depends on the configuration of the machine and has to be redetermined from time to time.

- In situ transfer, EBPVD based metallization of 80 nm of AuGe and of 170 nm of Au.
- Lift-off in acetone for 10 min at 50 °C.
- Rinse in isopropanol and water (consecutively), dry with nitrogen.

B

Completive transport data

The gate voltage V_G dependence of the conductance G of the QPC devices presented within the course of Chapter 2 is corrected by the subtraction of a serial resistance R_{Serial} for five out of six devices. For the sake of completeness, the comparison between the corrected and uncorrected transport data is presented in Fig. B.1. The individual subtracted values are added to the caption of Fig. B.1.

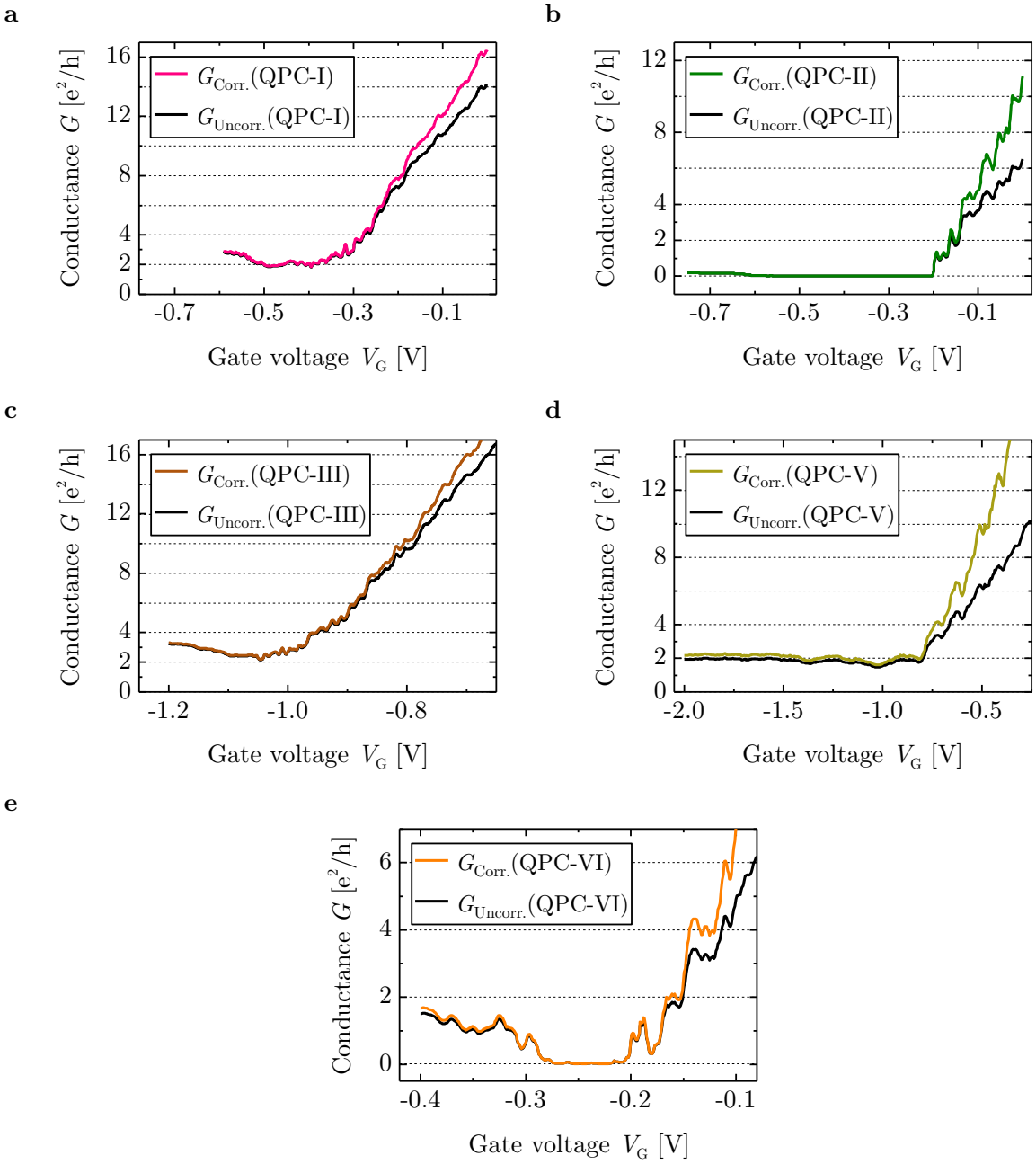

Figure B.1: **a**, Gate voltage V_{G} dependence of the conductance G of QPC-I. A serial resistance of $R_{\text{Serial}} = 260\,\Omega$ is subtracted for the corrected trace. **b**, Gate voltage V_{G} dependence of the conductance G of QPC-II. A serial resistance of $R_{\text{Serial}} = 1650\,\Omega$ is subtracted for the corrected trace. **c**, Gate voltage V_{G} dependence of the conductance G of QPC-III. A serial resistance of $R_{\text{Serial}} = 150\,\Omega$ is subtracted for the corrected trace. **d**, Gate voltage V_{G} dependence of the conductance G of QPC-V. A serial resistance of $R_{\text{Serial}} = 1450\,\Omega$ is subtracted for the corrected trace. **e**, Gate voltage V_{G} dependence of the conductance G of QPC-VI. A serial resistance of $R_{\text{Serial}} = 1600\,\Omega$ is subtracted for the corrected trace.

C

Fabrication process of a HgTe based quantum point contact embedded in a multi-terminal device geometry

The following process steps describe the fabrication of a QPC embedded in a multi-terminal device geometry. As outlined in Chapter 4, the process is still in the development phase. Within the scope of this thesis, a quantum well with $d_{\mathrm{QW}} = 10\,\mathrm{nm}$ has been utilized for device fabrication. Equivalent to standard QPC devices, the mesa is defined by three consecutive etching steps. In the following process description, the term *water* refers to the usage of ultra pure water.

Preparative cleaning step

- Ultrasonic bath in acetone for 5 min at 37 kHz and for 5 min at 80 kHz (both at 100 % P).
- Rinse in isopropanol and water (consecutively), dry with nitrogen.

Definition of the mesa – step I (electron beam lithography)

- Spin coating of PMMA 950 K 3 % in ethyl lactate for 40 s at 5000 rpm and softbaking for 10 min at 80 °C.

- Exposure with an acceleration voltage of 2.5 kV, a working distance of 10 mm, an aperture of 30 µm, a writing field size of $(204.8 \cdot 204.8)\,\mu m^2$, an area dose of $90\,\mu C/cm^2$, a stepsize of 9.4 nm and a magnification of 389×.
- Development in a solution of AR 600-56 and isopropanol (1:1) for 60 s, rinse in isopropanol for 60 s, dry with nitrogen.
- Wet etching of the mesa:
  - Dip the sample for 50 s in a solution of hydrofluoric acid and water (1:200).
  - Rinse in water, dry with nitrogen.
  - Etch for 30 s via the pumping method, use a 2 h old solution of an aqueous solution of KI : I_2 : HBr (standard recipe) and water (1:4).
  - Rinse in water, dry with nitrogen, review the etching result.
- Remove the etch mask in acetone, rinse in isopropanol and water (consecutively), dry with nitrogen.

Definition of the mesa – step II (electron beam lithography)

- Spin coating of PMMA 950 K 3 % in ethyl lactate for 40 s at 7000 rpm and softbaking for 10 min at 80 °C.
- Exposure with an acceleration voltage of 2.5 kV, a working distance of 7 mm, an aperture of 30 µm, a writing field size of $(81.92 \cdot 81.92)\,\mu m^2$, an area dose of $160\,\mu C/cm^2$, a stepsize of 10 nm and a magnification of 868×.
- Choose a design width of $W = 450$ nm.
- Development in a solution of AR 600-56 and isopropanol (1:1) for 60 s, rinse in isopropanol for 60 s, dry with nitrogen.
- Wet etching of the mesa:
  - Dip the sample for 50 s in a solution of hydrofluoric acid and water (1:200).
  - Rinse in water, dry with nitrogen.
  - Etch for 15 s via the pumping method, use a 2 h old solution of an aqueous solution of KI : I_2 : HBr (standard recipe) and water (1:4).
  - Rinse in water, dry with nitrogen, review the etching result.

- Remove the etch mask in acetone, rinse in isopropanol and water (consecutively), dry with nitrogen.

Definition of the mesa – step III (optical lithography)

- Spin coating of AZ ECI 3012 for 20 s at 6000 rpm and softbaking for 2 min at 80 °C.
- Exposure for 8 s (or longer if necessary) with an intensity of 8 mW/cm^2.
- Development in AZ 726 MIF for 22 s, rinse in water, dry with nitrogen.
- Wet etching of the mesa:
  - Etch for 90 s via the pumping method, use a 2 h old solution of an aqueous solution of KI : I_2 : HBr (standard recipe) and water (1:4).
  - Rinse in water, dry with nitrogen, review the etching result.
- Remove the etch mask in acetone, rinse in isopropanol and water (consecutively), dry with nitrogen.

Definition of gate electrode A & B (electron beam lithography)

- Note: to ensure an optimal alignment process during the exposure of the gate electrode design, a set of alignment marks is exposed and thus made resist-free in a first step.
- Spin coating of PMMA 600 K 6 % in ethyl lactate for 40 s at 5000 rpm and softbaking for 15 min at 80 °C.
- Exposure with an acceleration voltage of 30 kV, a working distance of 10 mm, an aperture of 30 µm, a writing field size of $(204.8 \cdot 204.8)$ µm^2, an area dose of 750 µC/cm^2, a stepsize of 9.4 nm and a magnification of 390×.
- Development in AR 600-56 for 60 s, rinse in isopropanol for 60 s, dry with nitrogen.
- Exposure with an acceleration voltage of 6.5 kV, a working distance of 10 mm, an aperture of 20 µm, a writing field size of $(204.8 \cdot 204.8)$ µm^2, an area dose of 300 µC/cm^2, a stepsize of 9.4 nm and a magnification of 388×.
- Choose a design width of $W = 800$ nm.

- Development in AR 600-56 for 60 s (after 30 s: ultrasonic pulse of 1 s at 80 kHz and 50 % power), rinse in isopropanol for 60 s, dry with nitrogen.
- Execution of a short oxygen plasma cleaning step in order to remove PMMA residuals. The process parameters are strongly depending on the utilized machine. For the QPC devices presented within this thesis, program 70 of the chair's reactive ion etching machine was used. The process was stopped manually 3 s after the machine's readout of the reflected power dropped to 0.
- ALD growth of 45 cycles of HfO_2 at $\approx 35\,^{\circ}C$.
- EBPVD based metallization of 5 nm of Ti and of 300 nm of Au.
- Lift-off in acetone in an ultrasonic bath using 37 kHz and 100 % P at 40 °C for 20 min (start the ultrasonic bath first, then add the sample).
- Rinse in isopropanol and water (consecutively), dry with nitrogen.

Definition of gate electrode C (electron beam lithography)

- Note: to ensure an optimal alignment process during the exposure of the gate electrode design, a set of alignment marks is exposed and thus made resist-free in a first step.
- Spin coating of PMMA 600 K 6 % in ethyl lactate for 40 s at 5000 rpm and softbaking for 15 min at 80 °C.
- Exposure with an acceleration voltage of 30 kV, a working distance of 10 mm, an aperture of 30 µm, a writing field size of $(204.8 \cdot 204.8)\,\mu m^2$, an area dose of $750\,\mu C/cm^2$, a stepsize of 9.4 nm and a magnification of 390×.
- Development in AR 600-56 for 60 s, rinse in isopropanol for 60 s, dry with nitrogen.
- Exposure with an acceleration voltage of 6.5 kV, a working distance of 10 mm, an aperture of 20 µm, a writing field size of $(204.8 \cdot 204.8)\,\mu m^2$, an area dose of $300\,\mu C/cm^2$, a stepsize of 9.4 nm and a magnification of 388×.
- Choose a design width of $W = 350$ nm.
- Development in AR 600-56 for 60 s (after 30 s: ultrasonic pulse of 1 s at 80 kHz and 50 % power), rinse in isopropanol for 60 s, dry with nitrogen.

- Execution of a short oxygen plasma cleaning step in order to remove PMMA residuals. The process parameters are strongly depending on the utilized machine. For the QPC devices presented within this thesis, program 70 of the chair's reactive ion etching machine was used. The process was stopped manually 3 s after the machine's readout of the reflected power dropped to 0.
- ALD growth of 90 cycles of HfO_2 at $\approx 35\,^{\circ}C$.
- EBPVD based metallization of 5 nm of Ti and of 300 nm of Au.
- Lift-off in acetone in an ultrasonic bath using 37 kHz and 100 % P at 40 °C for 20 min (start the ultrasonic bath first, then add the sample).
- Rinse in isopropanol and water (consecutively), dry with nitrogen.

Definition of the gate leads (optical lithography)

- Spin coating of AR-N 4340 for 20 s at 6000 rpm and softbaking for 2 min at 80 °C.
- Exposure for 20 s with an intensity of $8\,mW/cm^2$.
- Post exposure bake for 6 min at 80 °C.
- Development in AR 300-47 for 42 s, rinse in water, dry with nitrogen.
- EBPVD based metallization of 5 nm of Ti and of 250 nm of Au.
- Lift-off in acetone for 10 min at 50 °C.
- Rinse in isopropanol and water (consecutively), dry with nitrogen.

Definition of the ohmic contacts (optical lithography)

- Spin coating of AR-N 4340 for 20 s at 6000 rpm and softbaking for 2 min at 80 °C.
- Exposure for 20 s with an intensity of $8\,mW/cm^2$.
- Post exposure bake for 6 min at 80 °C.
- Development in AR 300-47 for 42 s, rinse in water, dry with nitrogen.

- Contact etch process using the chair's ion beam etching machine. Goal: etch $\approx 20\,\mathrm{nm}$ close to the HgTe layer. Process parameters: beam/extractor voltages of $\pm 0.4\,\mathrm{kV}$, beam current of $8\,\mathrm{mA}$, argon flow of $3.5\,\mathrm{sccm}$. The etching time depends on the thickness of the cap layer. The etching rate depends on the configuration of the machine and has to be redetermined from time to time.
- In situ transfer, EBPVD based metallization of $80\,\mathrm{nm}$ of AuGe and of $170\,\mathrm{nm}$ of Au.
- Lift-off in acetone for $10\,\mathrm{min}$ at $50\,^{\circ}\mathrm{C}$.
- Rinse in isopropanol and water (consecutively), dry with nitrogen.

List of publications

- Interacting topological edge channels.
  Jonas Strunz, Jonas Wiedenmann, Christoph Fleckenstein, Lukas Lunczer, Wouter Beugeling, Valentin L. Müller, Pragya Shekhar, Niccolò Traverso Ziani, Saquib Shamim, Johannes Kleinlein, Hartmut Buhmann, Björn Trauzettel and Laurens W. Molenkamp. *Nature Physics* **16**, 83 (2020).

Acknowledgements

In most cases, scientific achievements in the field of experimental physics are far from being results of a one-man show. The latter also applies to the thesis at hand. Thus, the following part is dedicated to express my gratitude to all the people who contributed to the success of my Ph.D. time. In detail, I want to thank:

Prof. Dr. Laurens W. Molenkamp and Prof. Dr. Hartmut Buhmann for accepting me as a Ph.D. student at EP-III.

Dr. Jonas Wiedenmann for being the most competent and inspiring postdoc a Ph.D. student could wish for. Even though our time was limited to roughly twelve months, I guess it is fair to say that we had an outstanding and fruitful year. Thank you very much Jonas for teaching me your sophisticated as well as pragmatic approach of understanding mesoscopic physics, it was a huge pleasure to work with you.

Prof. Dr. Björn Trauzettel for accepting my request to act as the second referee of my Ph.D. thesis. Furthermore, I want to thank you for your elevated role throughout the publishing process of the 0.5 anomaly manuscript and as well – apart from physics – for your comfortable and highly enjoyable interpersonal nature.

Julian Werther and Lukas Scheffler, my comrades-in-arms of the Verfügungsgebäude. Thank you very much for all the way too long lunch breaks, the extensive discussions about everything but physics and for all the laughter. Without you guys, my work at EP-III would have been way less endurable. I am really grateful for our time together.

Lukas Lunczer for always supplying me with top-notch material on demand. Moreover, I want to thank you Lukas for always being willing to discuss – recent results as well as non-physical topics – and for your honest interest in my research. It was a big pleasure to work with you.

Dr. Valentin L. Müller and Pragya Shekhar for all the countless and collectively survived sessions in the cleanroom, the discussions about lithography as well as the good company during my whole Ph.D. journey. It was a gift to work with both of you.

Volkmar Hock for giving me – and my fellow ordinary mortals working in the cleanroom – the chance to benefit from his technological wizardry. Thank you very much Volkmar for always ensuring excellent equipment conditions and for all our enriching, funny and cynical conversations during the last years.

Michael Kick, who supported my work as a master's student, and Alex J. Currie, who did an internship in our group supervised by me. I think it is fair to say that we had the chance to learn a lot together about the actual process of experimental research as well as about its flaws and its mercilessness – but also about its incomparable beauty. Thank you very much guys.

Furthermore, I want to thank all my colleagues and companions I had the honour to work with during the last years, in particular Dr. Christoph Fleckenstein, Prof. Dr. Erwann Bocquillon, Dr. Tobias Kießling, Dr. Tanja Borzenko, Dr. Saquib Shamim, Dr. Wouter Beugeling, Dr. Kalle Bendias, Andreas Budewitz, Johannes Baumann, Dr. Johannes Kleinlein and above all Marco Dusel, Marco De Gregorio and Pascal Laudenbach.

Most importantly, I want to thank my grandparents Hubert and Christine, my parents Raimund and Karin and my siblings Elias and Lea. And finally, I want to express my deepest gratitude to my girlfriend Eva for always unconditionally supporting me and for accepting well-nigh lunatic amounts of lab and office hours on a regular basis – which has become even more relevant and essential when I decided to put a way beyond reasonable workload on my shoulders back in 2019. I couldn't be more thankful.